

DA 14 22.9  
704  
91



**Ultrafast pump-and-probe spectroscopy in a CdSe thin film**

by

**Fumio Sasaki**

Submitted in partial fulfillment of the requirements for  
the degree of Doctor of Science in Doctoral Program in  
**University of Tsukuba**

January 1991

92303011

## Abstract

Ultrafast pump-and-probe spectroscopy was adopted to study the dynamics of the photogenerated carriers in a CdSe thin single crystal film.

In case of the band-to-band excitation, nonthermalized hot carrier distribution was observed when the pump pulse turns on. However, the distribution was thermalized as soon as the pump pulse turns off. This nonequilibrium distribution of hot carriers is thermalized by the carrier-carrier scattering. From the ratio of nonthermalized distribution to the total one, the thermalization time was estimated to be 20-40 fs.

In order to discuss the fast scattering processes of carriers quantitatively, ensemble Monte-Carlo simulation was performed. However, the full agreement could not be obtained. In order to obtain better agreement, it is necessary to improve the simulation.

In the wake of the thermalization, cooling of photogenerated carriers was observed. In this process, the carrier-LO phonon scattering is dominant. The obtained cooling time of carriers informed us that the carrier LO-phonon scattering time is 1.5-2.0 ps. The values are slower than those estimated from Frölich interaction by an order of magnitude. The analysis indicates that the slow cooling time is due to the hot phonon effect for the electrons and rapid thermalization between the electrons and the holes.

Under the resonant excitation of the A-exciton, the small bleaching and the broadening of the B-exciton structure were

observed. The small bleaching of the B-exciton was explained as the broadening of the B-exciton and the phase space filling of the conduction band. The bleaching was found to rise with a fast rise time about 400 fs. The transient broadening of the B-exciton structure indicates that the A-exciton-B-exciton scattering time is 31 fs. The value was explained by a simple theory based on the rigid-spheres scattering model. It was calculated by taking account of the A-exciton's velocity at the given density and temperature. The broadening continues for a long time, an order of hundreds of picoseconds. This duration is well explained by the lifetime of the excitons.

Under the resonant excitation of the B-exciton, the instantaneous broadening and the prompt recovery of the induced absorption were observed above the B-exciton energy. In the succeeding time region, the induced absorption with 1.7 ps rise time was observed. This rise in the induced absorption is considered to be ascribed to the carrier cooling. The bleaching increases instantaneously at the A-exciton, in contrast with the gradual rise in the bleaching of the A-exciton observed under the band-to-band excitation. This fact suggests the phase space filling effect of the conduction band.

We observed the common features in the pump-and-probe spectra independent of the excitation photon energy. One is the coherent oscillation around the exciton before the pump pulse hits the sample. Another is a succeeding transient broadening of the A- and the B-excitons when the pump pulse hits the sample. Third is the induced absorption in the band-to-band absorption

region. In case of the A-exciton resonant excitation, the induced absorption in the band is considered as the broadening of the B-exciton.

Throughout this study, many ultrafast scattering processes of photogenerated carriers are discussed and clarified.

## Contents

I. Introduction	5
II. Experiments	
2.1 Generation of ultrafast light pulses	11
2.2 Dispersion compensation	13
2.3 Sample preparation	15
2.4 Experimental results of the pump-and-probe experiments	
2.4.1 High energy band-to-band excitation	16
2.4.2 Resonant excitation	18
III. Monte-Carlo simulation	20
IV. Discussions	
4.1 Nonequilibrium distribution of photoexcited carriers	24
4.2 Cooling of hot carriers	28
4.3 Common and different features observed in three pump-and-probe experiments	35
4.4 A-exciton resonant excitation	39
4.5 B-exciton resonant excitation	44
V. Conclusions	47
Acknowledgements	49
Appendix	50
References	53
Figure captions	59
Figures	

## I. Introduction

Generation of ultrafast optical pulses needs various kinds of optical techniques and generating itself lies in one of a recently developed field in sciences.<sup>1,2)</sup> In these rapidly developed fields, nonlinear phenomena caused by optical excitation are one of an attractive field of studies. In a basic point of view, one can directly observe unknown ultrafast phenomena and explore the new physics. Especially, ultrafast nonlinear phenomena in semiconductors have a potential not only to realize an optical computer, but also to observe an intrinsic aspect of solid state physics.<sup>3)</sup>

Generally, there are two types of fields to study. One is a dynamics of photoexcited carriers, and the other is a coupling phenomenon between materials and optical field. If the time range to observe reduces to the cycle of the optical field and mono scattering time, such a classification becomes very difficult. However, there are many possibilities to observe and find an unknown and new phenomenon. As an example of the coupling phenomenon between materials and optical field, the optical Stark effect in semiconductors is one of great findings in this field.<sup>4-11)</sup>

In the former field, hot carrier effect in semiconductors is one of the most important subjects. One can directly observe the dynamical carrier distribution and obtain the relaxation processes in solids.<sup>12)</sup> Hot carrier phenomena are determined primarily by band structures and carrier-phonon scattering processes and therefore provide important information about

carrier-phonon interactions. On the other hand, hot carrier physics determines the behavior of ultrafast, ultrasmall semiconductor devices operating at high electric fields.<sup>12)</sup> Therefore, a study of hot carrier effects is also extremely valuable for a thorough understanding of such devices.

In the analysis of this phenomenon, one must consider the many-body effects, such as the absorption saturation caused by the phase space filling, the band gap renormalization caused by the change in the exchange-correlation energy and the Fermi energy in the electron system, so on. In order to understand the band gap renormalization (BGR), we consider the self energy of a point charge in a plasma. In this simple model, the renormalized band gap  $\Delta E_g$  is qualitatively represented by<sup>3)</sup>

$$\Delta E_g = \lim_{r \rightarrow 0} [ V_s(r) - V(r) ] . \quad (1.1)$$

Here,  $V(r)$  and  $V_s(r)$  denote the bare ( $\propto 1/r$ ) and the screened ( $\propto e^{-k_s r} / r$ ) Coulomb potential, respectively. Thus, the band gap reduction is represented by

$$\Delta E_g = - \frac{e^2 k_s}{\epsilon_0} . \quad (1.2)$$

Here,  $e$ ,  $\epsilon_0$  and  $k_s$  denote an electron charge, a static dielectric constant of the material and a screened wave vector, respectively.

The excitonic enhancement effect including excitons gives a characteristic absorption spectrum at low lattice temperature in

intrinsic semiconductors. At the room temperature, the enhancement effect is relatively small. However, in the 2-dimensional ( 2D ) system, the absorption peaks of excitons are clearly observed. The excitonic enhancement effect is strongly modified by high density carriers. Therefore, especially at low lattice temperature, or also at the room temperature in case of the 2D system, we must consider this effect in the analysis.

Up to now, the studies of the hot carrier system have been extensively done by means of transport experiments, luminescence spectroscopies around the fundamental gap of semiconductors. With the advance of the ultrafast laser spectroscopy, the time-resolved absorption experiments have been adopted to study this subject.<sup>12-32)</sup> As one of the most interesting feature of this study, one can directly observe the distribution of photoexcited carriers. From the observations, we have obtained the very interesting information about the relaxation processes of hot carriers as follows.

At first, photoexcited carriers are distributed at the same energy width of the pump pulse. If the carrier-carrier scattering process is very fast, the width of the distribution broadens. The transient spectral hole burning was experimentally observed in 3D<sup>20,23,24)</sup>, 2D<sup>25,26)</sup> and 0D<sup>32)</sup> systems. The transient spectral hole diminishes in several tens or hundreds of femtoseconds depending on excitation energy and density. After the transient hole diminishes, only the bleaching is observed below the pump photon energy. The bleaching profile shows the carrier distribution. Generally, carriers are thermalized by the carrier-carrier scattering. The scattering time is found to be

an order of a few or a few tens of femtoseconds by means of the femtosecond photon echo technique.<sup>33)</sup> In the succeeding time region, the photoexcited carriers emit phonons and lose their energy. The cooling rate of carriers depends strongly on the carrier-phonon scattering rate.

There are three types of the carrier-phonon scattering mechanisms. One is a polar optical scattering, that is a carrier-LO phonon scattering. A carrier-TO phonon scattering is not so important, because the transverse oscillation makes a relatively weak potential fluctuation. However, the longitudinal oscillation causes the ionic fluctuation, so that the carriers interact strongly with the longitudinal modes. Another is called a piezoelectric scattering. Third one is a deformation potential scattering. The later two scattering processes come from the carrier-acoustic phonon scattering. If photoexcited carriers have enough excess energy larger than the LO phonon energy, the carrier-LO phonon scattering is fastest among three processes. If not, the carrier-LO phonon scattering rate becomes very slow. In this case, the piezoelectric scattering process is a dominant process of energy transfer from the carrier system to the lattice.<sup>34,35)</sup>

There is another important scattering mechanism of photoexcited carriers. That is an intervalley scattering process. If conduction or valence bands have valley minima except the  $\Gamma$  point and photoexcited carriers have enough excess energy, the carriers can scatter to other valley. Through recent studies of GaAs and  $\text{Al}_x\text{Ga}_{1-x}\text{As}$  systems, the  $\Gamma$ -X or the  $\Gamma$ -L scattering surely occurs and was found that the scattering time is several tens of

femtoseconds.<sup>27-31)</sup> To study the multivalley scattering mechanism is very interesting and important in itself, but such a scattering mechanism makes it difficult to interpret the result.

In order to clarify the carrier cooling mechanism, we must consider the other effect which modifies the carrier-phonon interaction. One is a screening effect of the carrier-LO phonon interaction caused by highly excited carriers. The other is nonequilibrium phonon distribution effect, called a hot phonon effect.<sup>36-44)</sup> Both effects make the carrier cooling very slow. In the recent studies, the latter effect was found to be a dominant mechanism in the cooling processes. However, there are few study in the femtosecond region about the hot phonon effect. The fastest carrier-phonon interaction, carrier-polar optical phonon scattering takes place in an order of hundred femtoseconds region. Therefore, the hot-phonon effect in the femtosecond spectroscopy is now an open problem.

In these points of view, I have studied hot carrier effect in a bulk semiconductor, a CdSe thin crystal, by means of ultrafast pump-and-probe experiment under high energy excitation. In CdSe, a single conduction and valence valley is relevant under less than 4 eV photoexcitation, so that we take into account the scattering mechanisms only in a  $\Gamma$ -valley. As a result, non-equilibrium distribution of photogenerated hot carriers were observed under the condition where the carriers can emit the LO phonons. The nonequilibrium distribution was observed only when the pump pulse turns on.

The other purpose of this thesis is how the resonantly excited excitons behave. It is important to note that there are

many differences between two cases. One is the case where the initially excited carriers are hot carriers with large excess energy. On the other case, the excitons are initially excited. In the former case, an important process is the change of carriers' distribution, as already mentioned. However, in the latter case, one can obtain the information about the dense exciton system and its relaxation process.

In the previous study in 3D, the exciton bleaching caused by the free carriers works more effectively than by the dense excitons.<sup>3,45-49)</sup> This fact shows that the screening of Coulomb potential in the free carriers is stronger than in the dense exciton systems. On the contrary, the screening is not so important on the exciton bleaching in quasi 2D system.<sup>3,25)</sup> Such differences between 3D and 2D excitons are discussed by several authors.<sup>3,25,47)</sup> In this study, we tried to clarify the dynamics of the dense exciton system. Especially, CdSe has A- and B-excitons near the absorption edge, so that we obtain the information of two exciton bands.

In the section II, the experimental set-up and the experimental data of the pump-and-probe experiment are shown. In the section III, the method of the Monte-Carlo simulations are explained. In the section IV, discussions about the experimental results and comparison of the data with the numerical simulations will be given.

## II. Experiments

### 2.1 Generation of ultrafast light pulses

During the past 20 years, progress in the generation of optical pulses has opened the femtosecond time domain for investigation of a great variety of new phenomena in physics, chemistry, and biology. The advances have taken place recently in the generation of ultrashort pulses, starting from the colliding-pulse mode-locked ( CPM ) dye laser with amplification and compression techniques.<sup>50-53)</sup> In this thesis, two short-pulse sources were used.

One laser source consists of a cw mode-locked  $\text{Nd}^{3+}$ :YAG laser, the first-stage fiber compressor, a second-harmonic generator, a synchronously pumped cavity-dumped dye laser, the second-stage fiber compressor, and a dye amplifier pumped by a Q-switched  $\text{Nd}^{3+}$ :YAG laser. In this case, the pump-photon energy was 2.12 eV and pulse energy was about 400  $\mu\text{J}$  with 260 femtosecond pulse width ( the repetition rate was 10 Hz ). The laser pulses were splitted into two beams. One beam was focussed to a 1 cm water cell and generated white continuum femtosecond pulses. The white light pulses were used as a probe beam. The spectral range of the probe beam was selected by using some color filters. The other beam was used as a pump light through an optical delay. Powers of the excitation and probe beams were changed by using rotational neutral density filters in order to avoid the changes in the time delay and the dispersion. The dispersion effect caused by optical elements is referred in the

subsection 2.2. The diameter of the spot size and the overlap of two beams were checked by using a microscope.

The other laser source is consist of a CPM dye laser pumped by an Ar<sup>+</sup> laser. The output of the light pulses are amplified by a multi-path amplifier pumped by a Cu-vapor laser. The amplified beam is focused to an ethylene-glycol jet and generates white light continuum. A part of the white light is used as a probe beam. Most of the white light is through a interferential filter and selected its wavelength. The band width is about 10 nm. This beam is amplified by using another Cu-vapor laser. In this case one can tune the pump-photon energy. These Cu-vapor lasers have high repetition rate ( about 8.5 kHz ), so that the data accumulation rate become high in comparison with a Q-switched Nd<sup>3+</sup>:YAG laser system. Therefore, one can obtain the data with a better S/N ratio. In this system, the pump pulse width is between 70 and 150 fs depending on the photon energy. To reduce the pump light leakage, especially in case of the resonant pump experiments, pump and probe beams were polarized orthogonally to each other.

## 2.2 Dispersion compensation

In the femtosecond experiment, one of the difficulty comes from the dispersion compensation. The refractive indices in all optical elements, lenses, filters, mirrors and a water cell including water depend on the photon wavelength. When a short pulse with a finite wavelength width passes through some optical elements, the time delay is changed depending on the wavelength and the time width of the pulse is broadened. This effect is usually negligible in the picosecond spectroscopy, but in the femtosecond spectroscopy, one must take care of this effect much more. Especially, if we want to observe a wide range spectrum, we must suppress the dispersion of the optics as far as possible. Figures 1 to 3 show the time delay as a function of photon wavelength based on the actual measurement by using the sum-frequency generation. The solid circles represent the measured time delay. The results show that the typical dispersion value is an order of 10 fs/nm. Taking account of the second-order term, the least square fitting was done. Time delay  $T_d$  from the fundamental light is represented by

$$T_d(\lambda) = a \lambda^2 + b \lambda + c . \quad ( 2.1 )$$

Here,  $\lambda$  denotes the wavelength of the probe pulse, and  $a$ ,  $b$  and  $c$  are fitting parameters. The solid lines in all figures are the results of the fitting. The agreement between the experimental results and the fitting is very good, and the maximum deviation of the data from the fitting curve is smaller than 10 fs. Based

on eq. (2.1), the time delays of probe spectra were corrected depending on its wavelength. In this way, the time-resolved spectra were obtained in the wide-energy range.

### 2.3 Sample preparation

Samples, CdSe single crystal thin films were grown on the mica substrates by means of the hot wall epitaxy.<sup>54)</sup> The growth equipment used in this method is illustrated in Fig. 4. Temperatures of a head, a wall, a source and a reservoir were controlled. Typical temperatures of each parts were about 400, 650, 580 and 300 °C, respectively. A mica substrate is suitable for the absorption experiment, because it is transparent for the visible light. Moreover, a mica is a layered compound and its interlayer interaction comes from van-der-Waals force. Therefore, the mismatch between a mica substrate and a CdSe crystal is considered to be smaller than other systems.

In the experiments, a CdSe single crystal thin film 0.65  $\mu\text{m}$  thick was used. Typical transmittance at the pump photon energy is about 5 %, so that the sample is excited fairly uniformly.

## 2.4 Experimental results of the pump-and-probe experiment

As mentioned above, various kinds of photoexcitation experiments were performed. We show the experimental results in this subsection and discuss about the results in the section IV. There are five kinds of experiments in the rough classification.

- (1) Pump at 2.12 eV with the pulse width of 260 fs at 4.2 K.
- (2) The same pumping condition at the room temperature.
- (3) Pump at 1.99 eV with the pulse width of 70 fs at 10 K.
- (4) Pump at 1.86 eV with the pulse width of 110 fs at 10 K.
- (5) Pump at 1.82 eV with the pulse width of 150 fs at 10 K.

The experiments (1)~(3) correspond to the band-to-band excitation. The experiments (4) and (5) correspond to the resonant excitation of the B- and the A-excitons, respectively. The data acquisition was done by using an optical multi-channel analyzer (OMA) and a 25 cm spectrometer with low-dispersive gratings (300 groves/mm or 600 groves/mm) to obtain a wide energy range spectrum, and in some cases, photomultipliers.

### 2.4.1 High energy band-to-band excitation

Figures 5 and 6 show the time-resolved absorption spectra under the experimental conditions (1) and (2). The condition (1) corresponds to the 2.12 eV excitation at 4.2 K and the condition (2) to the same excitation at the room temperature, respectively. The excitation densities are 900 and 600  $\mu\text{J}\cdot\text{cm}^{-2}$ , respectively. The absorption spectra denoted by "NO PUMP" were obtained without the pump-pulses. The structures of A- and B-excitons are clearly

observed in Fig. 5. In Fig. 6, A-exciton corresponds to a kink around 1.76 eV. The spectrum at 0 ps shows a broad spectral dip around 2.0 eV in Fig. 5 and around 1.9 eV in Fig. 6. It is due to the nonthermalized distribution of hot carriers. Figures 7 and 8 show the change of the absorption coefficient normalized by unperturbed one,  $-\Delta\alpha/\alpha$  under the experimental condition (1) and (2), respectively. Figures 9 and 10 show the similar results at 4, 8 and 12 ps time delays. Figures 11 and 12 show the time dependences of  $-\Delta\alpha/\alpha$  at 4.2 K and the room temperature, respectively.

Figures 13 to 16 show the time-resolved absorption change,  $-\Delta\alpha$  under the experimental condition (3). In Figs. 13 and 14, each spectrum is normalized by the respective maximum value. In these cases, the S/N ratio is better than in (1) and (2), so that detailed structures can be observed. One of those is the coherent oscillation around the exciton structure preceding the pump pulse in Fig. 13.<sup>55-57)</sup> Another is the transient broadening of the A-exciton in Figs. 14 and 15. Another is nonequilibrium distribution around the time origin in Figs. 14 and 15, similarly to the experimental condition (1) and (2). Another is the induced absorption above the B-exciton at several picosecond time delays in Fig. 16. Figures 17 and 18 show the time dependence of  $-\Delta\alpha$  within 2 ps time delay and 12 ps time delay, respectively. The induced absorption above the B-exciton is more clearly observed in Fig. 18.

### 2.4.2 Resonant excitation

Figures 19 to 25 show the time-resolved spectra obtained by using an OMA. Each spectrum in these figures is normalized by the respective maximum value. Figures 19 to 21 are the results of the A-exciton resonant excitation. When the probe pulse precedes the pump pulse, spectral oscillations were observed. The oscillations come from the coherent effect, similar to the band-to-band excitation. Other features in the figures are the transient broadening at the low energy side of the A-exciton and the induced absorption above the B-exciton. Figures 22 to 25 show the results of the B-exciton resonant excitation. In this figure, the coherent oscillations and the transient broadening at the low energy side of the A-exciton are also observed.

To see the detailed time dependences of the spectra, we observed the transient trace of  $-\Delta\alpha$  at several spectral points. Figures 26 to 30 show the results around the time origin. The probe energy  $E_{pr}$  is shown in each figure. In all the figures the solid lines represent the data taken under the resonant excitation of the B-exciton ( excitation condition (4) ), and the dashed lines the data taken under the resonant excitation of the A-exciton ( excitation condition (5) ). Several features are found in the figures. One is an induced absorption with a rather slow rise time about 1.7 ps in Fig. 26 under the resonant excitation of the B-exciton. Another is an absorption saturation with a rise time about 400 fs as is observed in Fig. 27 under the resonant excitation of the A-exciton. Another is relatively flat time dependence as is observed in Figs. 27 and 28 under the

resonant excitation of the B-exciton. The temporal changes of  $\Delta\alpha$  at the picosecond region are also shown in Fig. 31.

The excitation-density dependent change in the absorption coefficient observed under the resonant excitation of the A-exciton are shown in Figs. 32 and 33. Figures 32 and 33 correspond to the spectra obtained at the 0 fs time delay and at the 150 fs time delay, respectively. With the increase in the excitation density, a structure between the A-exciton and the B-exciton is observed at the 0 fs time delay, but is not observed at the 150 fs time delay.

Figures 34 and 35 show the time dependence of change in absorption area,  $\Delta S$  observed under the excitation condition (3). Here,  $\Delta S$  is obtained by the spectral integration of each time-resolved spectrum. The spectrally integrated values of the bleaching,  $\Delta S_B$  and that of the induced absorption,  $\Delta S_A$  are shown by the solid lines and the dotted lines, respectively. Figure 34 shows the data in a short time range ( -1 to 1 ps ) and Fig. 35 shows the data in a long time range ( -2 to 12 ps ), respectively. The results observed under the excitation condition (4) are shown in Figs. 36 and 37. The results observed under the condition (5) are shown in Figs. 38 and 39.

Detailed discussions will be given in the section IV.

### III. Monte-Carlo simulation

Recently the advanced femtosecond spectroscopy, in particular the pump-and-white-continuum probe method, has clarified the carrier distribution at ultrafast time domain. However, some experimental results are difficult to be interpreted quantitatively because of complex scattering channels. Therefore, an ensemble Monte-Carlo simulation becomes a powerful method to interpret the experimental results.<sup>58-61)</sup> In the simulation, the time-dependent distribution functions are used to evaluate the time-resolved absorption spectrum.

At first, the carrier distribution corresponding to the real photoexcitation is generated by using the rejection method.<sup>58)</sup> Time dependence is simulated by using a constant time step method. Some scattering probabilities were calculated depending on each carriers' kinetic energy. In the simulation, electron-electron, electron-hole, hole-hole, electron-LO phonon and hole-LO phonon scattering mechanisms are considered. Carrier-carrier scattering probability is evaluated by the well-known formula,<sup>62-64)</sup>

$$1/\tau_{cc} = \frac{\mu^* e^2 k_B T_c}{8\pi\hbar^3 \epsilon_{vac} \epsilon_0} \cdot \frac{g}{g^2 + \beta^2} \quad (3.1)$$

This formalism is derived based on the the Born approximation with a screened Coulomb potential. The carriers are assumed to follow the Boltzmann distribution. Here,  $\mu^*$ ,  $e$ ,  $k_B$ ,  $T_c$ ,  $\hbar$ ,  $\epsilon_{vac}$ ,  $\epsilon_0$ ,  $g$  and  $\beta$  denote the reduced mass of a carrier pair, the

electron charge, the Boltzmann constant, the carrier temperature, the Planck constant divided by  $2\pi$ , the dielectric constant of vacuum, the static dielectric constant of CdSe, the relative momentum of scattering carriers and the screening wave vector, respectively. The screening wave vector,  $\beta$  is represented by

$$\beta = \left[ \frac{n_c e^2}{\epsilon_{\text{vac}} \epsilon_0 k_B T_c} \right]^{1/2} . \quad (3.2)$$

Here,  $n_c$  denotes the carrier density.

Strictly speaking, the carrier-carrier scattering rate and the screening wave vector depend on the distribution function of carriers.<sup>65)</sup> Initially, the photoexcited carriers do not obey the Boltzmann distribution, so that this formula is not correct. However, there are no theory to show the carrier-carrier scattering rate in nonequilibrium distribution, so that the formula was used as the first approximation.

The carrier-LO phonon scattering rate in the polar material is represented by<sup>34)</sup>

$$1/\tau_{c-LO} = \frac{2eE_0}{(2m^*E)^{1/2}} \left[ N_q \sinh^{-1} \left( \frac{E}{\hbar\omega_{LO}} \right)^{1/2} + (N_q + 1) \sinh^{-1} \left( \frac{E - \hbar\omega_{LO}}{\hbar\omega_{LO}} \right)^{1/2} \right] . \quad (3.3)$$

Here,  $m^*$ ,  $N_q$ ,  $\hbar\omega_{LO}$  and  $E$  denote the carrier effective mass, the phonon occupation number which is presented by the Bose distribution function, the LO phonon energy and the excess energy of

carriers. A factor  $eE_0$  presents the electric force caused by the oscillations of the LO phonons which is represented by

$$eE_0 = \frac{e^2 m^* \hbar \omega_{LO}}{4\pi \epsilon_{vac} \hbar^2} \left( \frac{1}{\epsilon_\infty} - \frac{1}{\epsilon_0} \right) \quad (3.4).$$

Here,  $\epsilon_\infty$  denotes the optical dielectric constant of CdSe.

Based on the above mentioned scattering rates, the time evolution of the electron and hole distributions was simulated. The way to do this is described as follows.

The sum of all the scattering rates,  $1/\tau_m$ , was calculated. Next, a random number  $R$  was generated. If the time step  $\Delta t$  is larger than  $R\tau_m$ , scattering does not occur. If  $\Delta t$  is smaller than  $R\tau_m$ , the scattering takes place. In order to decide which scattering process occurs, another random number  $R'$  was generated. When the  $j$ -th scattering with a scattering rate  $1/\tau_j$  takes place, the condition

$$\frac{\sum_{i=1}^{j-1} \tau_i}{\tau_m} < R' < \frac{\sum_{i=1}^j \tau_i}{\tau_m} \quad (3.5)$$

should be satisfied. In this way, the scattering type  $j$  was determined. The time step  $\Delta t$  should be equal to or smaller than the fastest scattering time.

When the carrier-carrier scattering takes place, each carriers' momenta and energies after the scattering were decided by using a random number. Of course in this case, the momentum conservation law and the energy conservation law hold. When the

carrier-LO phonon scattering takes place, the momentum and energy of scattering carrier were reduced or added by those of the LO phonon. In both cases above mentioned, the scattering rate after the scattering was recalculated. In this way, the time evolution of momenta and energies were simulated.

The results of the simulations are compared with the experimental data. The discussion will be given in the next section.

## IV. Discussions

### 4.1 Nonequilibrium distribution of photoexcited carriers

At first, the discussions about the results under the band-to-band excitation ( experimental condition (1)-(3) ) will be given. In this case, a lot of free carriers are generated by an intense optical pulse with the enough kinetic energy. The kinetic energy per carrier is an order of 100 meV. It depends on the difference between the band gap and the excitation photon energy.

Figures 5 to 8, 14 and 15 show the nonequilibrium distribution of photoexcited carriers around the time origin. To compare the experimental spectra with the simulated distribution function, the experimental spectra are shown in the form of  $-\Delta\alpha/\alpha$  in Figs. 7 and 8. The relation between  $-\Delta\alpha/\alpha$  and an electron ( a hole ) distribution function  $f_e(E_e)$  (  $f_h(E_h)$  ) is expressed by<sup>13,66)</sup>

$$-\Delta\alpha/\alpha = f_e(E_e) + f_h(E_h) . \quad (4.1.1)$$

Here,  $E_e$  and  $E_h$  are the kinetic energy of electrons and holes, respectively. The kinetic energies of electrons and holes are represented by

$$E_i = \mu/m_i ( E - E_g ) \quad ( i = e, h ) . \quad (4.1.2)$$

Here,  $\mu$ ,  $m_i$ ,  $E$  and  $E_g$  denote a reduced mass of an electron and a hole, an effective mass, the photon energy and the band gap, respectively. Equation (4.1.1) is based on an approximation. Strictly speaking, one must consider the Coulomb enhancement factor in the band-to-band absorption.

The absorption spectrum in the intrinsic semiconductors consists of the discrete exciton lines, quasi-continuum state below the band gap and true continuum state above the band gap.<sup>67)</sup> The absorption spectrum is presented as an interband absorption multiplied by the excitonic enhancement of the true continuum states above the band gap.<sup>68)</sup> However, we can justify the approximation, based on eq. (4.1.1) as follows.

At low temperature, the excitonic enhancement of the continuum state is affected by the high-density free carriers around the band edge. Above the band edge, the change in the optical spectrum is not so much. The result of this calculation is shown in Fig. 40.<sup>63)</sup> The detail of this calculation is described in the appendix. To discuss the high-density effect of the absorption spectra above the band gap, we may well omit the excitonic enhancement effect as the first approximation. Therefore, the absorption change in the band is considered to come from only the band filling effect at low temperature. At high temperature ( $\sim 300$  K), the excitonic enhancement in the band depends on the carrier density.<sup>69)</sup> However, the ratio between the bleaching caused by the band filling effect and that caused by the reduction of the excitonic enhancement is about 4:1, so that the reduction of the excitonic enhancement is considered to be neglected. In this approximation, the eqs. (4.1.1) and (4.1.2)

can well describe the experimental results. In the following discussion, both the equations will be used in the analysis.

In the Figs. 7 and 8, the estimated carrier density is an order of  $10^{19} \text{ cm}^{-3}$ . In the simulation, the same value of carrier density was used. Insert this value to eqs. (3.1)-(3.3), the typical carrier-carrier scattering rate is obtained as an order of femtoseconds. The value is shorter than our experimental time resolution. Figures 42 and 43 show the results of the Monte-Carlo simulation. Here, the dashed lines show the histograms of the electron distribution and the dotted lines that of the hole distribution, respectively. The solid lines represent the sum of both the distributions.

Initially, the electrons and the holes distribute around the excitation energy in the simulation. The initial distributions of the electron and the hole are the same. Therefore, only the sum of the electron distribution function and the hole distribution function is plotted in Fig. 42. At 50 fs time delay, the distributions of both carriers are nearly thermalized. However, the high energy tail of the electron distribution shows the nonthermalized feature. The part of the nonthermalized carriers is smaller than the results of the experiments. In order to discuss more quantitatively, it is necessary to improve the simulations.

We can estimate the thermalization time from the experimental results. A simple rate equation is written by,

$$dn/dt = g(t) - n/\tau_d \quad , \quad (4.1.3)$$

where  $n$ ,  $g(t)$  and  $\tau_d$  denote the carrier density, the generation rate of the photoexcited carriers and the decay rate. We can neglect the decay term because of the fairly long life time of carriers and assume that the initially generated carriers are nonthermalized. Then, the eq. (4.1.3) becomes

$$dn^n/dt = g(t) - n^n/\tau, \quad dn^e/dt = n^n/\tau, \quad (4.1.4)$$

where  $n^n$ ,  $n^e$  and  $\tau$  denote the nonthermalized carrier density, the thermalized carrier density and the thermalization time constant. If the generation rate is constant within the time resolution,  $\delta t$ , the nonthermalized carrier density at time  $\delta t$  is represented by

$$n^n(\delta t) = \int_{-\infty}^{\delta t} \frac{\delta n}{\delta t} \exp[(t' - \delta t)/\tau] dt' = \frac{\delta n}{\delta t} \tau. \quad (4.1.5)$$

Here,  $\delta n$  denotes the carrier density generated within the time resolution. Equation (4.1.5) shows that the thermalization time  $\tau$  is estimated to be  $\frac{n^n}{\delta n} \delta t$ .

From the experimental results, the ratio of the nonthermalized distribution to the total one is obtained as 10 % for the spectrum at 0 ps in 4.2 K and as 5 % in the room temperature. Therefore, 5 ~ 10 % of the present time resolution of 400 fs roughly gives the thermalization time of 20 ~ 40 fs.

## 4.2 Cooling of hot carriers

Cooling of hot carriers are observed in Figs. 7 to 10. In the analysis, we should take account of an anisotropy in the A-hole band. Then, the simple expression (4.1.1) is modified. In order to estimate the anisotropy effect in the cooling process of carriers, a simulation with and without the anisotropy is done.

The absorption spectrum is proportional to an imaginary part of the susceptibility, expressed as<sup>70)</sup>

$$\text{Im } \chi(E) \propto \left( \frac{2\mu}{\hbar^2} \right)^{3/2} (E-E_g)^{1/2} \theta(E-E_g) N(E-E_g) . \quad (4.2.1)$$

Here,  $E$ ,  $\mu^*$ , and  $E_g$  represent the photon energy, a reduced mass between an electron and a hole and the energy gap, respectively. The step function,  $\theta(E-E_g)$  means that there is not absorption below the band gap. The phase space filling effect is taken into account in term  $N(E-E_g)$ , which is represented by

$$N(E-E_g) = 1 - f(\alpha_e E - \mu_e) - f(\alpha_h E - \mu_h) . \quad (4.2.2)$$

Here,  $\mu_e$  and  $\mu_h$  represent the electron and the hole quasi-Fermi energies. The prefactors  $\alpha_e$  and  $\alpha_h$  mean  $\mu/m_e^*$  and  $\mu/m_h^*$ , respectively. The anisotropy in the band structures changes  $\mu$  and  $N(E-E_g)$ . By using the anisotropic masses of the electron ( $m_e^\perp$  and  $m_e^{\parallel}$ ) and the hole ( $m_h^\perp$  and  $m_h^{\parallel}$ ),  $N(E-E_g)$  is represented by,<sup>70)</sup>

$$N(E-E_g) = \int_0^1 ds \{ 1 - f([r+\eta s^2]E-\mu_e) - f([1-r-\eta s^2]E-\mu_h) \},$$

$$r = \frac{m_h^\perp}{m_e + m_h^\perp}, \quad \eta = \frac{m_h^{//}}{m_e^{//} + m_h^{//}}. \quad (4.2.3)$$

The effective masses of the electron and the hole are replaced by averaged values,  $m_e = (m_e^\perp m_e^{//})^{1/3}$ ,  $m_h = (m_h^\perp m_h^{//})^{1/3}$ . The calculated results of  $\text{Im } \chi(E)$  are shown in Fig. 41. The solid curve and the dashed curve are calculated results with and without anisotropy, respectively. The difference is very small. Therefore, it does not matter to neglect the anisotropy in the A-hole band. If we neglect the anisotropy, we can use the relation (4.1.1).

Further, we can approximately replace the right hand side of eq. (4.1.1) at the high energy tail by the larger one, because both  $f_e(E_e)$  and  $f_h(E_h)$  are the exponentially decaying functions at the high energy tail. Then, the analysis procedures become simple as follows. We analyzed the  $-\Delta\alpha/\alpha$  spectra by fitting the single Fermi distribution function,  $f_c(E) = 1/(\exp[(E-E_F)/k_B T_c] + 1)$ , where  $E_F$  is the chemical potential and  $T_c$  is the effective temperature of hot carriers. Almost all the spectra can be well fitted by the single Fermi distribution function  $f_c(E)$  except the spectra around the time origin. The spectra at 5 ps is well fitted by a single Fermi distribution function as shown in Figs. 7 and 8. At the later time range, the spectra are also well described by the Fermi distribution as shown in Figs. 9 and 10.

Therefore, the cooling of the hot carriers is characterized by the effective temperature of the hot carriers  $T_c$ . The temporal change of the temperatures are plotted in Figs. 44 and 45. The mean cooling rate of hot electrons and holes,  $\langle dE_e/dt \rangle$  and  $\langle dE_h/dt \rangle$ , are written by the equations,<sup>17)</sup>

$$\langle dE_e/dt \rangle = - E_{LO} / \tau_e \exp(-E_{LO}/k_B T_e) , \quad (4.2.4)$$

$$\langle dE_h/dt \rangle = - E_{LO} / \tau_h \exp(-E_{LO}/k_B T_h) , \quad (4.2.5)$$

where  $E_{LO}$  is the LO phonon energy of 26.3 meV and  $\tau_{e(h)}$  is the phonon emission time of hot electrons (holes), which is estimated from eq. (3.4). Electron and hole temperatures are represented by  $T_e$  and  $T_h$ , respectively. Numerical integration were done in eqs. (4.2.4) and (4.2.5), by using the approximate relations  $\langle E_e \rangle = (3/2)k_B T_e$  and  $\langle E_h \rangle = (3/2)k_B T_h$ .

The fitting of the experimental data was done in three ways. One is a cooling of hot electrons, where  $T_c$  is replaced by the electron temperature  $T_e = (\mu/m_e)T_c$ . Another is a cooling of hot A-band holes, where  $T_c$  is replaced by the A-hole temperature  $T_{hA} = (\mu/m_{hA})T_c$ . The third one is a cooling of hot B-band holes, where  $T_c$  is replaced by the B-hole temperature  $T_{hB} = (\mu/m_{hB})T_c$ . The best fitting is obtained in case of hot A-band holes. The results are shown in Figs. 44 and 45 by solid lines. The fitting is quite well. Then initial temperature of  $T_h$  and phonon emission time  $\tau_h$  are 220 K and 1.5 ps for Fig. 44 and 200 K and 2.0 ps for Fig. 45, respectively.

The obtained phonon emission time of 1.5 ps at 4.2 K and 2.0 ps at the room temperature are those of hot A-band holes. They are longer than 170 fs at 4.2 K for the A-band holes or 120 fs at 4.2 K for the electrons calculated by using eq. (3.4) by an order of magnitude. As mentioned before, CdSe has a single valley at the  $\Gamma$  point below 2.12 eV. Therefore, no intervalley scattering takes place. Hot electrons and holes lose their energy in the single valley by successive emission of the LO phonons as calculated by the Monte-Carlo simulation. It is well known that the holes lose their energy much faster than the electrons in GaAs.<sup>41,42,44)</sup> This fact was explained by considering that hot phonon effect reduces the electron cooling rate, while hardly reduces the hole cooling rate. The carriers interact so strongly at the high density of  $10^{19} \text{ cm}^{-3}$  that thermal equilibrium between the electrons and the holes is apt to be established. Therefore, slow cooling electrons heat fast cooling holes. The disagreement between the experimental phonon emission time and the theoretical one probably comes from the fast electron-hole scattering and the hot phonon effect.<sup>71)</sup>

Intuitively, the hot phonon effect is considered as follows. The high density photoexcited carriers with high excess-energy emit a lot of LO phonons. In this case, the phonon occupation number becomes large compared with that at the lattice temperature, so that the carriers are apt to absorb the LO phonons and be heated. Then the net energy flow from the carriers to the lattice becomes small. In this picture, the energy loss rate of carriers emitting the LO phonons is described by<sup>36,37)</sup>

$$\frac{dE_i}{dt} = \frac{e^2 m_i^2 k_B T_i}{4\pi^3 \epsilon_{vac} \hbar^5} \left( \frac{1}{\epsilon_\infty} - \frac{1}{\epsilon_0} \right) (\hbar \omega_{LO})^2 \times$$

$$\{ N_q(T_i) - N_q(T_L) \} \times \int_0^\infty \frac{q^3 dq}{(q^2 + \beta^2)^2} \times$$

$$\text{Log} \left[ \frac{1 + \exp(M_-)}{1 + \exp(M_+)} \right] \times \frac{1}{n_c}, \quad (4.2.6)$$

where,  $M_{\pm}$  is represented by,

$$M_{\pm} = \frac{-\hbar^2}{8m_i k_B T_i} \left[ q \pm \frac{2m_c \omega_{LO}}{\hbar q} \right]^2 + \frac{\mu_i}{k_B T_i}. \quad (4.2.7)$$

Here, the same notation is used as in section III, except for  $T_L$ .  $T_L$  denotes the bath temperature of the lattice.

When the carrier temperature is higher than 100 K, the energy loss rate at  $n_c = 10^{19} \text{ cm}^{-3}$  is smaller than that at  $n_c < 10^{15} \text{ cm}^{-3}$  by an order of magnitude.<sup>37)</sup> The LO phonon emission time obtained from the experiment is slower than the calculated one by an order of magnitude. The agreement between the experiment and calculation is fairly good.

Figures 11 and 12 show that the recovery time of bleaching at 4.2 K is comparable with that at the room temperature. The solid lines in the figures represent the phenomenological fitting curves, described by

$$-\Delta \alpha d = c [ 1 - \exp(-t/\tau_r) ] \exp(-t/\tau_d). \quad (4.2.8)$$

Here,  $\tau_r$  and  $\tau_d$  represent the rise time and the decay time, respectively. The value of  $c$  was also determined as a fitting parameter. The nonlinear-least-squared-fitting was done and all the parameters were obtained as a function of photon energy. Here, our attention is paid only to the cooling process, so that only the discussions about the decay time are given.

The results of the fitting are shown in Figs. 11 and 12 by the solid lines. The agreement between the data and the fitting curve is good. In Fig. 46, the obtained relaxation time constants are plotted as a function of the photon energy. Here, the solid line shows the relaxation time constants at 4.2 K and the dashed line shows those at the room temperature. The higher the photon energy is, the faster the relaxation time is. This fact is quite reasonable because the carrier cooling rate increases as the carrier kinetic energy increases.

As an interesting feature in Fig. 46, we can find a kink in the curve at room temperature. At the low energy side of the kink point, the hot carrier cooling rate becomes slow. The energy of the kink point is 1.828 eV. Figure 6 shows that the A-exciton energy at the room temperature is 1.760 eV. Taking account of the binding energy of the A-exciton ( $\sim 15$  meV), the energy of the kink point is higher than the band edge by 53 meV. This energy corresponds to twice of the LO phonon energy ( $\sim 26.3$  meV).

As already mentioned in the introduction, the fastest mechanism in the cooling processes of hot carriers is the LO phonon scattering. Therefore, in a simple model, the kink energy should be higher than the band gap by one LO phonon energy.

However, the situation is more complicated because the excess energy is shared by both an electron and a hole. The fact that the kink point is higher than the band gap by two LO phonon energy is considered as follows.

In a hot phonon model, the carriers hardly emit the LO phonons with a small wave vector, because of its small phase space. Therefore, the hot phonon effect reduces the electron cooling rate, but does not reduce the hole cooling rate.<sup>41)</sup> However, if the carrier emits two LO phonons simultaneously, the situation is very different. In this case, the hot phonon effect does not work effectively, because the carrier can emit the LO phonons with large momentum. Therefore, the cooling rate of carriers which is larger than the band gap by twice of the LO phonon energy is not affected by the hot phonon effect. This is the reason why the kink point is observed at the energy where the excess energy is twice of the LO phonon energy.

### 4.3 Common and different features observed in three pump-and-probe experiments

There are common features among three kinds of the excitation photon energy, 2.00 eV, 1.87 eV and 1.82 eV, which correspond to the experiments (3), (4) and (5), respectively.

As shown in Figs. 13, 19, and 22, the oscillated spectra are observed before the pump pulse hits the sample. This feature can be understood based on the optical Bloch equation.<sup>55-57)</sup> When the pump energy is below the exciton, the oscillation is a precursor of the optical Stark effect.<sup>55,57)</sup> Under the band-to-band excitation or the resonant excitation of the exciton, the oscillation is a precursor of the absorption saturation.

As shown in Figs. 14, 19 and 23, the dip at low energy side of the A-exciton is observed around the time origin and suddenly disappears after the pump pulse hits the sample. Such a transient broadening is observed in the GaAs quantum well system.<sup>47)</sup> The transient broadening of the exciton line is considered as follows.

When the probe pulse precedes the pump pulse, the coherent oscillation can be observed as already shown. When the pump pulse and the probe pulse hit the sample simultaneously, the transient broadening around the low energy side of the exciton is observed. However, the transient broadening disappears as soon as the bleaching occurs. This fact suggests that the excitation density where the broadening takes place is lower than that the bleaching takes place. Therefore, the broadening occurs before the bleaching takes place.

The time dependences of the broadening and the bleaching are more clearly seen in Figs. 34 and 36. In both the figures, the spectrally integrated bleaching,  $\Delta S_B$  and the spectrally integrated induced absorption,  $\Delta S_A$  are plotted as a function of the time delay. In Fig. 34, ( in the case of the band-to-band excitation )  $\Delta S_A$  decreases suddenly, because all the absorption spectra observed below the pump energy are bleached. In both the figures, the time delay where  $\Delta S_A$  reaches its minimum corresponds to the time delay where the increase of  $\Delta S_B$  finishes. This means that the induced absorption caused by the exciton broadening is quickly occupied by the cooled excitons or carriers.

On the other hand, in the case of the A-exciton resonant excitation, the time dependence of  $\Delta S_A$  is completely the same as that of  $\Delta S_B$ , as shown in Fig. 38 and 39. This fact indicates that the origin of the induced absorption and the bleaching in the A-exciton resonant excitation is the same. Detailed discussion about this case is given in the next subsection.

In the case of band-to-band excitation, the initial increase in the bleaching between 1.81 and 1.88 eV as shown in Fig. 17 is ascribed to carrier cooling. The carriers with the large kinetic energy relax to the low energy side with emitting LO phonons. Therefore, the bleaching at the low energy side increases. The increase or the decrease in the bleaching is determined by the balance between the coming of carriers from the high energy side and the going of carriers to the low energy side. This phenomenon was already studied by several authors in GaAs.<sup>27-29)</sup> However, there are the intervalley scattering in GaAs, so that the energy dependence of the cooling processes is more

complicated. On the other hand, there is no intervalley scattering in this energy region in CdSe, so that the simple cooling and the monotonous increase in bleaching is observed below 1.92 eV.

The interesting feature observed under the band-to-band excitation is the induced absorption at the higher energy side, as shown in Figs. 16 to 18. This feature is always observed in all the excitation energy. This is typically shown in Figs. 16, 21 and 25. Under the A-exciton resonant excitation, the induced absorption is well explained by considering the broadening of the B-exciton, but in other cases, the origins are not clearly understood. In case of the A-exciton excitation, the detailed discussions are given in the next subsection.

There is another characteristic difference between the A-exciton resonant excitation and the B-exciton resonant excitation. In the case of the A-exciton resonant excitation, the bleaching at the B-exciton increases as time precedes, as shown in Fig. 20. However, in the case of the B-exciton resonant excitation, the bleaching at the B-exciton decreases as the time proceeds from 150 fs to 600 fs. In the case of the band-to-band excitation, the bleaching at the B-exciton also increases as the time proceeds from 150 fs to 600 fs, as shown in Figs. 15 and 17.

This feature is more clearly seen in Fig. 27. In the case of the B-exciton resonant excitation, the carriers at the B-exciton energy show only cooling. Therefore, the bleaching at the B-exciton in this time region simply decreases. In the case of the A-exciton excitation, only the A-excitons are excited. However, both A-excitons and B-excitons are composed of common conduction band electrons, so that the bleaching at the B-exciton

is observed. The rise time of the B-exciton bleaching was found to be about 400 fs, as shown in Fig. 27.

The resonant excitation of the exciton system were studied in the GaAs quantum well system.<sup>47-49)</sup> In the room temperature, the excitons can be ionized by the LO phonon absorption.<sup>47,48)</sup> In this case, the ionization time of excitons was found to be about 300 fs. However, the excitons can not be ionized in CdSe at 10 K. Therefore, the rise at the B-exciton can not be considered as the exciton ionization. The reason why the B-exciton bleaching have a rise time under the resonant excitation of the A-exciton is discussed in the next subsection.

#### 4.4 A-exciton resonant excitation

In this subsection, discussions about the resonant excitation of the A-exciton are done.

The induced absorption at the low energy side of the A-exciton is considered to come from the broadening of the A-exciton, as already mentioned. On the other hand, what explains the induced absorption observed between the A-exciton and the B-exciton and above the B exciton? The induced absorption observed between the A-exciton and the B-exciton may come from the broadening of both the excitons. The induced absorption observed above the B-exciton may come from the broadening of the B-exciton. The time dependence of the induced absorption observed above the B-exciton structure is different from that observed below the A-exciton as shown in Figs. 26 and 30. Two explanations come to our mind as an origin of the induced absorption observed above the B-exciton.

One is a band gap renormalization ( BGR ). The BGR is considered as an origin of the induced absorption not only below the unperturbed band gap,<sup>72)</sup> but also in the band-to-band absorption. The other is a B-exciton broadening. However, the former explanation is omitted as follows.

Figure 47 shows the pure red-shift of the unperturbed absorption spectrum. In this figure, the induced absorption above the B-exciton is not observed. The result indicates that the induced absorption observed above the B-exciton can not be explained by BGR.

Figure 48 shows the excitation density dependence of  $\Delta S_B$  and  $\Delta S_A$  at the time origin. Figure 49 shows the same data obtained at 150 fs time delay. The integration was done between 1.814 eV and 1.828 eV for  $\Delta S_B$ . For  $\Delta S_A$  the integration was done between 1.885 eV and 2.000 eV. As shown in Figs. 32 and 33, the positive region is taken to be the integration range for  $\Delta S_B$  and the negative region for  $\Delta S_A$ , respectively. In Figs. 48 and 49, the solid circles represent  $\Delta S_B$  and the solid squares  $\Delta S_A$ , respectively. The results show that,  $\Delta S_B$  in both figures obeys the expression as<sup>73)</sup>

$$\alpha = \alpha_2 + \frac{\alpha_1}{1 + I_{\text{ex}}/I_s} . \quad (4.4.1)$$

Here,  $I_{\text{ex}}$  and  $I_s$  denote the excitation density and the saturation density, respectively. The sum,  $\alpha_1 + \alpha_2$  represents the unperturbed absorption coefficient, and  $\alpha_2$  is the absorption coefficient at high density excitation limit. This result indicates that the bleaching at 0 and 150 fs is well explained by the usual absorption saturation caused by the phase space filling. The bleaching area at 0 fs is smaller than that at 150 fs. This is quite reasonable, because the absorption saturation is caused by the leading edge of the excitation pulse at 0 fs .

The absorption area of the B-exciton is estimated to be between 300 and 600  $\text{eV}\cdot\text{cm}^{-1}$  from the unperturbed spectrum. If the induced absorption comes from the broadening of the B-exciton,  $\Delta S_A$  should be smaller than this value. Figures 48 and 49 show that the values of  $\Delta S_A$  are between 100 and 200  $\text{eV}\cdot\text{cm}^{-1}$ . The values are reasonable.

The broadening of the excitonic line tells us a scattering time of the exciton. The spectral shape of an absorption line caused by the collisional broadening is represented by a Lorentzian function.<sup>74)</sup> In this case, the relation between the energy width,  $\Delta E$  and the mean scattering time,  $\tau$  is expressed by

$$\Delta E \tau \sim 2\hbar . \quad (4.4.2)$$

From this equation, we can estimate the exciton-exciton scattering time. In order to obtain the energy broadening,  $\Delta E$  we fitted the calculated spectrum to the experimental spectrum,  $-\Delta\alpha$ . In the fitting, we did not obtain the sufficient agreement when we take account of only the B-exciton broadening. The agreement was improved when both the broadening of the A-exciton and the B-exciton is taken into account, as shown in Fig. 50. Initially, the broadening of the A-exciton was observed below the A-exciton peak, as shown in Fig. 19. Therefore, the broadening of the A-exciton surely occurs. The broadening below the A-exciton disappears as soon as the bleaching becomes large. However, the broadening observed above the A-exciton probably remains and is independent of the bleaching. Therefore, it is quite reasonable to take account of the broadening of the A-exciton.

As a result of fitting, the energy broadening of the B-exciton and the A-exciton were found to be about 42 and 27 meV, respectively. Inserting these values to eq. (4.4.2), we obtained the mean scattering time between the B-exciton and the A-exciton, 31 fs. We also obtained the mean scattering time between the A-exciton and the A-exciton, 49 fs.

The exciton-exciton scattering rate can be estimated from a simple theory. Excitons have no charge, so that we consider the scattering mechanism of excitons on the model of rigid-spheres scattering. Initially, the photoexcitation generates the A-excitons with zero translational momentum. Then, the photoexcited A-excitons are thermalized at the lattice temperature and obey the Boltzmann distribution. The B-excitons generated by a probe pulse collide with the A-excitons. In this case, the A-exciton and B-exciton mutual scattering rate  $1/\tau_{A-B}$  is represented by,

$$1/\tau_{A-B} = 2n_{ex} (a_{AB} + a_{BB})^2 (2\pi k_B T_L / \mu_{AB})^{1/2} . \quad (4.4.4)$$

Here,  $n_{ex}$ ,  $\mu_{ex}$ ,  $a_{AB}$  and  $a_{BB}$  denote the A-exciton density, the reduced mass between the translational mass of the A-exciton and that of the B-exciton, Bohr radius of the A-exciton and that of the B-exciton, respectively. In the experimental condition, the value of  $n_{ex}$  and  $T_L$  are  $1 \times 10^{19} \text{ cm}^{-3}$  and 10 K, respectively. The calculated scattering time is 11 fs. The agreement between the observed 31 fs and estimated 11 fs is good. Therefore, the broadening of the B-exciton resonance is well explained by the A-exciton-B-exciton collisional broadening. As already mentioned in the previous subsection, the B-exciton bleaching increases with 400 fs rise time, as shown in Fig. 27. As an origin of the rise time, two explanations are considered as follows. One is ascribed to the thermalization time between the exciton's motion and bath temperature. The other is the change of the exciton

phase-space. In order to solve the problem, further studies are needed.

With the increase in the excitation density, a small structure is observed just above the A-exciton energy, as shown in Fig. 32. We took a derivatives of the curves, the energy of the structure is found to be 1.842 eV. This energy is covered by the pump pulse. This structure is diminished as soon as the excitation pulse turns off. Actually, the structure is not observed in Fig. 33, where the time delay is 150 fs. The origin of the structure may come from the spectral hole burning.

#### 4.5 B-exciton resonant excitation

In case of the resonant excitation of the B-exciton, both the B-excitons and the free carriers are generated. The free carriers are excited from the A-hole band to the conduction band. Therefore, we must consider the effects due to both the carriers.

There are several characteristic features in case of the resonant excitation of the B-exciton. One is an induced absorption with a rise time of 1.7 ps observed above the B-exciton, as shown in Fig. 26. When we determine the rise time, we omitted the spikelike structure around the time origin. The induced absorption is explained as follows.

As soon as the pump pulse comes in, the transient broadening of the B-exciton occurs. At that time, the induced absorption at the time origin in Fig. 26 is observed. Next, the photoexcited carriers spread out in the momentum-energy space by the carrier-carrier scattering. Therefore, the bleaching was observed above the excitation energy. This phenomenon corresponds to a transient recovery in Fig. 26. After that, the carrier cooling takes place. As a result, the bleaching disappears and only the broadening of the B-exciton remains. Therefore, the rise time ( 1.7 ps ) in Fig. 26 is considered to be carrier cooling.

Figures 28 to 30 show the time dependence of the change in the absorption,  $-\Delta\alpha$  observed below the pump energy. In contrast with the results under the band-to-band excitation as shown in Fig. 17, the bleaching at both the A-exciton and the B-exciton energies after the pump takes place promptly. Here, we refer to

the mechanisms of the exciton bleaching before we consider about this results.

In 3D system, the dominant contribution on the exciton bleaching comes from the screening of the Coulomb interaction.<sup>15)</sup> There is another contribution to the exciton bleaching caused by the phase space filling effect. The screening of the Coulomb interaction depends on the carrier temperature.<sup>3,75,76)</sup> The cold carriers screen the Coulomb interaction much effectively compared with the hot carriers. Therefore, some part of the increase in the exciton bleaching comes from the phase space filling, and other part comes from the screening effect and the carrier cooling. The most plausible reason why the gradual increase of the exciton bleaching is not observed under the B-exciton resonant excitation is suggested as follows.

Under the resonant excitation of the B-exciton, not only the free carriers but also the B-excitons are generated. The A- and the B-excitons have a common conduction band, so that the phase space filling on the conduction band is considered to be effective. Therefore, the bleaching at the A-exciton shows no rise.

Figures 27 and 28 show that the bleaching observed around the time origin shows the flat time dependence. Such a flat region was not observed at the A-exciton energy, as shown in Fig. 29. As already mentioned, the bleaching observed at the A-exciton under the B-exciton resonant excitation takes place promptly. This result is different from that observed under the band-to-band excitation. Therefore, the flat time dependence is

not explained by a simple carrier cooling. We cannot understand the actual origin of this structure.

The recovery time of the B-exciton's bleaching was faster than that under the A-exciton resonant excitation and that under the band-to-band excitation. Figures 16, 21 and 25 show this feature. More clearly, Figs. 18 and 31 show the results. Under the band-to-band excitation the time delay where the bleaching becomes the half of its maximum value was 5.3 ps, as shown at the 1.87 eV time trace in Fig. 18. Under the resonant excitation of the B-exciton, this time was 1.8 ps, as shown at the 1.86 eV time trace in Fig. 31. This time is much longer than 10 ps observed under the resonant excitation of the A-exciton, as shown in Fig. 31. The reason why this time constant is so fast under the B-exciton resonant excitation is considered as follows. The photoexcited carriers quickly spread out in the momentum-energy space. In case of the B-exciton resonant excitation, the pump photon energy is the same with the B-exciton resonance, so that the carriers spread out from the B-exciton energy. The other explanation is a fast scattering process from the B-hole band to the A-hole band.

## V. Conclusions

In this work, ultrafast pump-and-white-continuum-probe spectroscopy was adopted to study the dynamical behavior of photogenerated carriers in a CdSe thin film. As a result, the dynamics of the photogenerated carriers in CdSe is clarified as follows.

Under the band-to-band excitation, nonthermalized hot carrier distribution was observed when the pump pulse turns on. The duration of the nonthermalized feature could not be resolved in the experiment, but the ratio of the nonthermalized distribution to the total one gives the thermalization time of 20-40 fs.

In the cooling process of photogenerated hot carriers, hot carriers lose their excess energy by emitting the LO phonons keeping the thermalized distribution. From the time resolved absorption spectra, the time dependence of the distribution function was determined. As a result, the carrier-LO phonon scattering time is estimated to be 1.5-2.0 ps. The values are slower than those estimated from Frölich interaction by an order of magnitude. The observed slow cooling time is due to the hot phonon effect of the electrons and rapid thermalization between the electrons and holes.

In the pump-and-probe experiment, the pump photon energy was widely changed and the pump energy dependence was studied. Through the study, the common and different features are clarified. One of the common features is the coherent oscillation around the exciton resonance before the pump pulse hits the sample. Another is a transient broadening of the A-exciton

around the time origin. This feature is diminished as soon as the bleaching becomes large. The third one is an induced absorption in the band-to-band absorption region.

Under the resonant excitation of the A-exciton, the small bleaching with 400 fs rise time and the broadening were observed for the B-exciton. From the observed broadening, the A-exciton-B-exciton scattering time is estimated to be 31 fs. This value is well explained by the rigid-spheres scattering model. This fact clarifies the information about the exciton dynamics in the femtosecond domain.

Under the resonant excitation of the B-exciton, the instantaneous induced absorption and its prompt recovery was observed. This spikelike temporal structure is well explained by the broadening of the B-exciton and the fast carrier scattering in the momentum-energy space. The scattered carriers cool down to lower energy and only the broadening of the B-exciton was remained. The cooling time was about 1.7 ps.

The time dependence of the bleaching at the A-exciton observed under the B-exciton resonant excitation was different from that observed under the band-to-band excitation. The difference suggests the phase space filling of the conduction band.

Further experimental and theoretical works are necessary for the full understanding of the ultrafast scattering processes in solids.

## Acknowledgements

The author express a deep sense of gratitude to Prof. Y. Masumoto for the introduction to solid state physics, for that to the optical experiment including various kinds of ultrafast laser spectroscopies and for the helpful instruction of his study. He is also grateful to Profs. H. Fujiyasu and A. Ishida and their coworkers at University of Shizuoka for the kind guidance of hot wall epitaxy. He wishes to acknowledge to Prof. N. Peyghambarian and his coworkers at the University of Arizona for the fruitful discussions and help of the experiments during the international joint research. Some parts of this thesis were performed in the course of the joint research. Especially, Drs B. Fluegel and K. Meissner always helped the author in the experiments and analysis of the data during the joint research. The author would like to thank to Dr. I. Arai for the kind explanation of the Monte-Carlo simulation. He also acknowledges to emeritus Prof. E. Matuura and members of his laboratory for the initial-stage practice of the experimental physics. In the end, he wishes to express his acknowledgement to all the members in the research group of Prof. Y. Masumoto, Dr. Y. Kanemitsu for the kind encouragement, Dr. T. Mishina for the fruitful discussions and collaboration, and all students for the help of the experiments and the analysis. This work was partly supported by the Scientific Research Grant-in-Aid No.02952058 from the Ministry of Education, Science and Culture of Japan. The author thanks to Fellowships of the Japan Society for the Promotion of Science for Japanese Junior Scientists for the financial support.

## Appendix

Optical absorption coefficient  $\alpha(E)$  is represented by

$$\alpha(E) = \frac{E}{n(E)\hbar c} \text{Im } \chi(E) . \quad (\text{a.1})$$

Here,  $E$ ,  $n(E)$ ,  $c$  and  $\chi(E)$  denote the photon energy, the refractive index of the material, the light velocity and imaginary part of susceptibility. The imaginary part of the susceptibility is represented by

$$\text{Im } \chi(E) = 2\pi \sum_{\mathbf{v}} r_{\text{cv}}^2 \sum_{\mathbf{k}} [1 - f_e(\mathbf{k}) - f_h(\mathbf{k})] \delta\left(E - E_{\text{gv}} - \frac{\hbar^2 \mathbf{k}^2}{2\mu_{\mathbf{v}}}\right) , \quad (\text{a.2})$$

in the case of interband transition. The sum  $\mathbf{v}$  is done through all the valence bands concerning to the photoexcitation. Here,  $r_{\text{cv}}$  and  $\delta(E)$  is the matrix element of the interband transition and the delta-function, respectively. Other notation is the same as used in the text.

Equation (a.2) is the simplest expression for  $\text{Im } \chi(E)$ . We must take into account of Coulomb interaction between electrons and holes. As a result, the excitonic enhancement at band edge appears. At zero temperature  $\text{Im } \chi(E)$  is represented by

$$\text{Im } \chi(E) = 2\pi \sum_{\mathbf{v}} r_{\text{cv}}^2 \sum_{\lambda} |\phi_{\lambda}(\vec{\mathbf{r}}=0)|^2 \delta(E - E_{\text{gv}} - E_{\lambda}) . \quad (\text{a.3})$$

Here,  $\vec{\mathbf{r}}$ ,  $\phi_{\lambda}$ , and  $E_{\lambda}$  denote the coordinate of the relative motion between an electron and a hole, the eigenfunction and the

eigenenergy of a Wannier equation. This formula is well-known as an Elliot formula. In the general case, one should take account of this Coulomb interaction at the finite temperature and the finite carrier density. To solve the Wannier equation at the finite temperature and the finite carrier density, one must use a Bethe-Salpeter equation for the electron-hole pair function. However, there is a simple analytical form which evaluate the imaginary part of the susceptibility.<sup>65)</sup> In this formalism, eq. (a.2) and (a.3) are simply combined. The eqs. (a.2) is replaced by  $2\pi r_{cv} A(E)$ , where  $A(E)$  is represented by

$$A(E) = \tanh\left(\frac{E - \mu_e - \mu_h}{2k_B T_c}\right). \quad (a.4)$$

In this approximation, the formula,

$$\text{Im } \chi(E) = 2\pi r_{cv} A(E) \sum_{\lambda} |\phi_{\lambda}(\vec{r}=0)|^2 \delta(E - E_{gv} - E_{\lambda}), \quad (a.5)$$

is obtained.

In order to get an analytical form of  $\text{Im } \chi(E)$ , we replace the screened Coulomb potential in the Wannier equation by the Hulthen potential, and obtain a final form

$$\begin{aligned} \text{Im } \chi(E) = & \tilde{\epsilon} \tanh\left[\frac{\tilde{E}/\tilde{T} - \tilde{\mu}_e - \tilde{\mu}_h}{2}\right] \times \\ & \left\{ \sum_{l=1}^{ng} \pi \delta_{\Gamma}\left(\tilde{E} + [1/l - 1/g]^2\right) \times 2(g-1^2)(2l^2 - g)/l^3 g^2 \times \right. \\ & \prod_{n=1}^{\infty} \frac{n^2 [n^2 l^2 - (g-1^2)^2]}{(n^2 - 1^2)(n^2 l^2 - g^2)} + \\ & \left. \int_0^{\infty} dx x^{1/2} \prod_{n=1}^{\infty} \left[ 1 + \frac{2gn^2 - g^2}{(n^2 - g)^2 + n^2 g^2 x} \right] \delta_{\Gamma}(x - \tilde{E}) \right\} \quad (a.6) \end{aligned}$$

Here, all the parameters are written in dimensionless units as represented by,

$\tilde{\epsilon} = r_{cv}/2\pi a_B^3 E_R$ ,  $\tilde{E} = (E - E_g)/E_R$ ,  $\tilde{T} = k_B T/E_R$ ,  $\tilde{\mu}_i = \mu_i/k_B T$  ( $i=e, h$ ), respectively. A parameter  $g$  is derived from the Hulthen potential, and is described by  $g = 12/\pi a_B \kappa$ . The screening vector,  $\kappa$  is a function of the carrier distribution and is represented by,

$$\kappa^2 = \frac{4\tilde{T}^{1/2}}{\pi a_B^2} \int_0^\infty dx x^{1/2} \sum_i \tilde{m}_i^{3/2} f(x - \tilde{\mu}_i) [1 - f(x - \tilde{\mu}_i)] ,$$

(a.7)

where,  $\tilde{m}_i$  is the effective mass normalized by the reduced mass. The line broadening function  $\delta_\Gamma(x)$  is chosen as  $1/[\pi\Gamma \cosh(x/\Gamma)]$  in order to produce an exponential low-energy tail, which is called Urbach tail. The results of the calculation are shown in Fig. 40.

## References

- (1) Ultrashort light pulses, edited by S. L. Shapiro (Springer-Verlag, New York, 1977).
- (2) Ultrashort laser pulses, edited by W. Kaiser (Springer-Verlag, New York, 1988).
- (3) Optical Nonlinearities and instabilities in semiconductors, edited by H. Haug (Academic, New York-Boston, 1988).
- (4) D. Fröhlich, A. Nöthe and K. Reimann, Phys. Rev. Lett. 55, 1335 (1985).
- (5) A. Mysyrowicz, D. Hulin, A. Antonetti, A. Migus, W. T. Masselink and H. Morkoç, Phys. Rev. Lett. 56, 2748 (1986).
- (6) S. Schmitt-Rink and D. S. Chemla, Phys. Rev. Lett. 57, 2752 (1986).
- (7) M. Yamanishi, Phys. Rev. Lett. 59, 1014 (1987).
- (8) D. S. Chemla, D. A. B. Miller and S. Schmitt-Rink, Phys. Rev. Lett. 59, 1018 (1987).
- (9) D. Fröhlich, R. Wille, W. Schlapp and G. Weimann, Phys. Rev. Lett. 59, 1748 (1987).
- (10) N. Peyghambarian, S. W. Koch, M. Lindberg, B. Fluegel and M. Joffre, Phys. Rev. Lett. 62, 1185 (1989).
- (11) W. H. Knox, D. S. Chemla, D. A. B. Miller, J. B. Stark, S. Schmitt-Rink, Phys. Rev. Lett. 62, 1189 (1989).
- (12) D. H. Auston, Phys. Today, 46 (1990).
- (13) J. Shah, R. F. Leheny and C. Lin, Solid State Commun. 18, 1035 (1976).
- (14) J. Shah, R. F. Leheny and W. Wiegmann, Phys. Rev. B16, 1577 (1977).

- (15) C. V. Shank, R. L. Fork, R. F. Leheny and J. Shah, Phys. Rev. Lett. 42, 112 (1979).
- (16) R. F. Leheny, J. Shah, R. L. Fork, C. V. Shank and A. Migus, Solid State Commun. 31, 809 (1979).
- (17) D. von der Linde and R. Lambrich, Phys. Rev. Lett. 42, 1090 (1979)
- (18) C. L. Tang and D. J. Erskine, Phys. Rev. Lett. 51, 840 (1983)
- (19) J. L. Oudar, A. Migus, D. Hulin, G. Grillon, J. Etchepare and A. Antonetti, Phys. Rev. Lett. 53, 384 (1984).
- (20) J. L. Ouder, D. Hulin, A. Migus, A. Antonetti and F. Alexandre, Phys. Rev. Lett. 55, 2074 (1985).
- (21) D. J. Erskine, A. J. Taylor and C. L. Tang, Appl. Phys. Lett. 45, 1209 (1984).
- (22) A. J. Taylor, D. J. Erskine and C. L. Tang, J. Opt. Soc. Am. B2, 663 (1985).
- (23) W. Z. Lin, R. W. Schoenlein, S. D. Brorson, J. G. Fujimoto, E. P. Ippen, in Proceedings of the 15th International Quantum Electronics Conference IQEC '87, Baltimore, Maryland, April 1987, TUJJ2.
- (24) C. H. Brito-Cruz, R. L. Fork, C. V. Shank, in Proceedings of the 15th International Quantum Electronics Conference IQEC '87, Baltimore, Maryland, April 1987, TUJJ3.
- (25) W. H. Knox, C. Hirlimann, D. A. B. Miller, J. Shah, D. S. Chemla and C. V. Shank, Phys. Rev. Lett. 56, 1191 (1986).
- (26) W. H. Knox, D. S. Chemla, G. Livescu, J. E. Cunningham and J. E. Henry, Phys. Rev. Lett. 61, 1290 (1988).

- (27) M. J. Rosker, F. W. Wise and C. L. Tang, Appl. Phys. Lett. 49, 1726 (1986).
- (28) W. Z. Lin, J. G. Fujimoto, E. P. Ippen and R. A. Logan, Appl. Phys. Lett. 50, 124 (1987).
- (29) W. Z. Lin, J. G. Fujimoto, E. P. Ippen and R. A. Logan, Appl. Phys. Lett. 51, 161 (1987).
- (30) P. C. Becker, H. L. Fragnito, C. H. Brito Cruz, J. Shah, R. L. Fork, J. E. Cunningham, J. E. Henry and C. V. Shank, Appl. Phys. Lett. 53, 2089 (1988).
- (31) W. Z. Lin, W. Schoenlein, J. G. Fujimoto and E. P. Ippen, IEEE J. Quantum Electron. 24, 267 (1988)
- (32) N. Peyghambarian and S. W. Koch, Rev. Phys. Appl. 22, 1711 (1987).
- (33) P. C. Becker, H. L. Fragnito, C. H. Brito Cruz, R. L. Fork, J. E. Cunningham, J. E. Henry, and C. V. Shank, Phys. Rev. Lett. 61, 1647 (1988).
- (34) E. M. Conwell, in Solid State Physics, edited by F. Seitz, D. Turnbull and H. Ehrenreich (Academic, New York, 1967), suppl. 9.
- (35) R. Ulbrich, Phys. Rev. B8, 5719 (1973).
- (36) S. M. Kogan, Sov. Phys. Solid State, 4, 1813 (1963).
- (37) M. Pagnet, J. Collet and A. Cornet, Solid State Commun. 38, 531 (1981).
- (38) J. Collet, A. Cornet, M. Pagnet and T. Amand, Solid State Commun. 42, 883 (1982).
- (39) W. Pötz and P. Kocevar, Phys. Rev. B28, 7040 (1982).
- (40) P. Kocevar, Physica 134B, 155 (1985).

- (41) J. Shah, A. Pinczuk, A. C. Gossard and W. Wiegmann, Phys. Rev. Lett. 54, 2045 (1985).
- (42) S. A. Lyon, J. Lumin. 35, 121 (1986).
- (43) K. Leo, W. W. Rühle and K. Ploog, Phys. Rev. B38, 1947 (1988).
- (44) J. Shah, IEEE J. Quantum Electron. QE-22, 1728 (1986).
- (45) G. W. Fehrenbach, W. Schafer, J. Treusch and R. G. Ulbrich, Phys. Rev. Lett. 49, 1281 (1982).
- (46) G. W. Fehrenbach, W. Schäfer and R. G. Ulbrich, J. Lumin. 30, 154 (1985).
- (47) N. Peyghambarian, H. M. Gibbs, J. L. Jewell, A. Antonetti, A. Migus, D. Hulin and A. Mysyrowicz, Phys. Rev. Lett. 53, 2433 (1984).
- (48) W. H. Knox, R. L. Fork, M. C. Downer, D. A. B. Miller, D. S. Chemla, C. V. Shank, A. C. Gossard and W. Wiegmann, Phys. Rev. Lett. 54, 1306 (1985).
- (49) L. Schultheis, J. Kuhl, A. Honold and C. W. Tu, Phys. Rev. Lett. 57, 1635 (1986).
- (50) R. L. Fork, B. I. Greene and C. V. Shank, Appl. Phys. Lett. 41, 671 (1981)
- (51) R. L. Fork, C. V. Shank and R. Yen, Appl. Phys. Lett. 41, 223 (1982)
- (52) A. Migus, J. L. Martin, R. Astier, A. Antonetti and A. Orszag, in Picosecond Phenomena III, p. 6, ed. by K. B. Eisenthal, R. M. Hochstasser, W. Kaiser and A. Lauberau (Springer-Verlag, New York, 1982)
- (53) D. Grischkowsky and A. C. Balant, Appl. Phys. Lett. 41, 1 (1982)

- (54) H. Fujiyasu and K. Murase, in special issue on "Superlattices and Multilayers", Solid State Physics, 21, 469 (1986). (In Japanese)
- (55) B. Fluegel, N. Peyghambarian, G. Olbright, M. Lindberg, S. W. Koch, M. Joffre, D. Hulin, A. Migus and A. Antonetti, Phys. Rev. Lett. 59, 2588 (1987).
- (56) M. Lindberg and S. W. Koch, Phys. Rev. B38, 7607 (1988).
- (57) J. P. Sokoloff, M. Joffre, B. Fluegel, D. Hulin, M. Lindberg, S. W. Koch, A. Migus, A. Antonetti and N. Peyghambarian, Phys. Rev. B38, 7615 (1988).
- (58) for review of the ensemble Monte-Carlo simulation, see C. Jacobini and L. Reggiani, Rev. Mod. Phys. 55, 645 (1983).
- (59) S. M. Goodnich and P. Lugli, Phys. Rev. B37, 2578 (1988).
- (60) C. J. Stanton, D. W. Bailey and K. Hess, Phys. Rev. Lett. 65, 231 (1990).
- (61) D. W. Bailey, C. J. Stanton and K. Hess, Phys. Rev. B42, 3423 (1990).
- (62) A. Hasegawa and J. Yamashita, J. Phys. Soc. Jpn. 17, 1751 (1962).
- (63) A. Matulionis, J. Požela and A. Reklaitis, Solid State Commun. 16, 1133 (1975).
- (64) R. Brunetti, C. Jacobini, A. Matulionis and V. Dienys, Physica, B134, 369 (1985).
- (65) L. Bányai and S. W. Koch, Z. Phys. B63, 283 (1986).
- (66) D. H. Auston, S. McAfee, C. V. Shank, E. P. Ippen and O. Teschke, Solid State Electron. 21, 147 (1978).
- (67) R. J. Elliott, Phys. Rev. 108, 1384 (1957).

- (68) J. O. Dimmock, in "semiconductors and Semimetals. Vol. 3, Optical Properties of III-V compounds", ed. by R. K. Willardson and A. C. Beers ( Academic Press, New York, 1967 ).
- (69) Y. H. Lee, A. Chavez-Pirson, S. W. Koch, H. M. Gibbs, S. H. Park, J. Morhange, A. Jeffery, L. Bányai, A. C. Gossard and W. Wiegmann, Phys. Rev. Lett. 57, 2446 (1986).
- (70) R. Zimmermann, "Many-Particle Theory of Highly Excited Semiconductors", ( Teubner, Leipzig, 1988).
- (71) Y. Masumoto and F. Sasaki, J. Lumin. 47, 235 (1990) [ in press ].
- (72) F. Sasaki and Y. Masumoto, J. Phys. Soc. Jpn. 59, 1150 (1990).
- (73) D. A. B. Miller, D. S. Chemla, D. J. Eilenberger, P. W. Smith, A. C. Gossard and W. T. Tsang, Appl. Phys. Lett. 41, 679 (1982).
- (74) for example, "Introduction to Optical Electronics" third edition, edited by A. Yariv ( Holt-Saunders, New York, 1971 ).
- (75) M. Rösler, R. Zimmermann and W. Richert, Phys. Stat. Sol. B121, 609 (1984).
- (76) S. Schmitt-Rink, D. S. Chemla and D. A. B. Miller, Phys. Rev. B32, 6601 (1985).

## Figure captions

Fig. 1 Time delay vs. wavelength caused by the group velocity dispersion in the experiment (1). ( see text )

Fig. 2 Time delay vs. wavelength caused by the group velocity dispersion in the experiment (2). ( see text )

Fig. 3 Time delay vs. wavelength caused by the group velocity dispersion in the experiments (3) to (5). ( see text )

Fig. 4 The illustration of the hot-wall-epitaxy equipment.

Fig. 5 Time-resolved absorption spectra of CdSe observed under the 2.12 eV excitation at 4.2 K. The spectrum denoted by "NO PUMP" shows the spectrum without the pump. The pump-and-probe spectra at 0 ps, 5 ps and 12 ps time delays are shown.

Fig. 6 Time-resolved absorption spectra of CdSe observed under the 2.12 eV excitation at the room temperature. The spectrum denoted by "NO PUMP" shows the spectrum without the pump. The pump-and-probe spectra at 0 ps, 5 ps and 12 ps time delays are shown.

Fig. 7 The change in the absorption coefficient divided by the unperturbed absorption coefficient,  $-\Delta\alpha/\alpha$  observed under the 2.12 eV excitation at 4.2 K. The left part shows  $-\Delta\alpha/\alpha$  in the linear scale, and the right part shows  $-\Delta\alpha/\alpha$  in the logarithmic scale.

The effective temperature of the hot carriers  $T_c$  is estimated from the distribution and the fitting shown by dashed lines. The values of  $T_c$  for spectra at 0 ps, 0.6 ps and 5 ps are 970 K, 850 K and 540 K, respectively.

Fig. 8 The change in the absorption coefficient divided by the unperturbed absorption coefficient,  $-\Delta\alpha/\alpha$  observed under the 2.12 eV excitation at the room temperature. The left part shows  $-\Delta\alpha/\alpha$  in the linear scale, and the right part shows  $-\Delta\alpha/\alpha$  in the logarithmic scale. The effective temperature of the hot carriers  $T_c$  is estimated from the distribution and the fitting shown by dashed lines. The values of  $T_c$  for spectra at 0 ps, 0.6 ps and 5 ps are 1100 K, 860 K and 560 K, respectively.

Fig. 9 The change in the absorption coefficient divided by the unperturbed absorption coefficient,  $-\Delta\alpha/\alpha$  observed under the 2.12 eV excitation at 4.2 K. The figure shows the spectra observed at the late time ( solid lines ). The vertical scale is logarithmic one. The fitted Fermi distribution functions are shown by dashed lines. The effective temperature of hot carriers  $T_c$  for spectra at 4 ps, 8 ps and 12 ps are 580 K, 440 K and 390 K, respectively.

Fig. 10 The change in the absorption coefficient divided by the unperturbed absorption coefficient,  $-\Delta\alpha/\alpha$  observed under the 2.12 eV excitation at the room temperature. The figure shows the spectra at the late time ( solid lines ). The vertical scale is logarithmic one. The fitted Fermi distribution functions are shown by dashed lines. The effective temperature of hot carriers

$T_c$  for spectra at 4 ps, 8 ps and 12 ps are 590 K, 460 K and 400 K, respectively.

Fig. 11 The absorption change normalized by the unperturbed absorption coefficient,  $-\Delta\alpha/\alpha$  as a function of the time delay observed under the 2.12 eV excitation at 4.2 K. All dots represent the experimental data and the solid lines represent the fitting curves. The probe energy of each trace is shown in the figure.

Fig. 12 The absorption change normalized by the unperturbed absorption coefficient,  $-\Delta\alpha/\alpha$  as a function of the time delay observed under the 2.12 eV excitation at the room temperature. All dots represent the experimental data and the solid lines represent the fitting curves. The probe energy of each trace is shown in the figure.

Fig. 13 The change in the absorption coefficient,  $-\Delta\alpha$  observed under the 1.99 eV excitation at 10 K. Each curve is normalized by the respective maximum value. The time delay of each spectrum is shown in the figure. The lowest curve shows the pump laser spectrum.

Fig. 14 The change in the absorption coefficient,  $-\Delta\alpha$  observed under the 1.99 eV excitation at 10 K. Each curve is normalized by the respective maximum value. The time delay of each spectrum is shown in the figure. The lowest curve shows the pump laser spectrum.

Fig. 15 The change in the absorption coefficient,  $-\Delta\alpha$  observed under the 1.99 eV excitation at 10 K. The time delay of each spectrum is shown in the figure.

Fig. 16 The change in the absorption coefficient,  $-\Delta\alpha$  observed under the 1.99 eV excitation in 10 K at the late time. The spectra at 2 ps, 5 ps, and 10 ps time delays are shown. The lowest curve shows the pump laser spectrum.

Fig. 17 The change in the absorption coefficient,  $-\Delta\alpha$  as a function of the time delay observed under the 1.99 eV excitation at 10 K. The probe energy of each trace is shown in the figure.

Fig. 18 The change in the absorption coefficient,  $-\Delta\alpha$  as a function of the time delay observed under the 1.99 eV excitation at the late time. The probe energy of each trace is shown in the figure.

Fig. 19 Time-resolved absorption change,  $-\Delta\alpha$  observed under the resonant excitation of the A-exciton at 10 K around the time origin. The vertical scale of each curve is normalized by the respective maximum value. The lowest curve shows the pump laser spectrum.

Fig. 20 Time-resolved absorption change,  $-\Delta\alpha$  observed under the resonant excitation of the A-exciton after the pump. The vertical scale of each curve is normalized by the respective maximum value. The lowest curve shows the pump laser spectrum.

Fig. 21 Time-resolved absorption change,  $-\Delta\alpha$  observed under the resonant excitation of the A-exciton at the late time. The vertical scale of each curve is normalized by the respective maximum value. The lowest curve shows the pump laser spectrum.

Fig. 22 Time-resolved absorption change,  $-\Delta\alpha$  observed under the resonant excitation of the B-exciton before the time origin. The vertical scale of each curve is normalized by the respective maximum value. The lowest curve shows the pump laser spectrum.

Fig. 23 Time-resolved absorption change,  $-\Delta\alpha$  observed under the resonant excitation of the B-exciton around the time origin. The vertical scale of each curve is normalized by the respective maximum value. The lowest curve shows the pump laser spectrum.

Fig. 24 Time-resolved absorption change,  $-\Delta\alpha$  observed under the resonant excitation of the B-exciton after the pump. The vertical scale of each curve is normalized by the respective maximum value. The lowest curve shows the pump laser spectrum.

Fig. 25 Time-resolved absorption change,  $-\Delta\alpha$  observed under the resonant excitation of the B-exciton at the long time delay. The vertical scale of each curve is normalized by the respective maximum value. The lowest curve shows the pump laser spectrum.

Fig. 26 Plots of the absorption change,  $-\Delta\alpha$  as a function of the time delay around the time origin. The probe energy  $E_{pr}$  is 1.91 eV. A solid line shows the data taken under the B-exciton

resonant excitation and a dashed line shows the data taken under the A-exciton resonant excitation.

Fig. 27 Plots of the absorption change,  $-\Delta\alpha$  as a function of the time delay around the time origin. The probe energy  $E_{pr}$  is 1.86 eV. A solid line shows the data taken under the B-exciton resonant excitation and a dashed line shows the data taken under the A-exciton resonant excitation.

Fig. 28 Plots of the absorption change,  $-\Delta\alpha$  as a function of the time delay around the time origin. The probe energy  $E_{pr}$  is 1.84 eV. A solid line shows the data taken under the B-exciton resonant excitation and a dashed line shows the data taken under the A-exciton resonant excitation.

Fig. 29 Plots of the absorption change,  $-\Delta\alpha$  as a function of the time delay around the time origin. The probe energy  $E_{pr}$  is 1.82 eV. A solid line shows the data taken under the B-exciton resonant excitation and the dashed line shows the data taken under the A-exciton resonant excitation.

Fig. 30 Plots of the absorption change,  $-\Delta\alpha$  as a function of the time delay around the time origin. The probe energy  $E_{pr}$  is 1.81 eV. A solid line shows the data taken under the B-exciton resonant excitation and a dashed line shows the data taken under the A-exciton resonant excitation.

Fig. 31 Plots of the absorption change,  $-\Delta\alpha$  as a function of the time delay at the long time delay. The probe energies  $E_{pr}$  are shown in the figure. The solid lines show the data taken under the B-exciton resonant excitation and the dashed lines shows the data taken under the A-exciton resonant excitation. The horizontal short bars represent the respective zero point.

Fig. 32 The change in the absorption coefficient,  $-\Delta\alpha$  observed under the resonant excitation of the A-exciton at 10 K. The excitation density of each spectrum is shown in the figure. The time delay is 0 fs.

Fig. 33 The change in the absorption coefficient,  $-\Delta\alpha$  observed under the resonant excitation of the A-exciton at 10 K. The excitation density of each spectrum is shown the figure. The time delay is 150 fs.

Fig. 34 Temporal changes in the spectrally integrated value of the bleaching,  $\Delta S_B$  ( solid lines ) and that of the induced absorption,  $\Delta S_A$  observed under the 1.99 eV excitation at the short time delay. The left part shows the data in the linear scale, and the right part in the logarithmic scale.

Fig. 35 Temporal change in the spectrally integrated value of the bleaching,  $\Delta S_B$  ( solid lines ) and that of the induced absorption,  $\Delta S_A$  observed under the 1.99 eV excitation at the long time delay. The left part shows the data in the linear scale, and the right part in the logarithmic scale.

Fig. 36 Temporal change in the spectrally integrated value of the bleaching,  $\Delta S_B$  ( solid lines ) and that of the induced absorption,  $\Delta S_A$  observed under the B-exciton resonant excitation at the short time delay. The left part shows the data in the linear scale, and the right part in the logarithmic scale.

Fig. 37 Temporal change in the spectrally integrated value of the bleaching,  $\Delta S_B$  ( solid lines ) and that of the induced absorption,  $\Delta S_A$  observed under the B-exciton resonant excitation at the long time delay. The left part shows the data in the linear scale, and the right part in the logarithmic scale.

Fig. 38 Temporal change in the spectrally integrated value of the bleaching,  $\Delta S_B$  ( solid lines ) and that of the induced absorption,  $\Delta S_A$  observed under the A-exciton resonant excitation at the short time delay. The left part shows the data in the linear scale, and the right part in the logarithmic scale.

Fig. 39 Temporal change in the spectrally integrated value of the bleaching,  $\Delta S_B$  ( solid lines ) and that of the induced absorption,  $\Delta S_A$  observed under the A-exciton resonant excitation at the long time delay. The left part shows the data in the linear scale, and the right part in the logarithmic scale.

Fig. 40 A calculated absorption spectrum based on the generalized Elliot formula. The detail of the calculation is described in the appendix. The solid line shows the result for the low

carrier density (  $\sim 10^{14} \text{ cm}^{-3}$  ) and the dashed line shows the result for the high carrier density (  $\sim 10^{17} \text{ cm}^{-3}$  ).

Fig. 41 Calculated absorption spectra of the interband transition in direct-gap semiconductors. A solid line shows the isotropic case, and a dashed line the anisotropic case.

Fig. 42 The electron and hole distribution functions simulated by means of the Monte-Carlo method. The dashed lines show the electron distribution function, and the dotted lines show the hole distribution function. The solid lines show the sum of both the distribution functions. The bottom curve shows the initial distribution.

Fig. 43 The electron and hole distribution functions simulated by means of the Monte-Carlo method. The dashed lines show the electron distribution function, and the dotted lines show the hole distribution function. The solid lines show the sum of both the distribution functions.

Fig. 44 Temporal change of the effective temperature of hot carriers  $T_c$  at 4.2 K. Solid circles show experimentally estimated temperature. A solid line is the best fitted result based on eq. (4.2.2) in the text. Here, the vertical scale of  $T_c$  is replaced by  $T_h = (\mu/m_h) T_c$ , corresponding to the case that hot carriers are hot A-holes. Then, initial temperature of  $T_h$  is 220 K and the phonon emission time  $\tau_h$  is 1.5 ps.

Fig. 45 Temporal change of the effective temperature of hot carriers  $T_c$  at the room temperature. Solid circles show experimentally estimated temperature. A solid line is the best fitted result based on eq. (4.2.2) in the text. Here, the vertical scale of  $T_c$  is replaced by  $T_h = (\mu/m_h)T_c$ , corresponding to the case that hot carriers are hot A-holes. Then, initial temperature of  $T_h$  is 200 K and the phonon emission time  $\tau_h$  is 2.0 ps.

Fig. 46 The relaxation time constants of the bleaching as a function of the photon energy observed under the 2.12 eV excitation at 4.2 K (solid line) and the room temperature (dashed line) in the logarithmic scale.

Fig. 47 The change in the absorption induced by the rigid energy shift of the unperturbed absorption spectrum,  $\alpha_d(E) - \alpha_d(E - \delta E)$ . The rigid energy shift  $\delta E$  is taken to be 4 meV in this figure.

Fig. 48 Excitation density dependence of the spectrally integrated bleaching,  $\Delta S_B$  (solid circles) and the spectrally integrated induced absorption,  $\Delta S_A$  (solid squares) observed under the resonant excitation of the A-exciton at 0 fs.

Fig. 49 Excitation density dependence of the spectrally integrated bleaching,  $\Delta S_B$  (solid circles) and the spectrally integrated induced absorption,  $\Delta S_A$  (solid squares) observed under the resonant excitation of the A-exciton at 150 fs.

Fig. 50 Fitting of the line broadening. The solid line shows the experimental spectrum observed under the A-exciton resonant excitation at 560 fs. The dashed line shows the calculated spectrum based on the broadening of two Lorentzians.

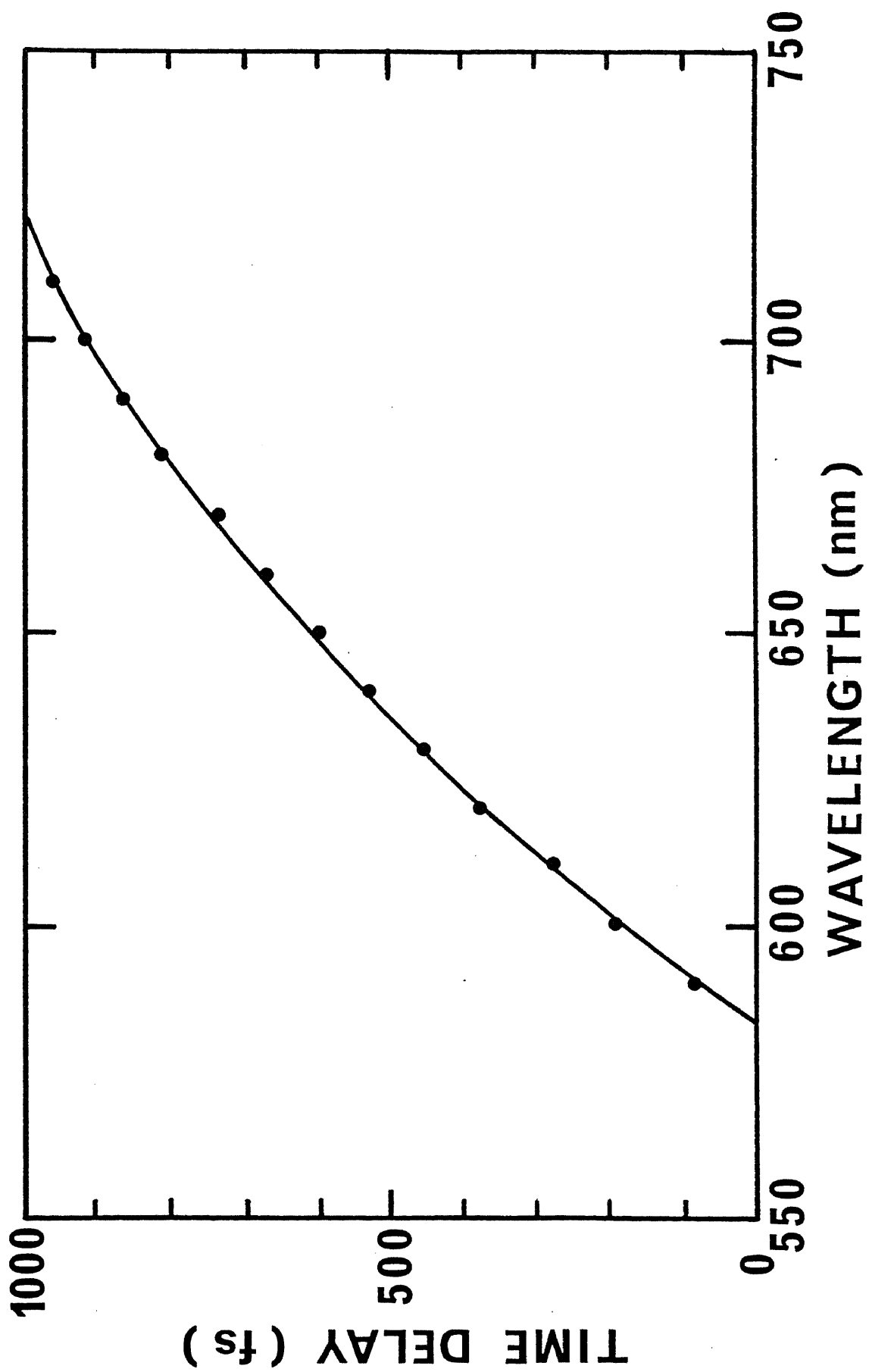


Fig. 1

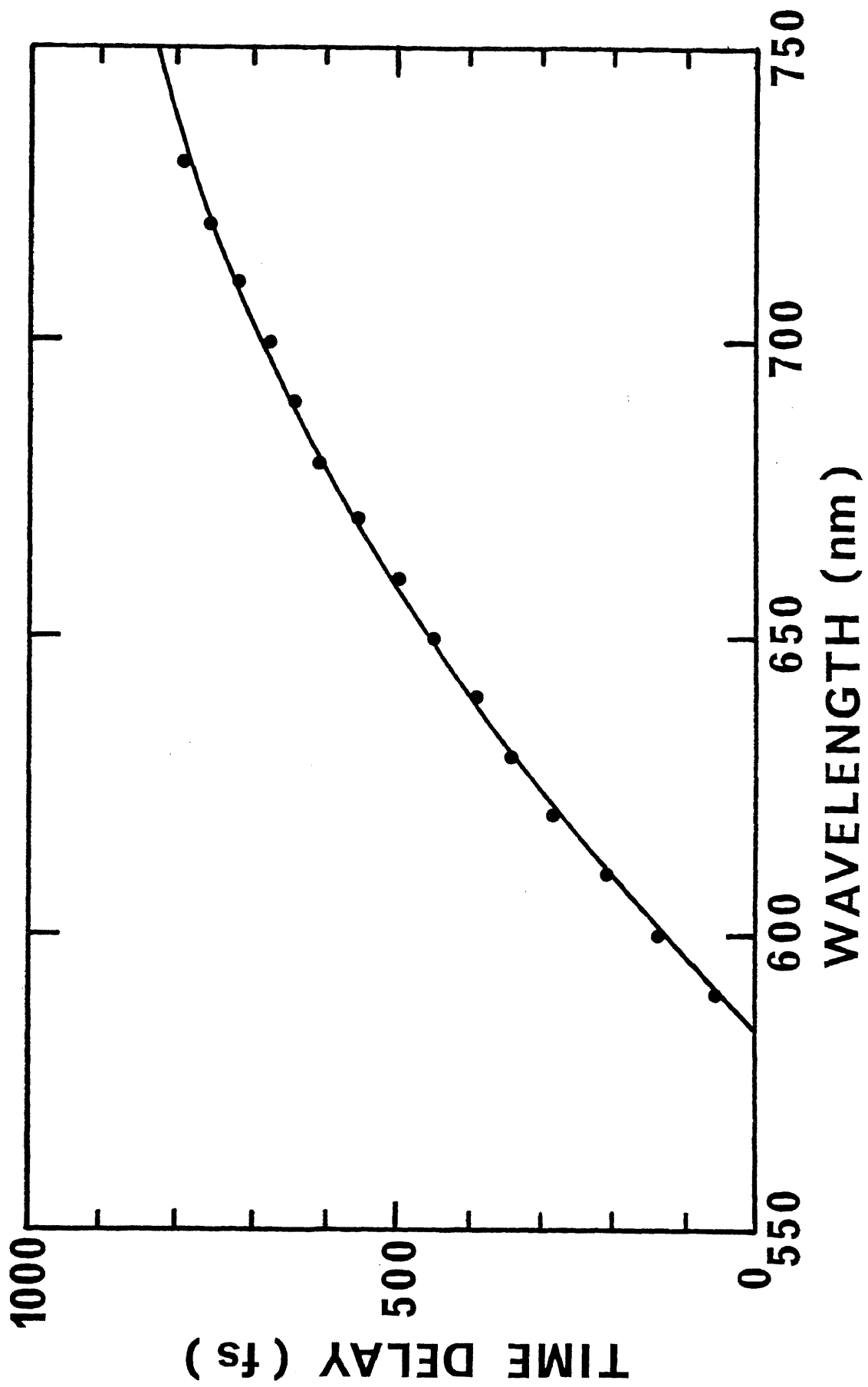


Fig. 2

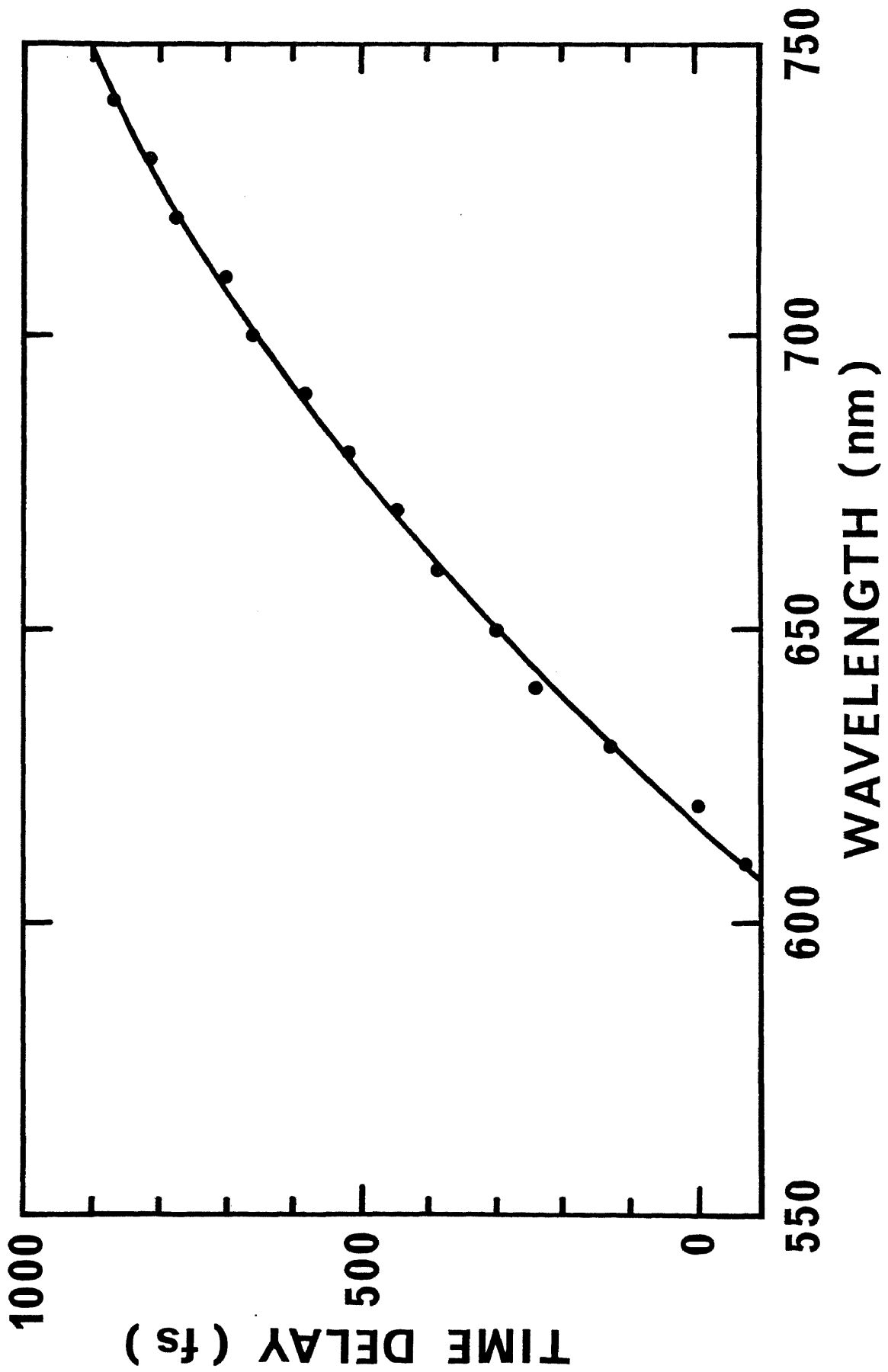


Fig. 3

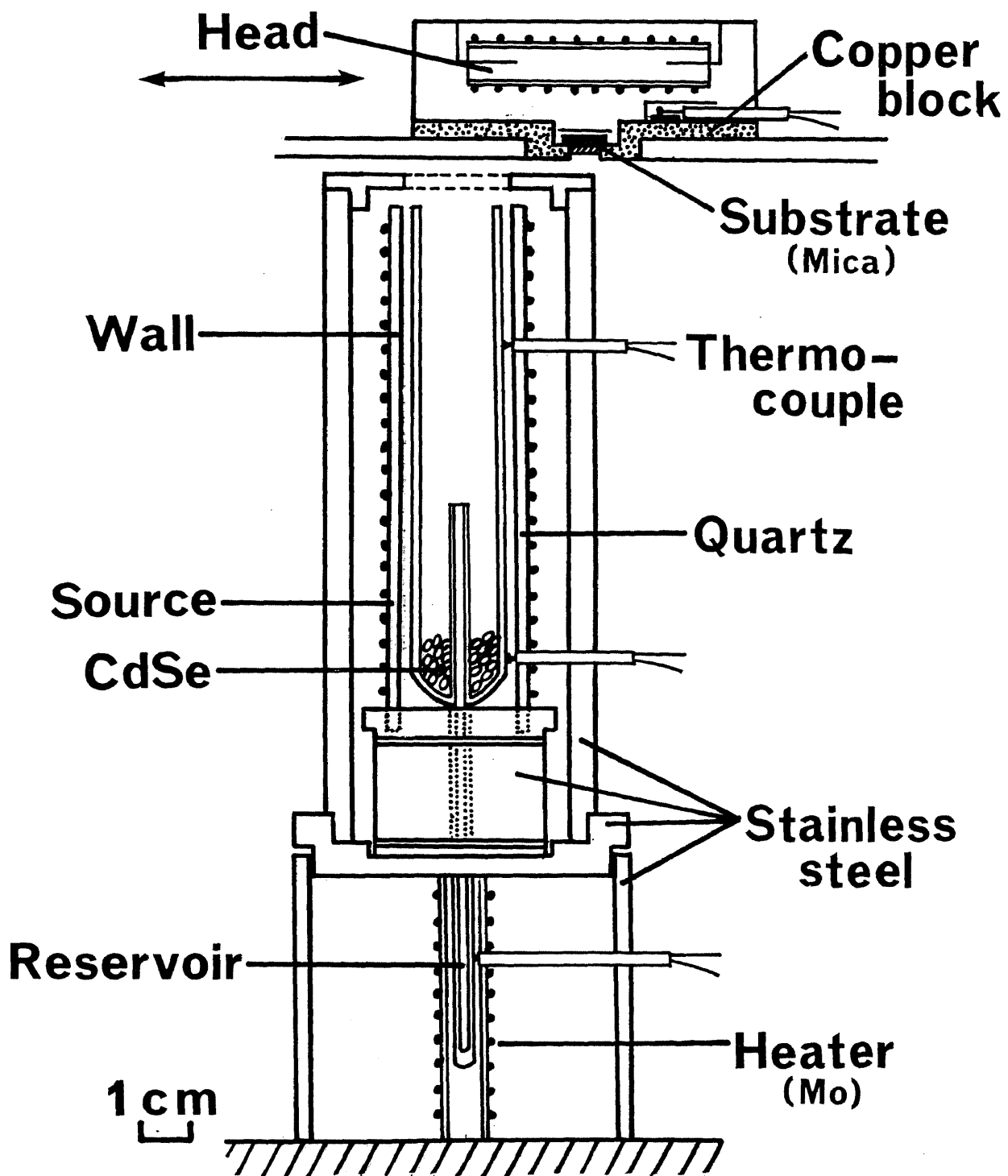


Fig. 4

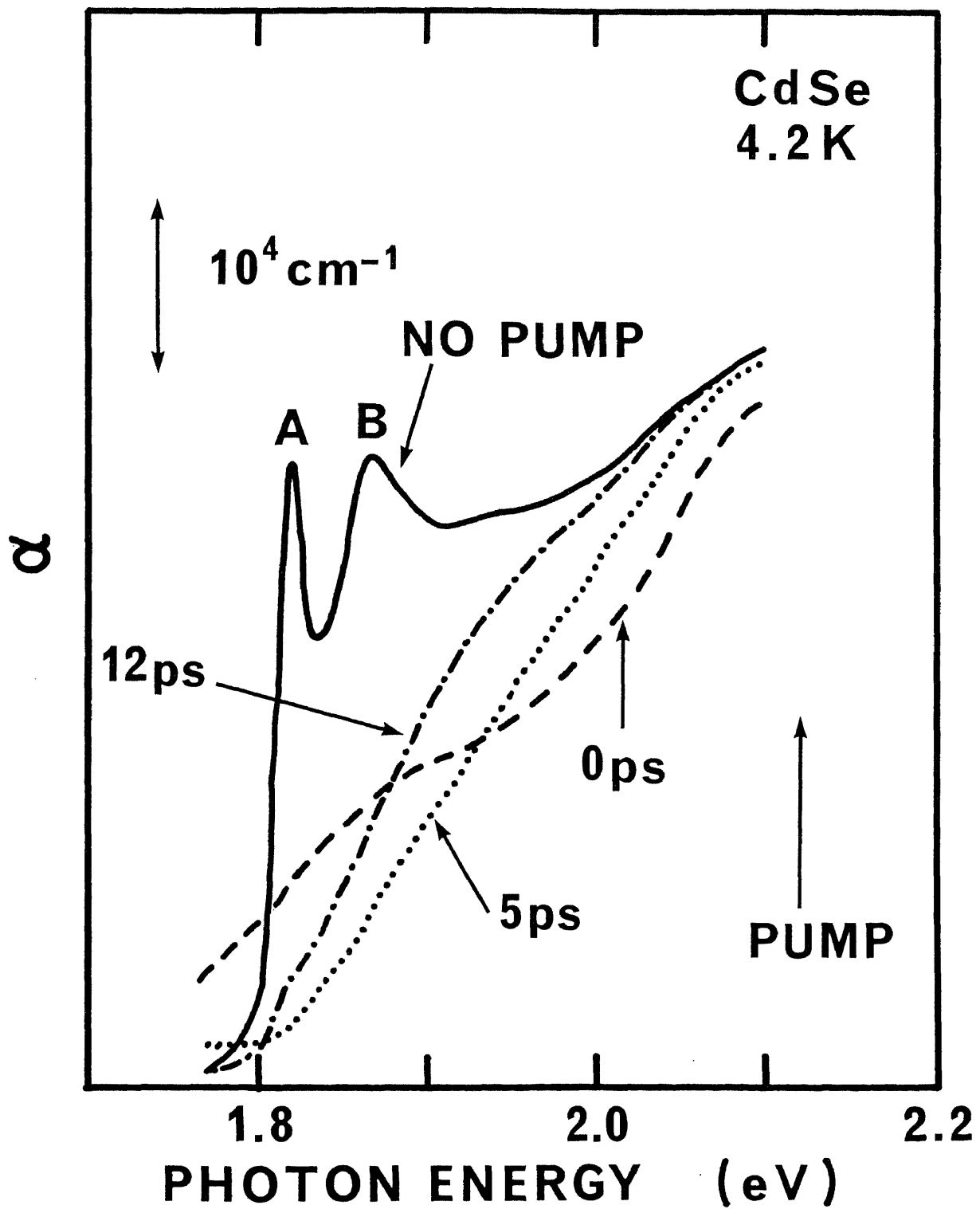


Fig. 5

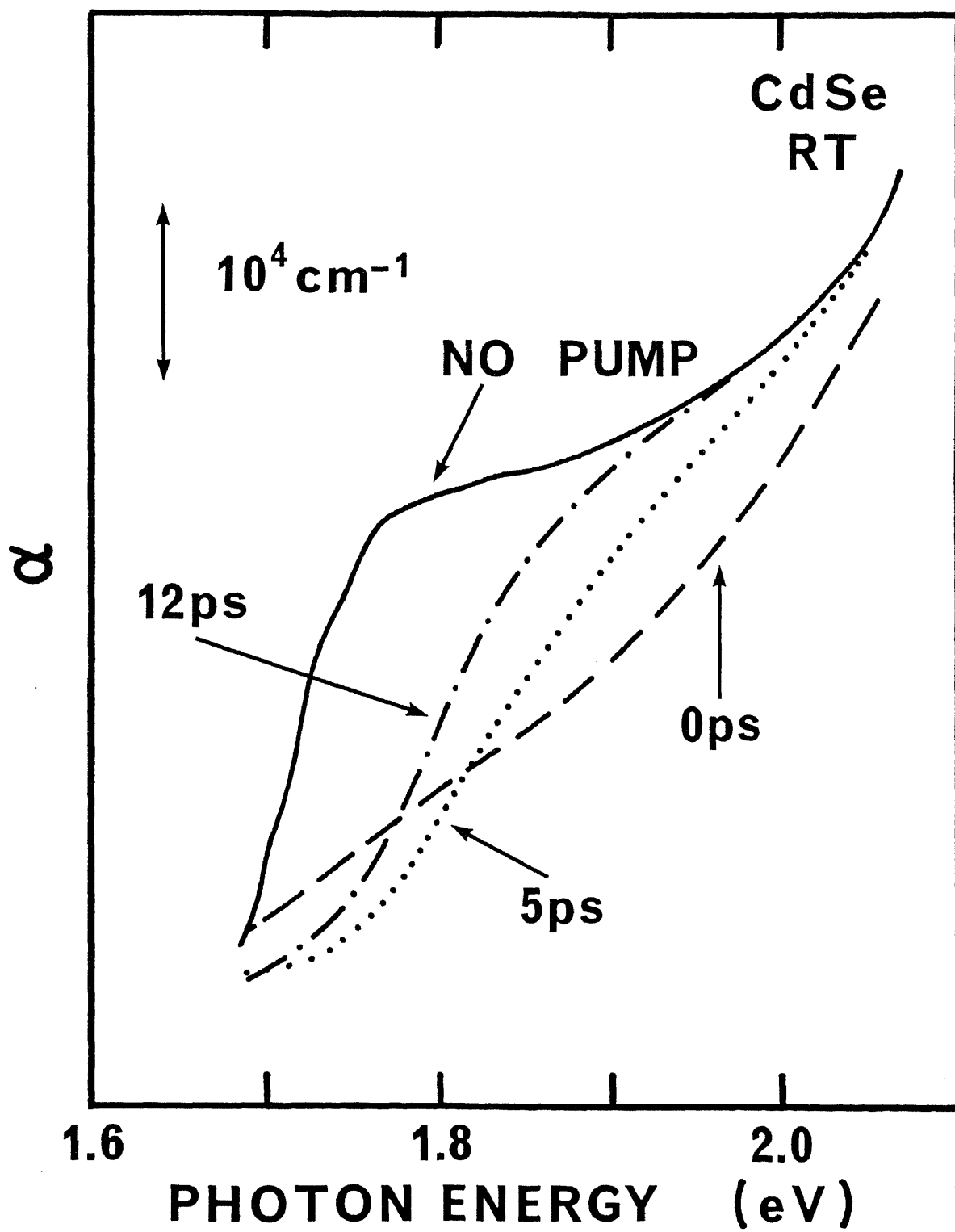


Fig. 6

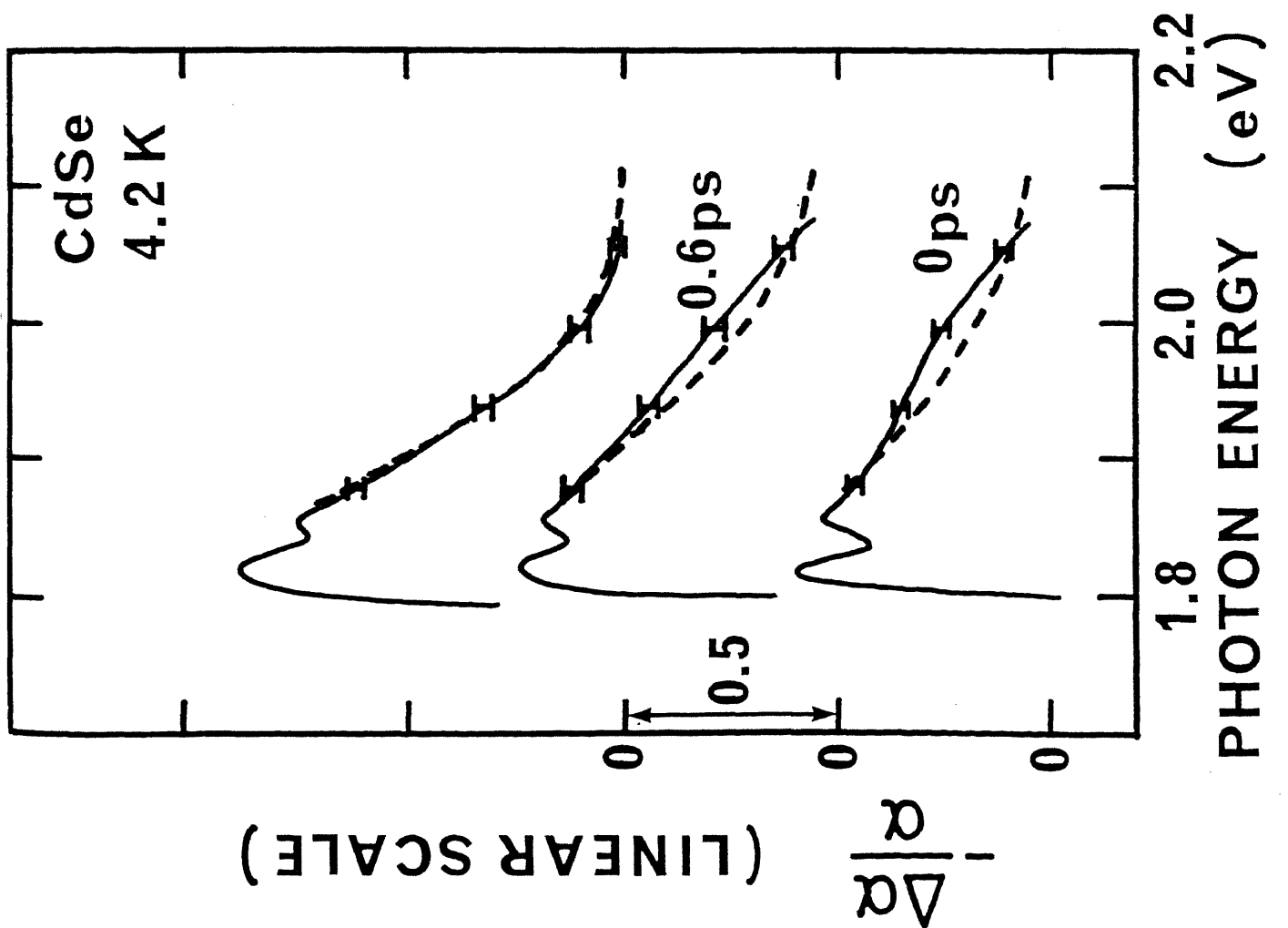
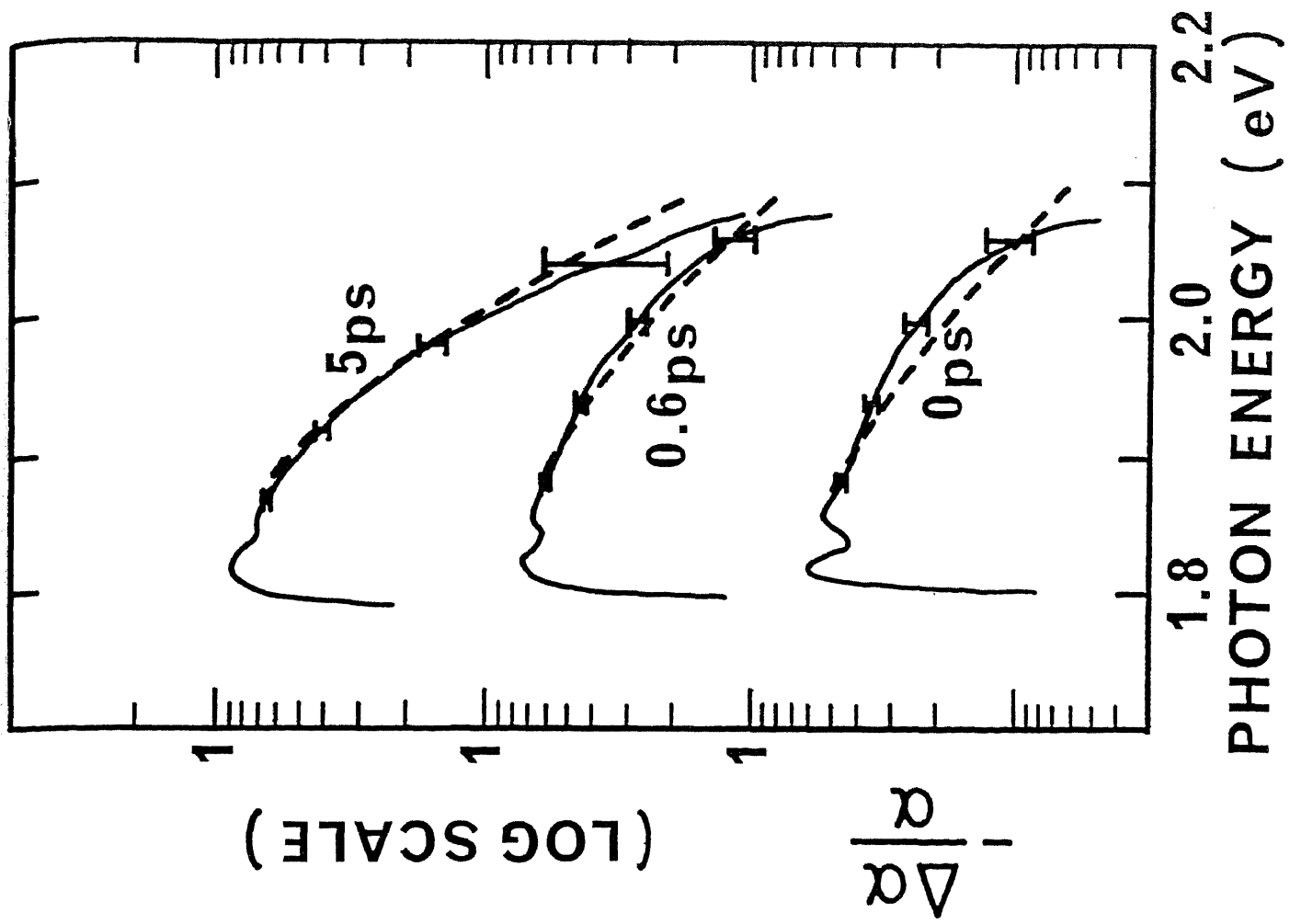
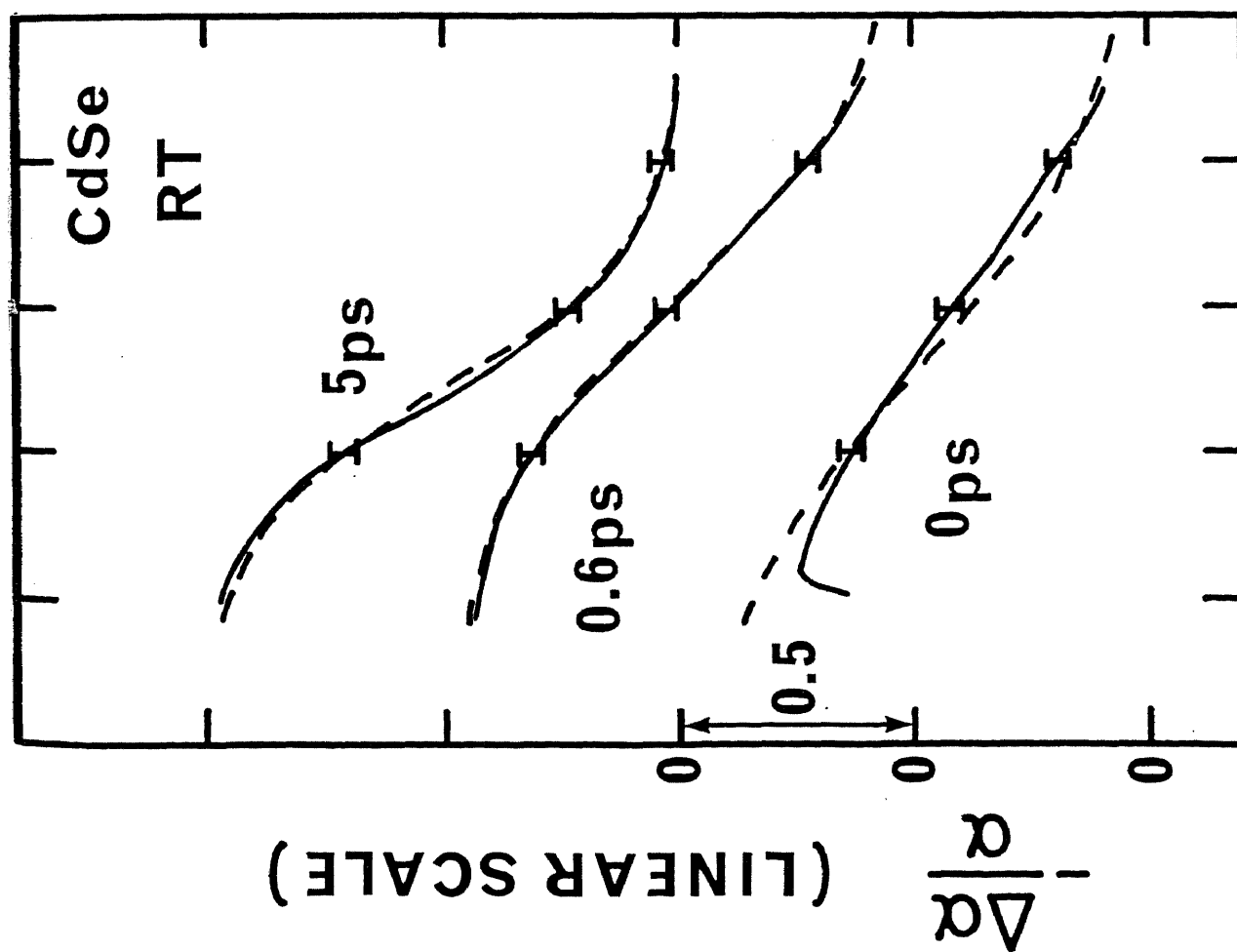
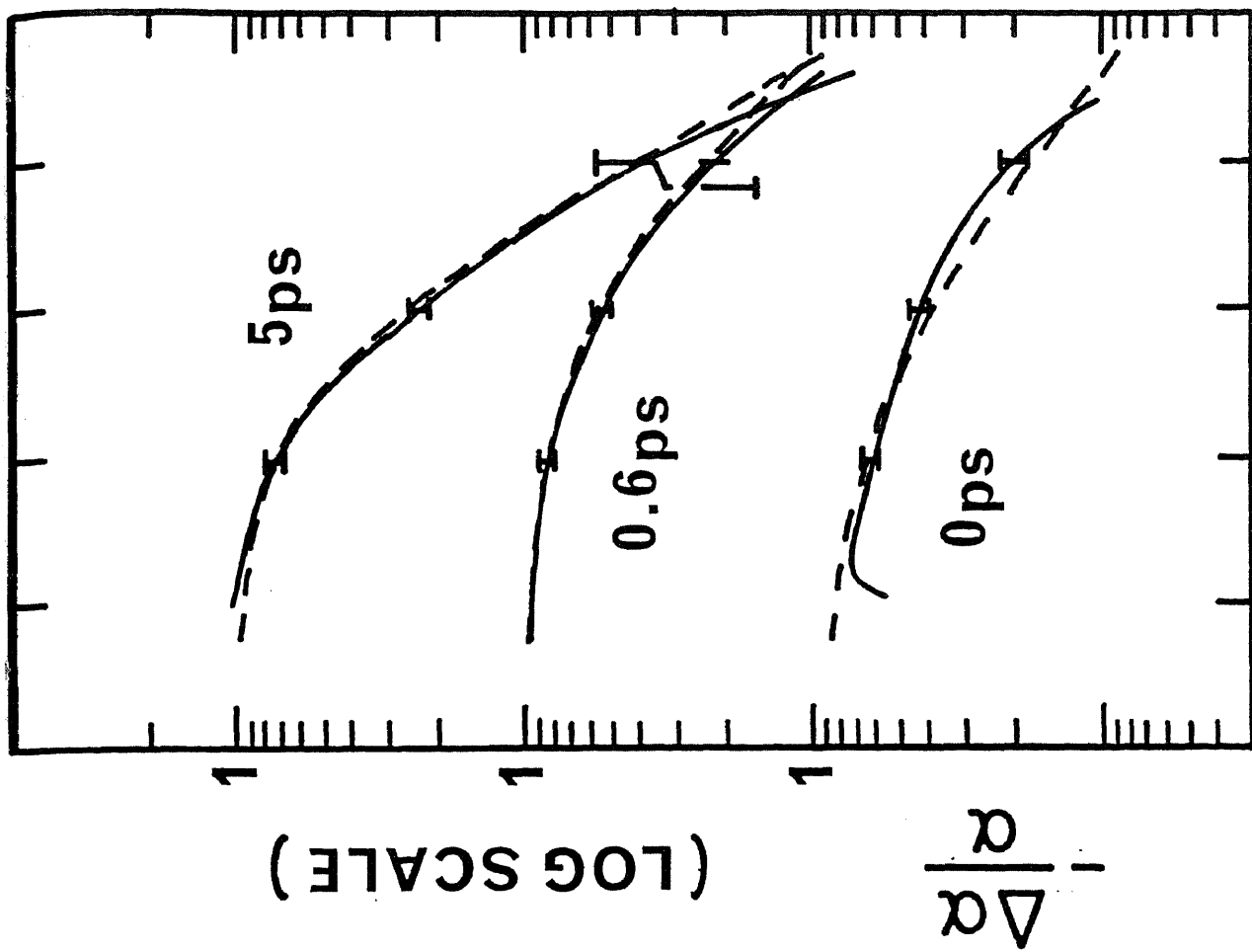


Fig. 7



PHOTON ENERGY (eV)

PHOTON ENERGY (eV)

Fig. 8

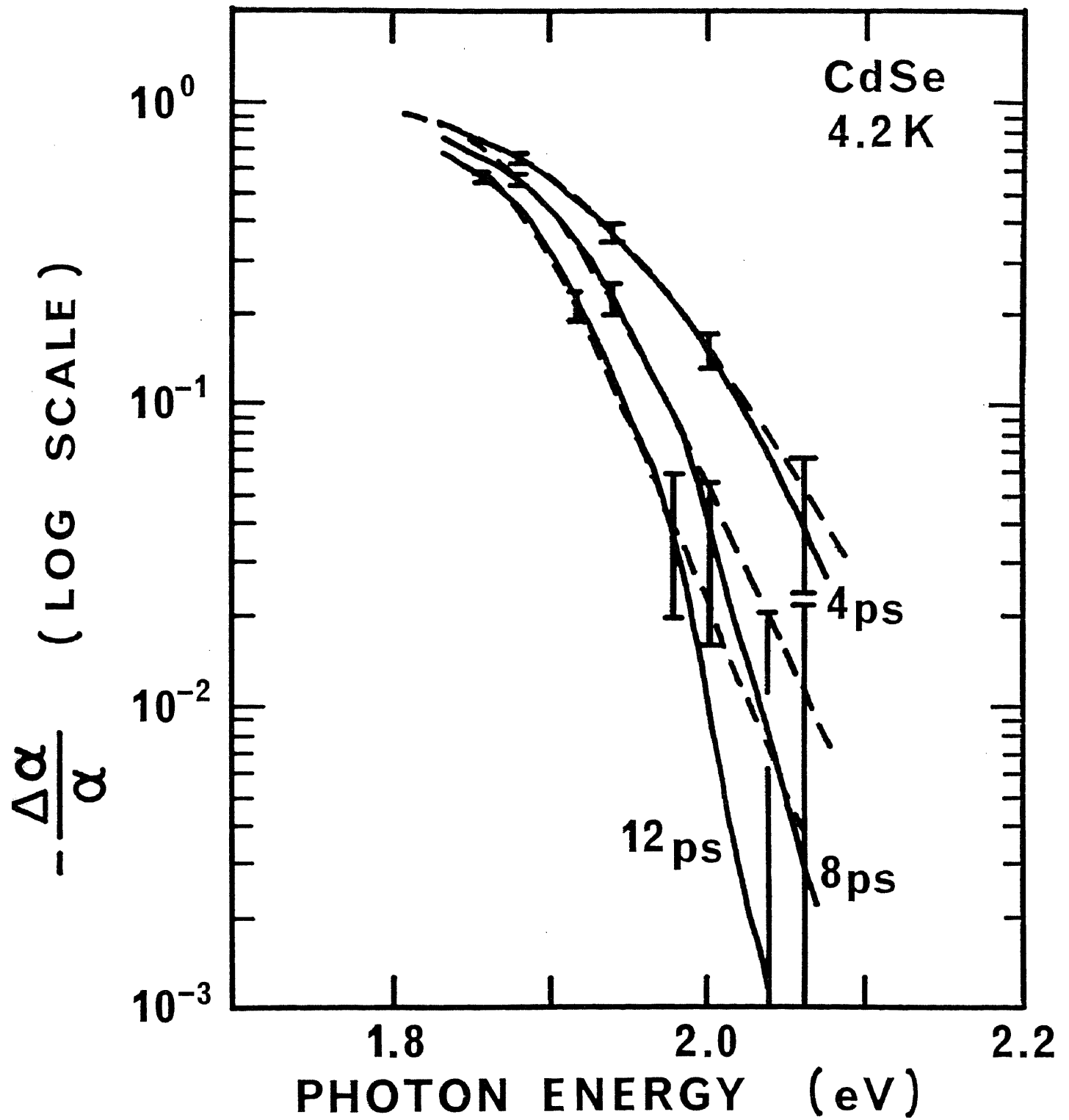


Fig. 9

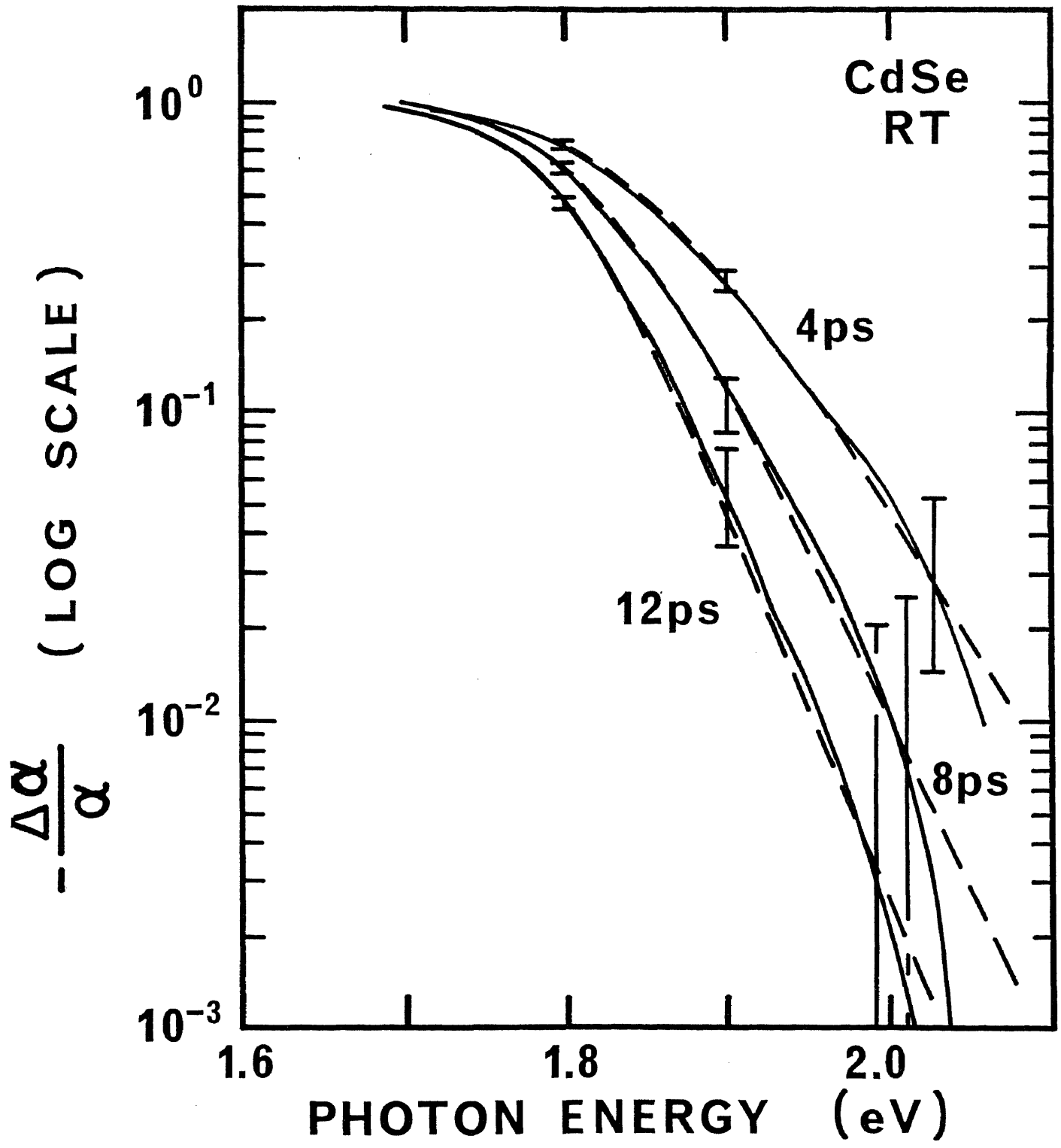


Fig. 10

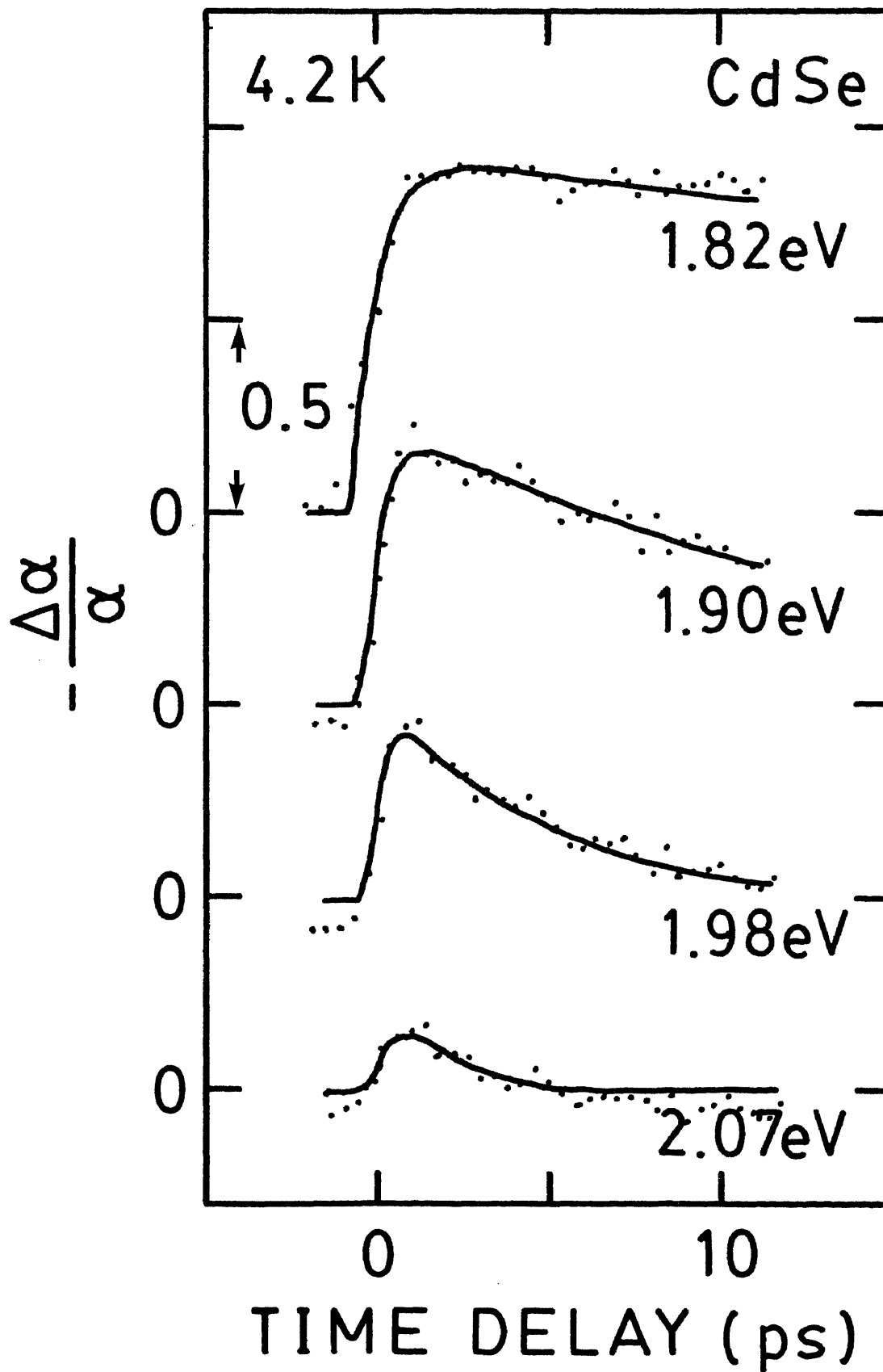


Fig. 11



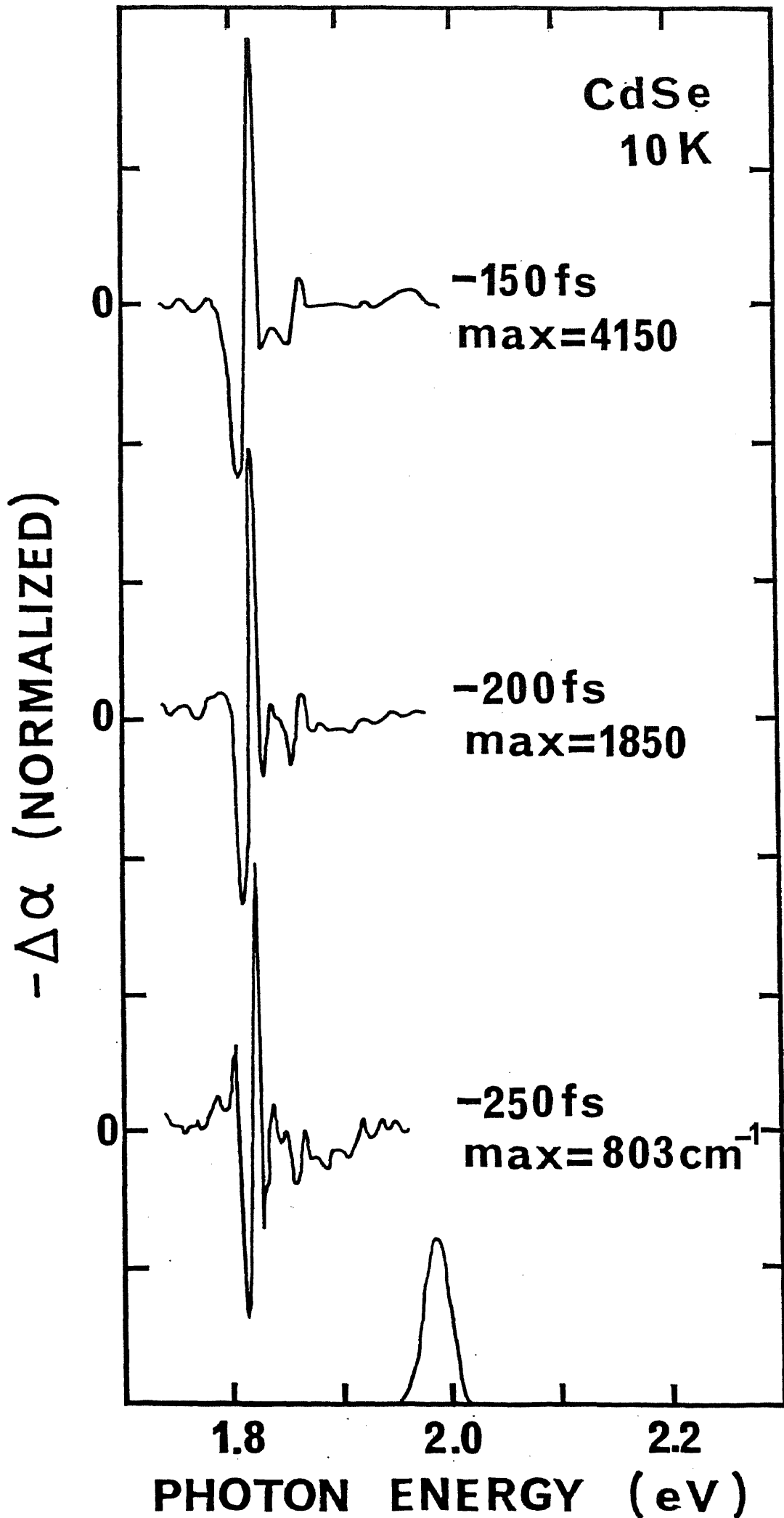


Fig. 13

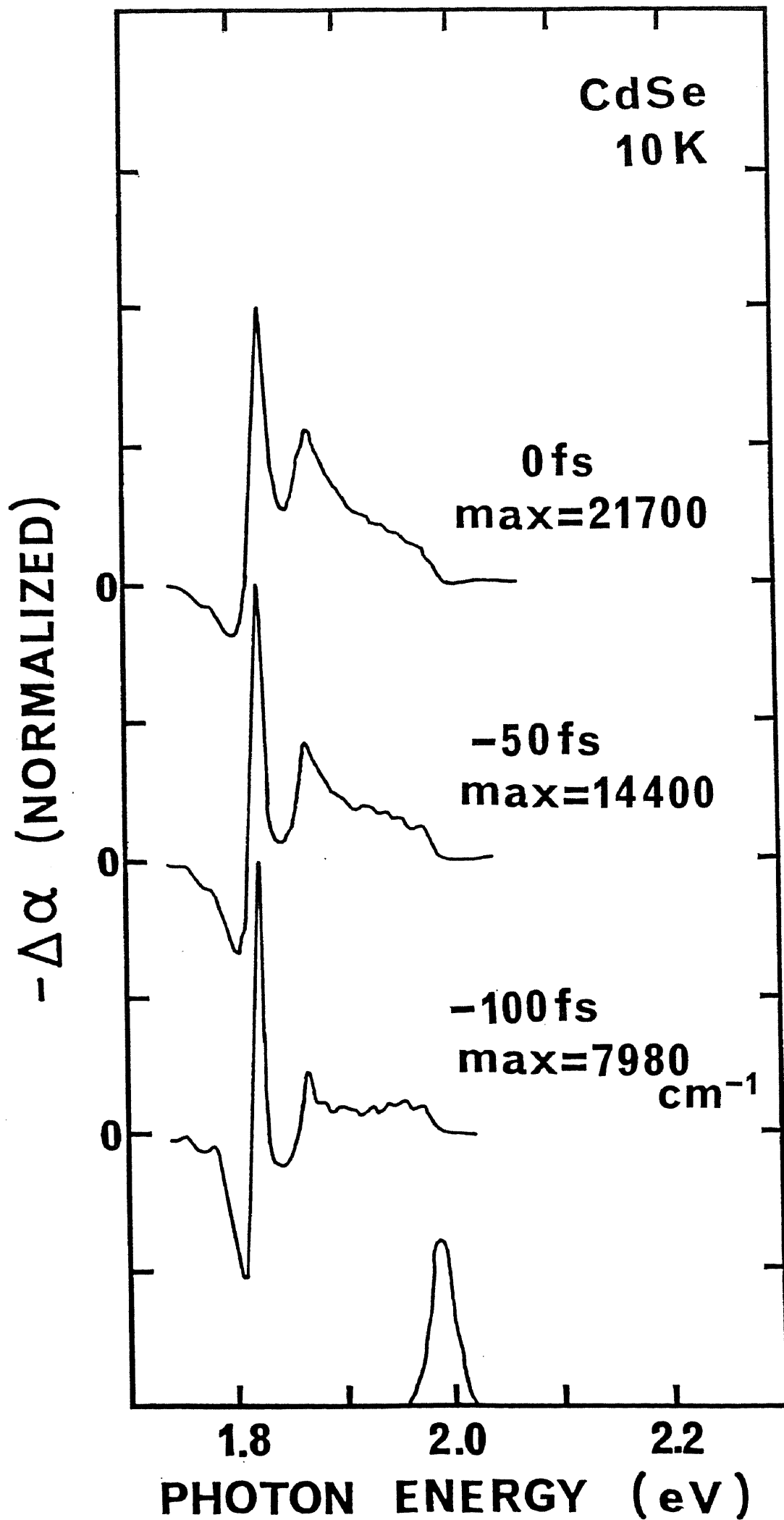


Fig. 14

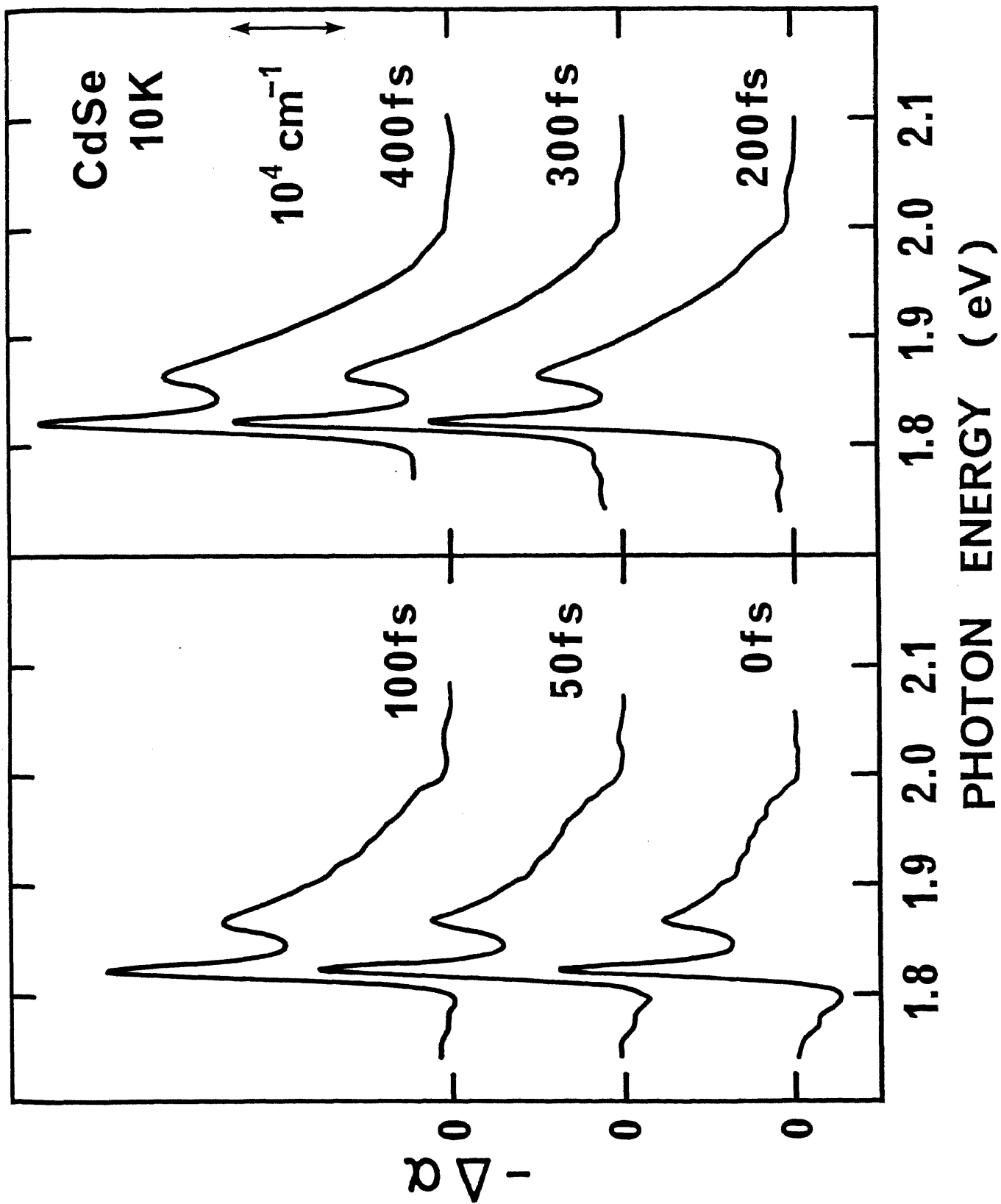


Fig. 15

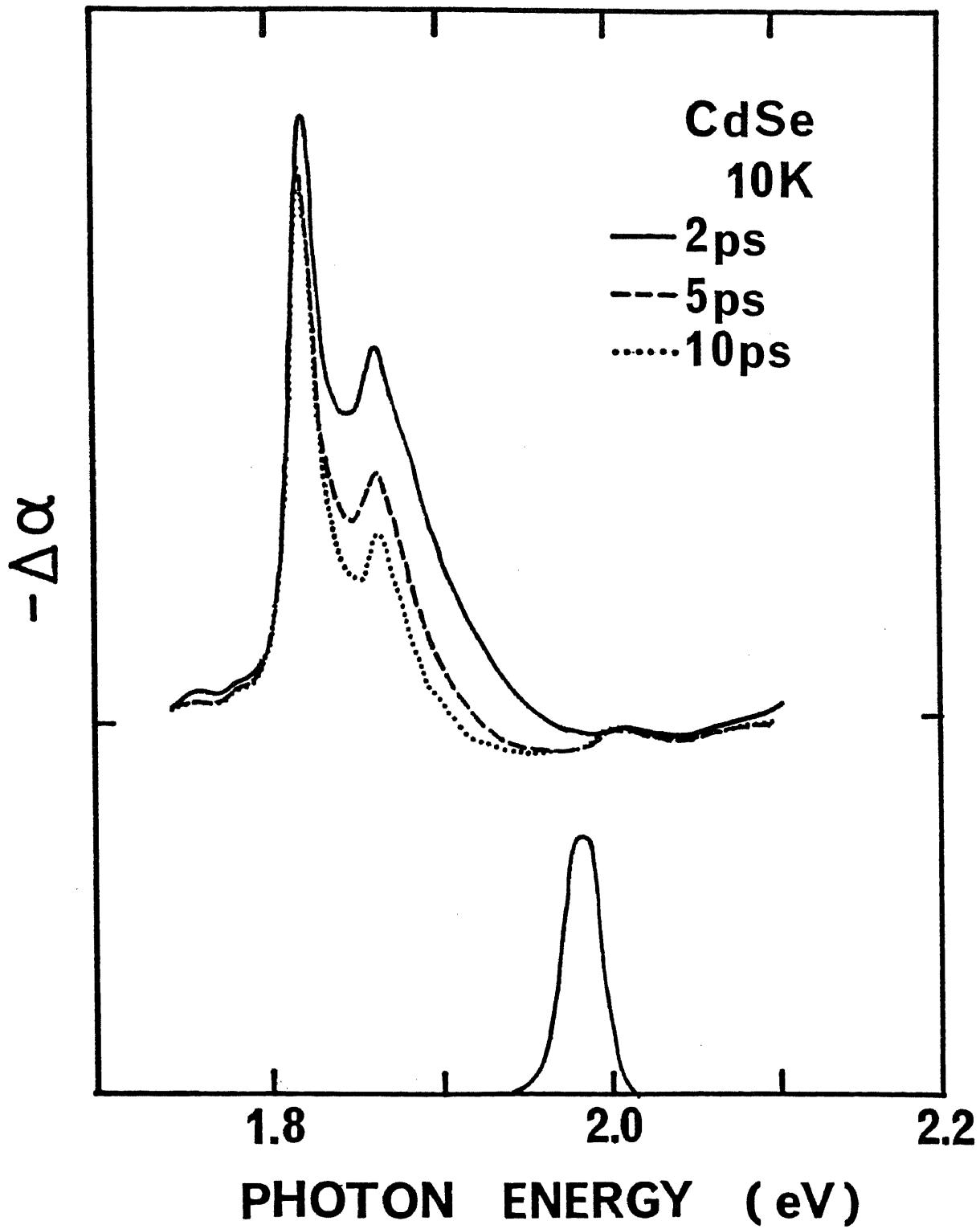


Fig. 16

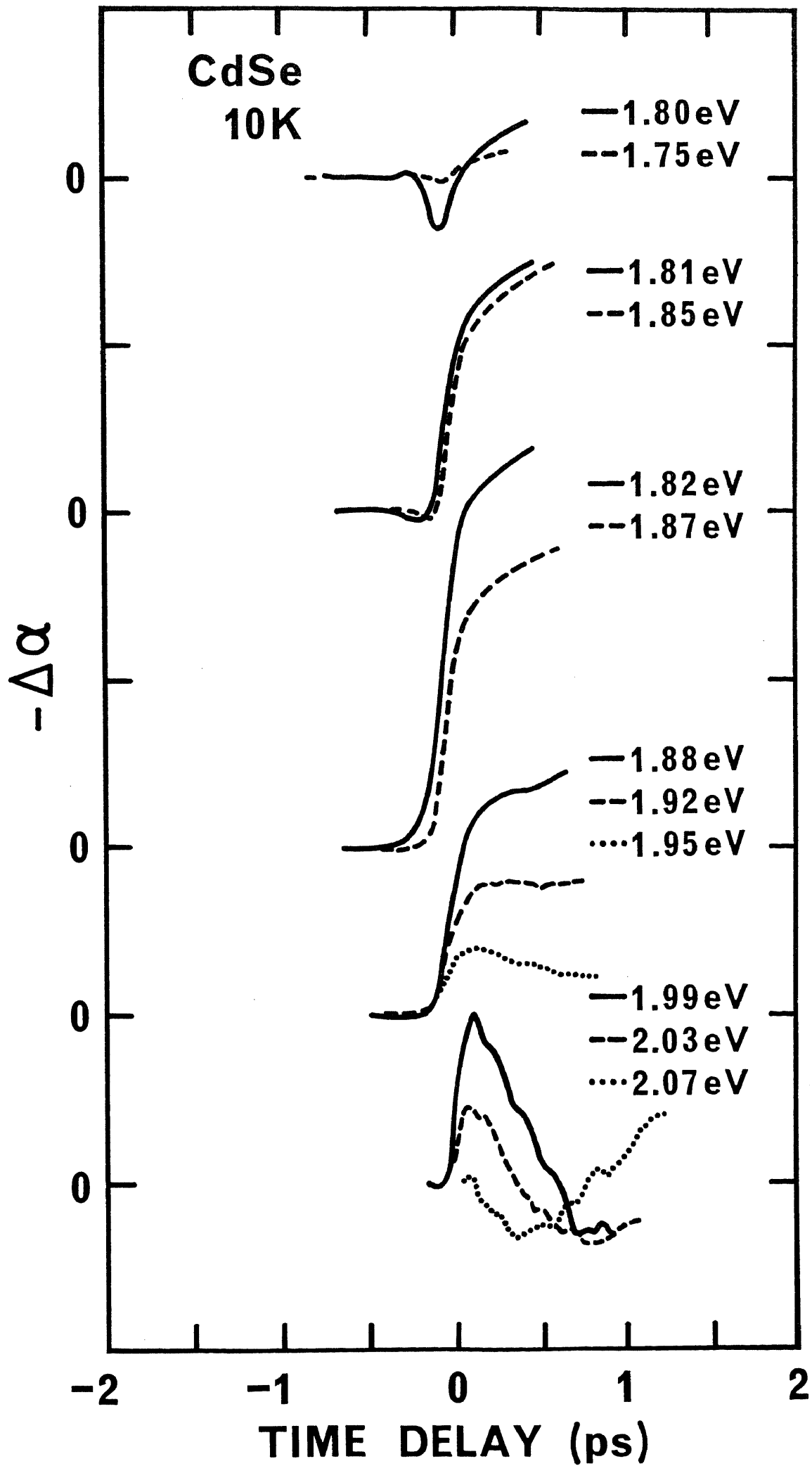


Fig. 17

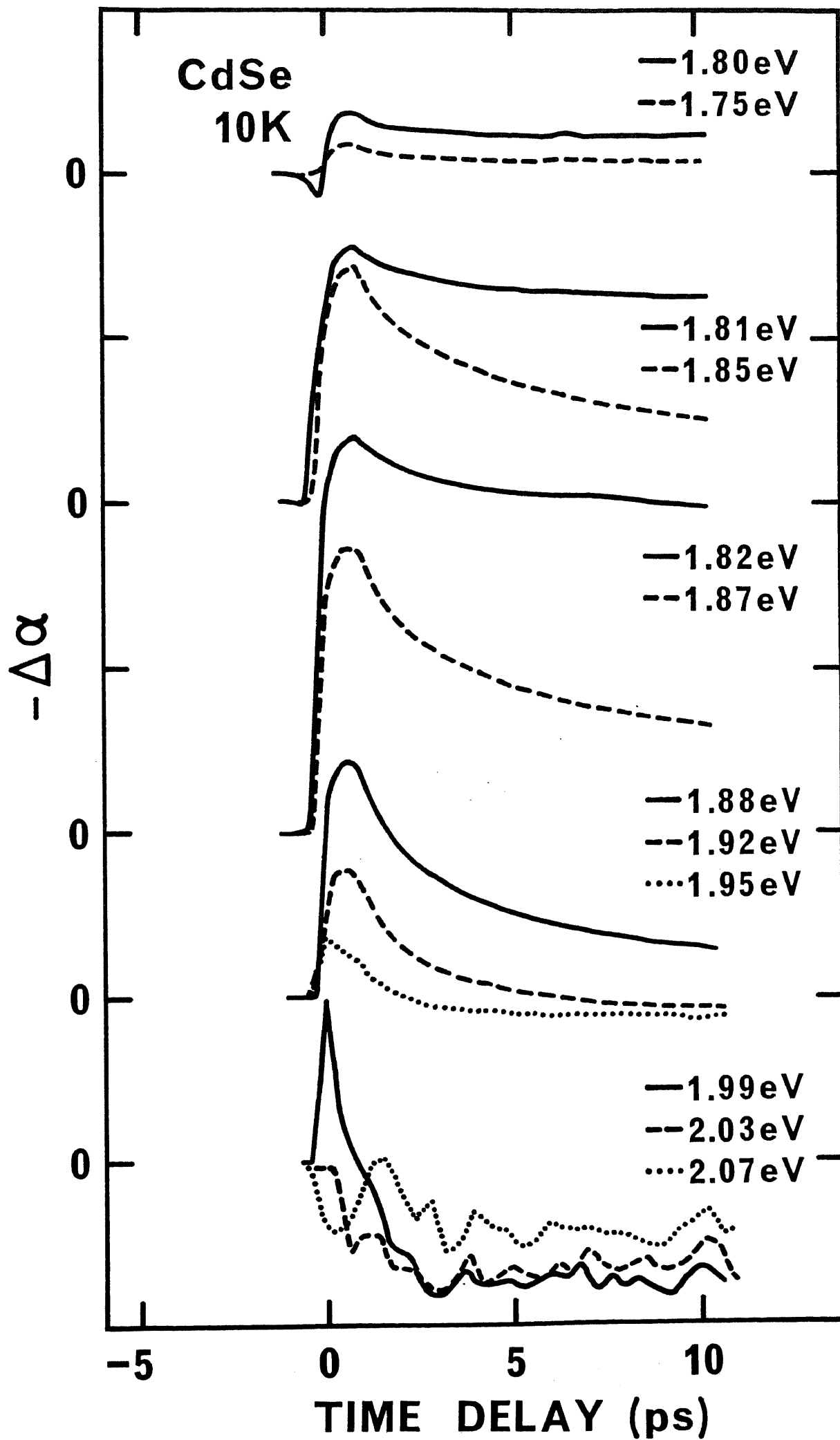


Fig. 18

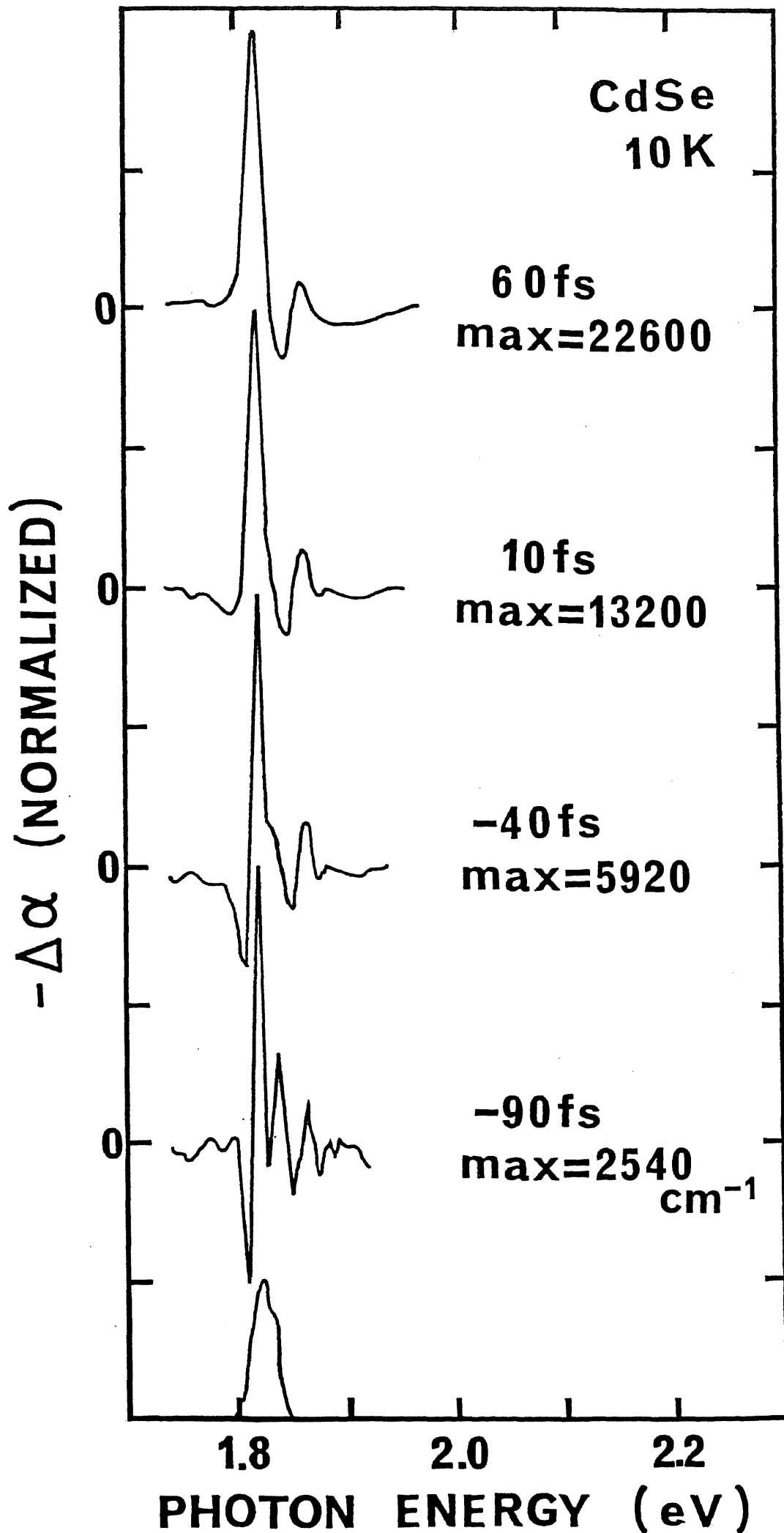


Fig. 19

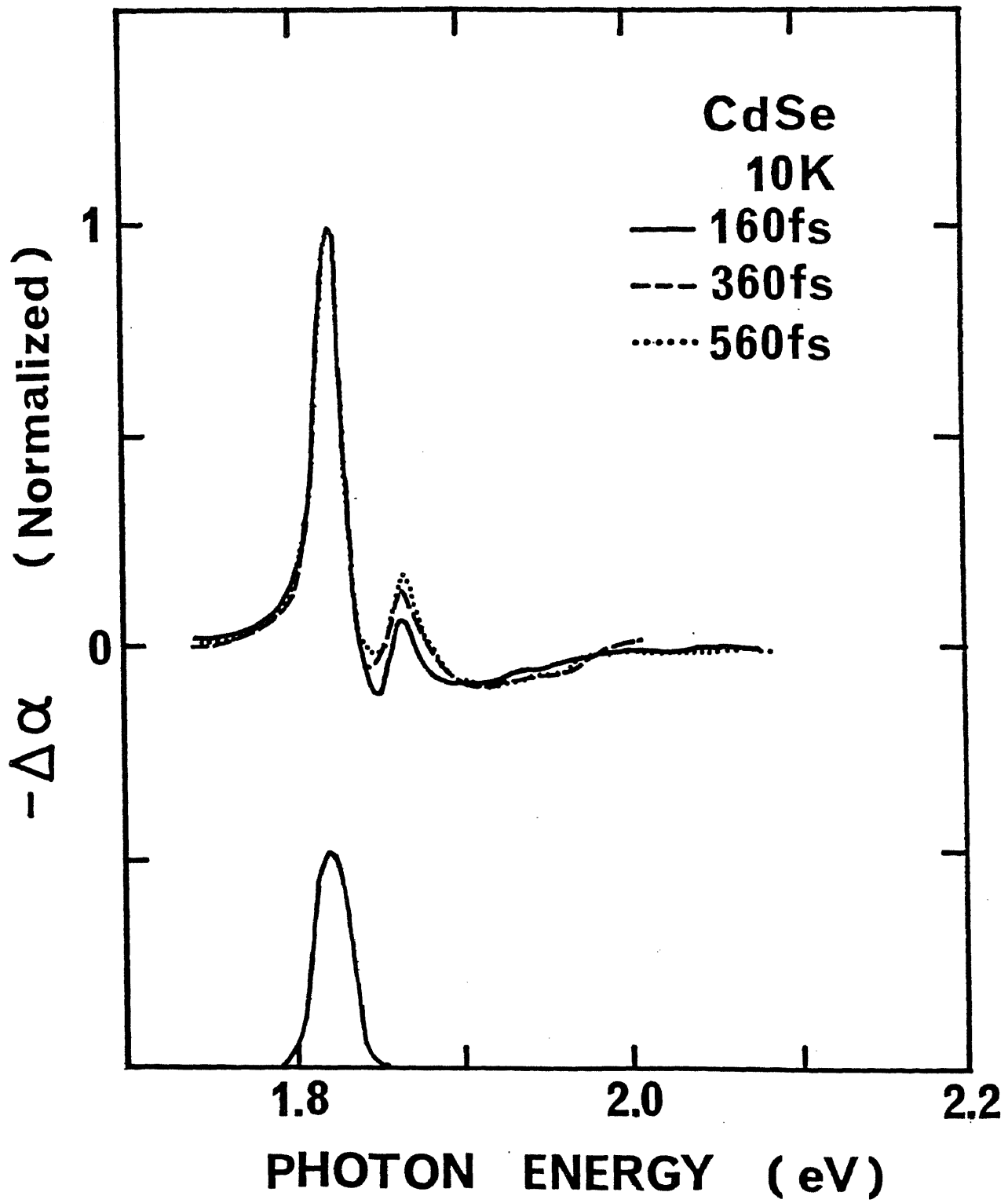


Fig. 20

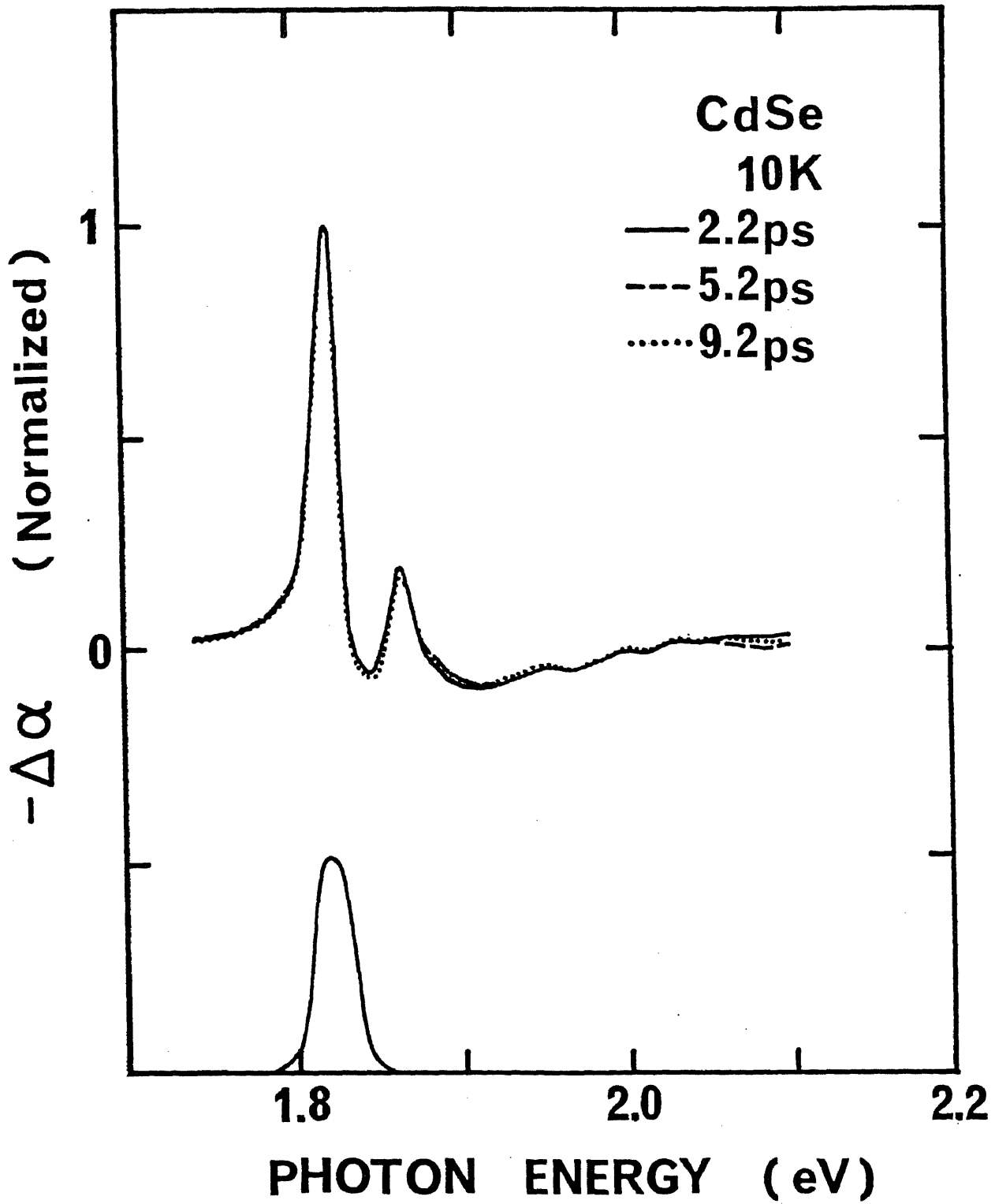


Fig. 21

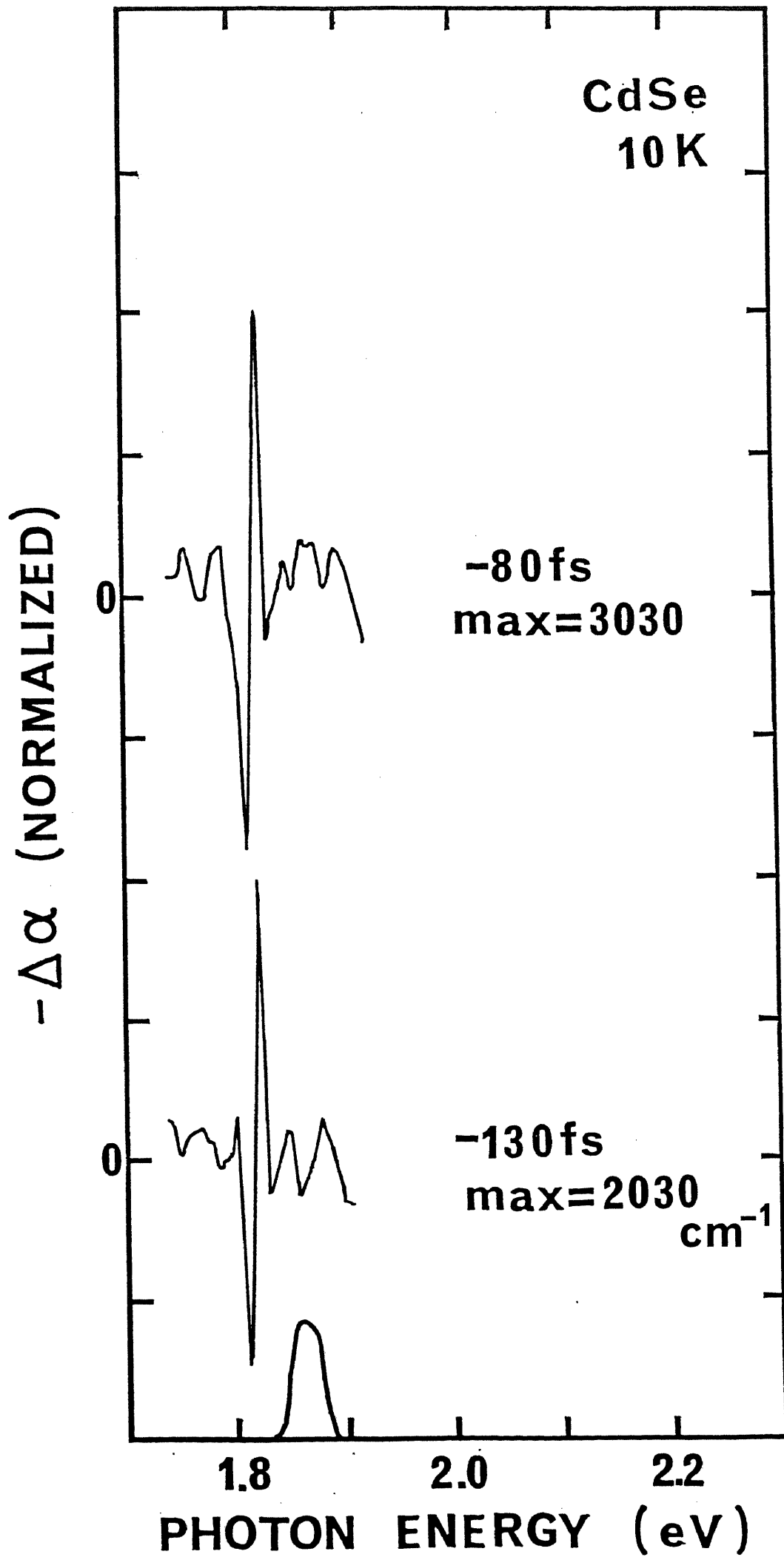


Fig. 22

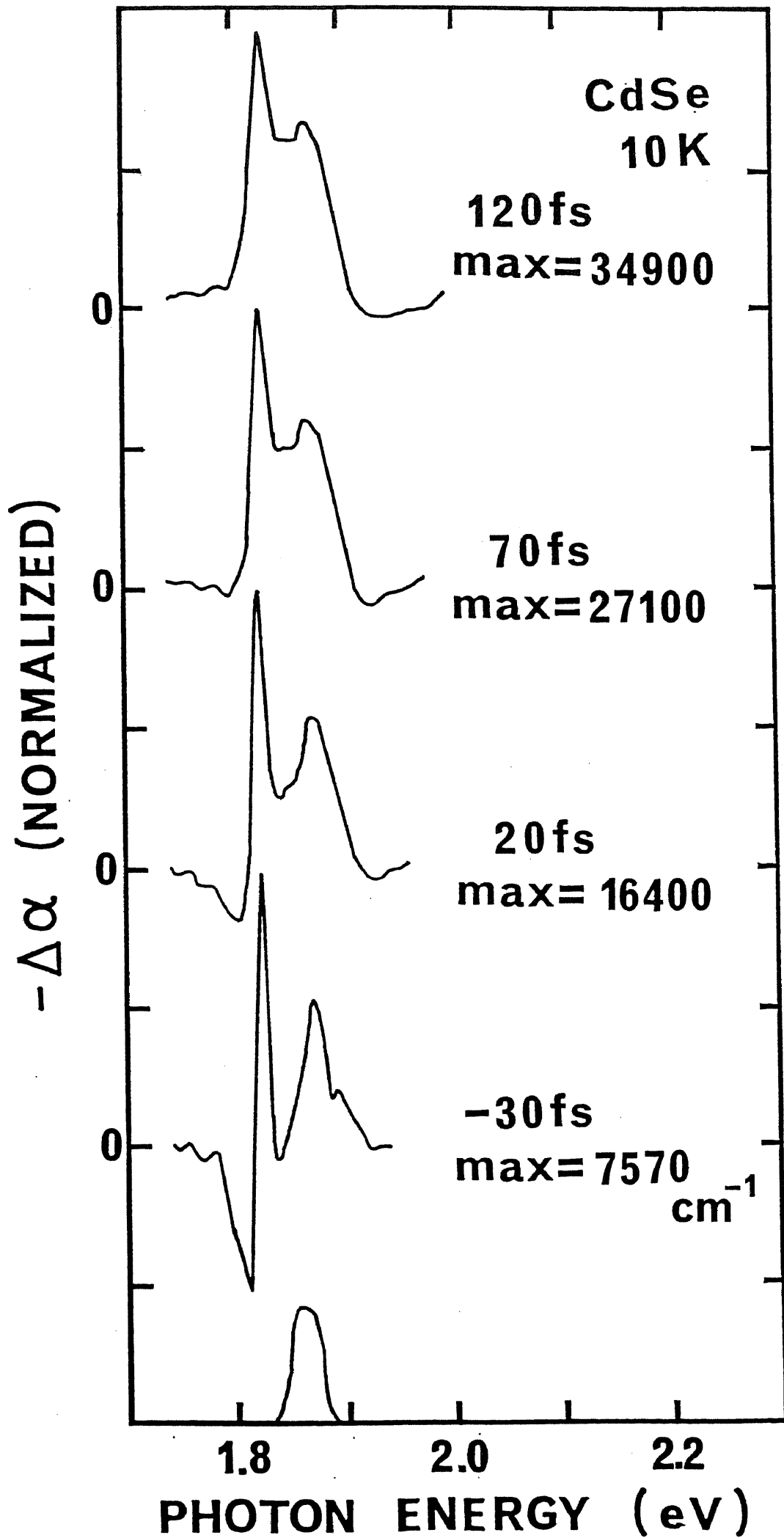


Fig. 23

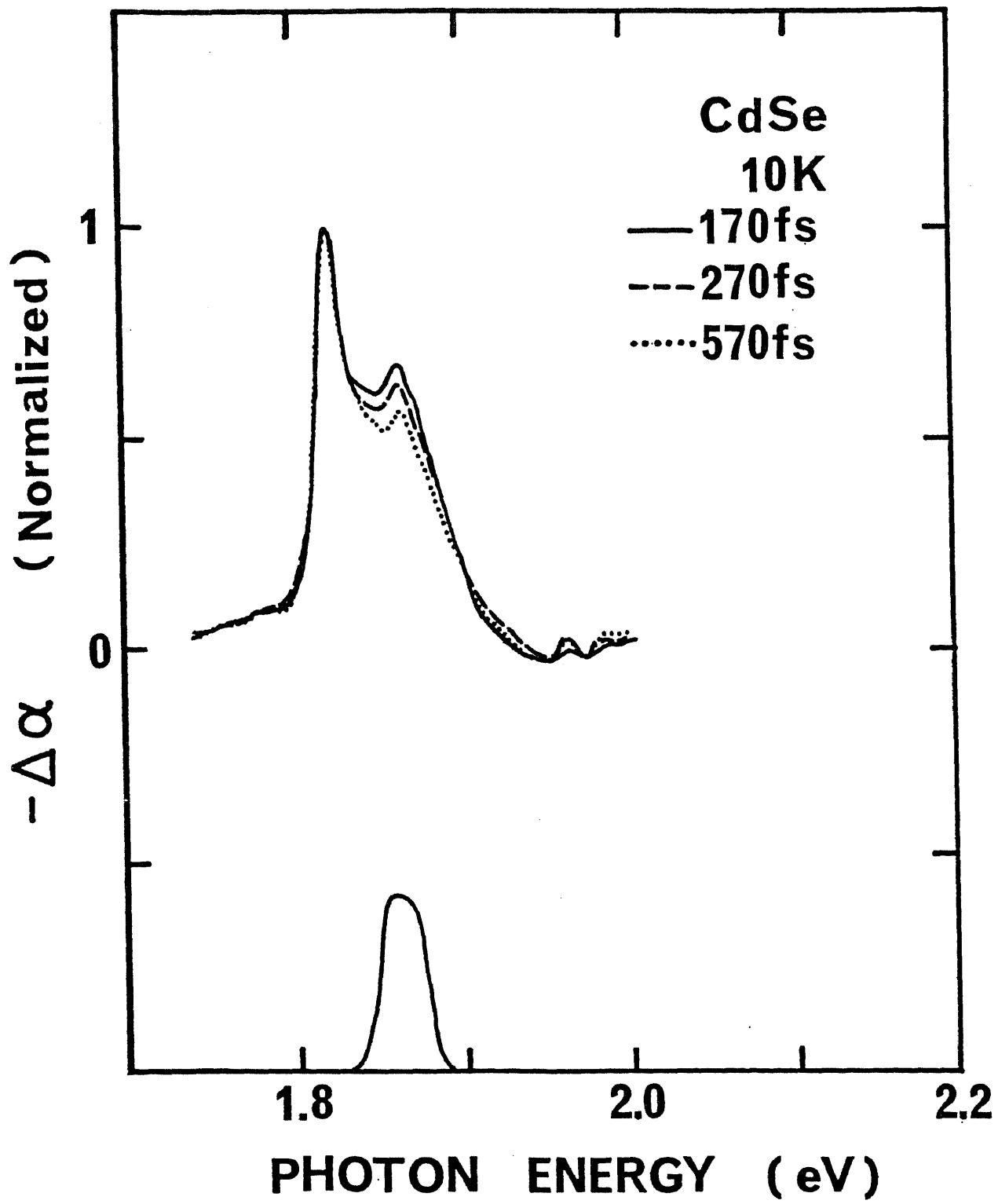


Fig. 24

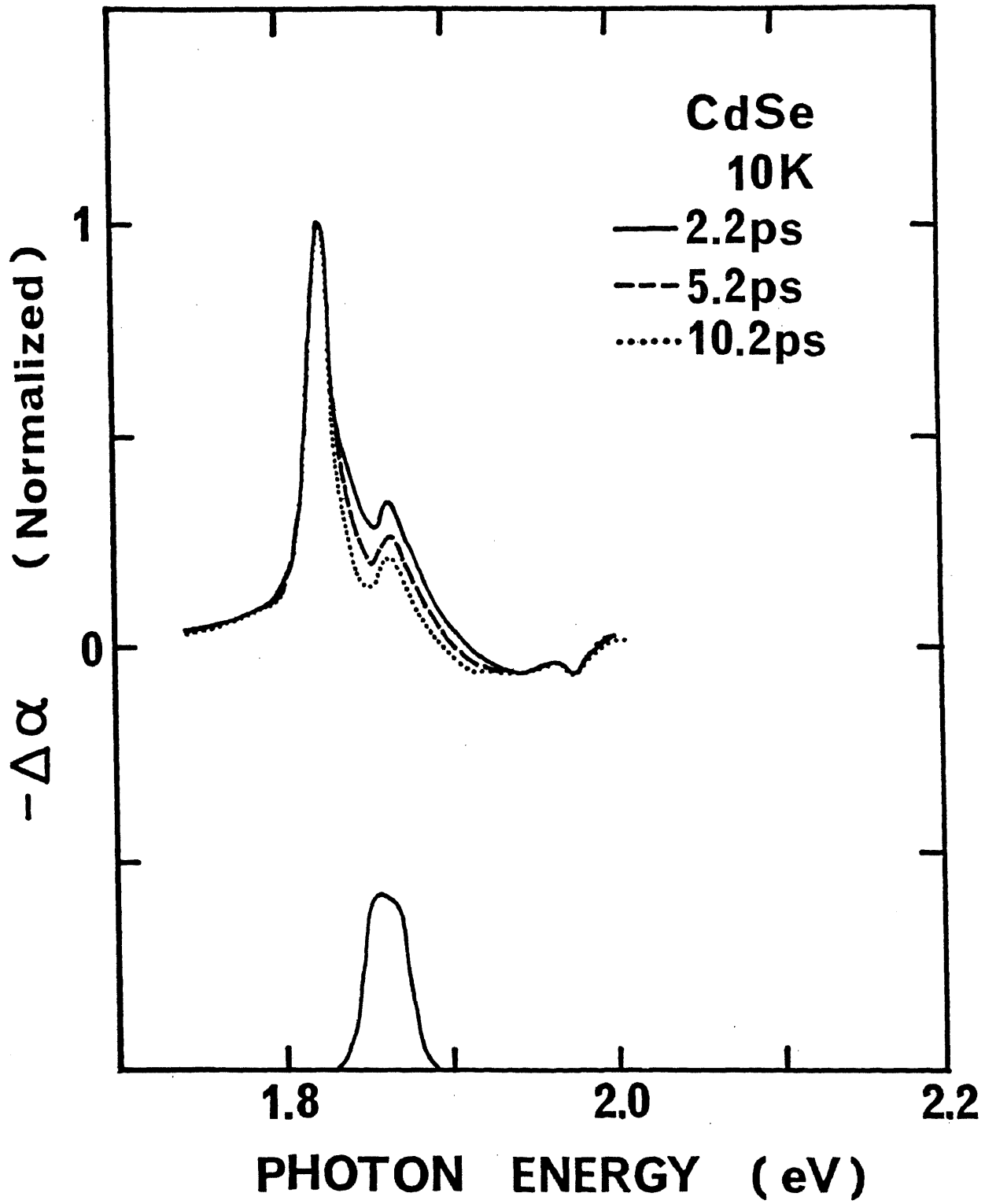


Fig. 25

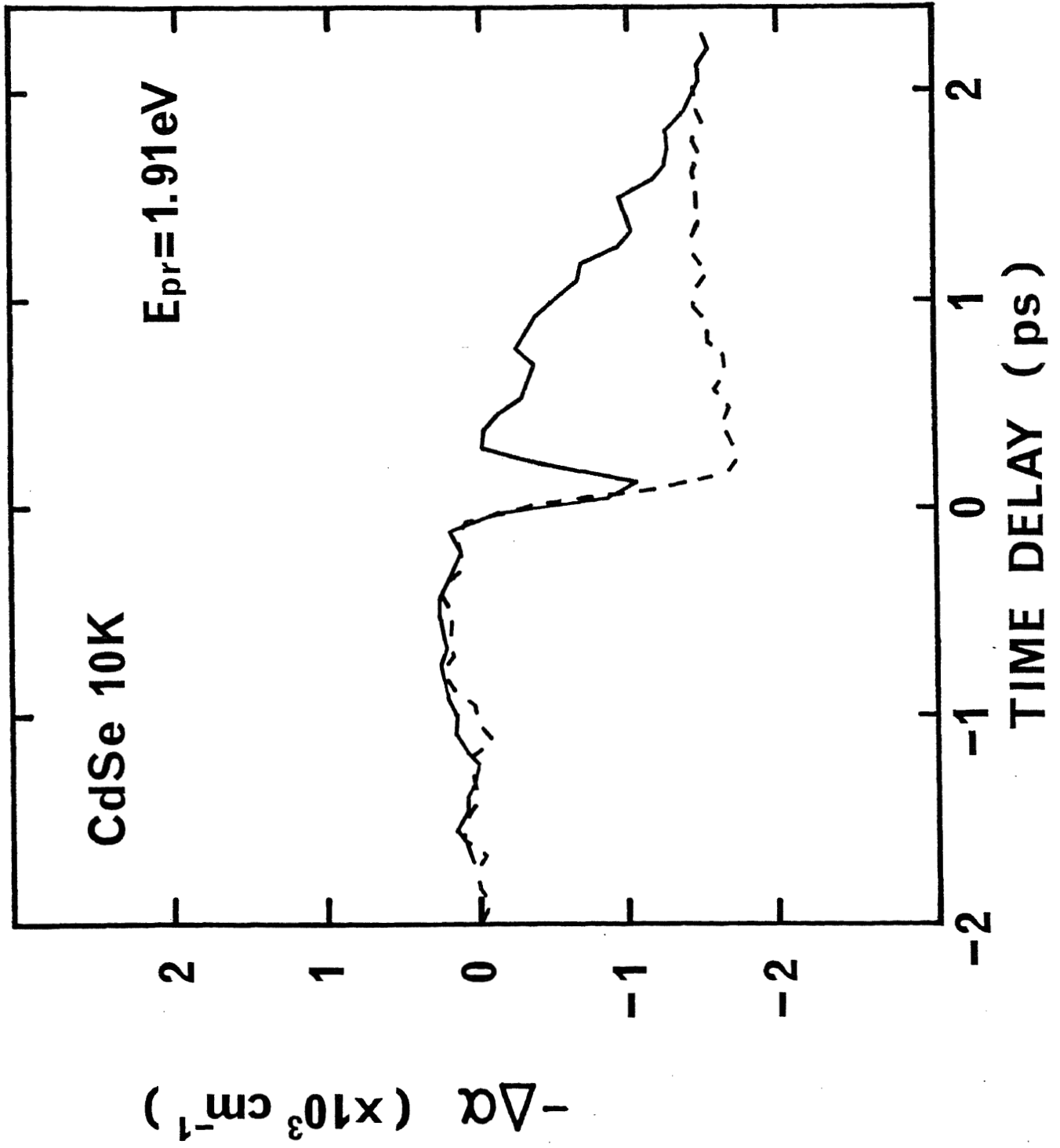


Fig. 26

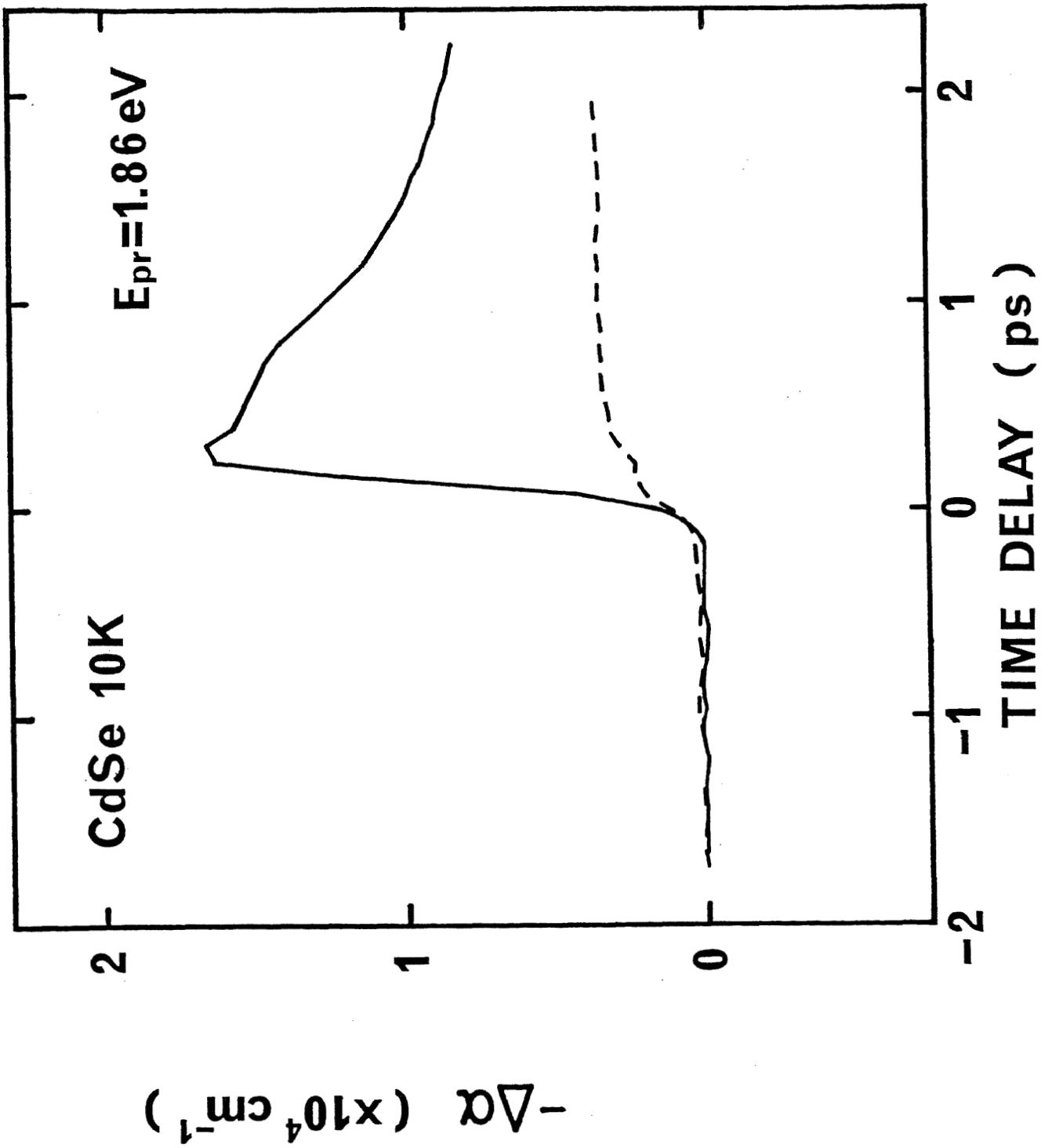


Fig. 27

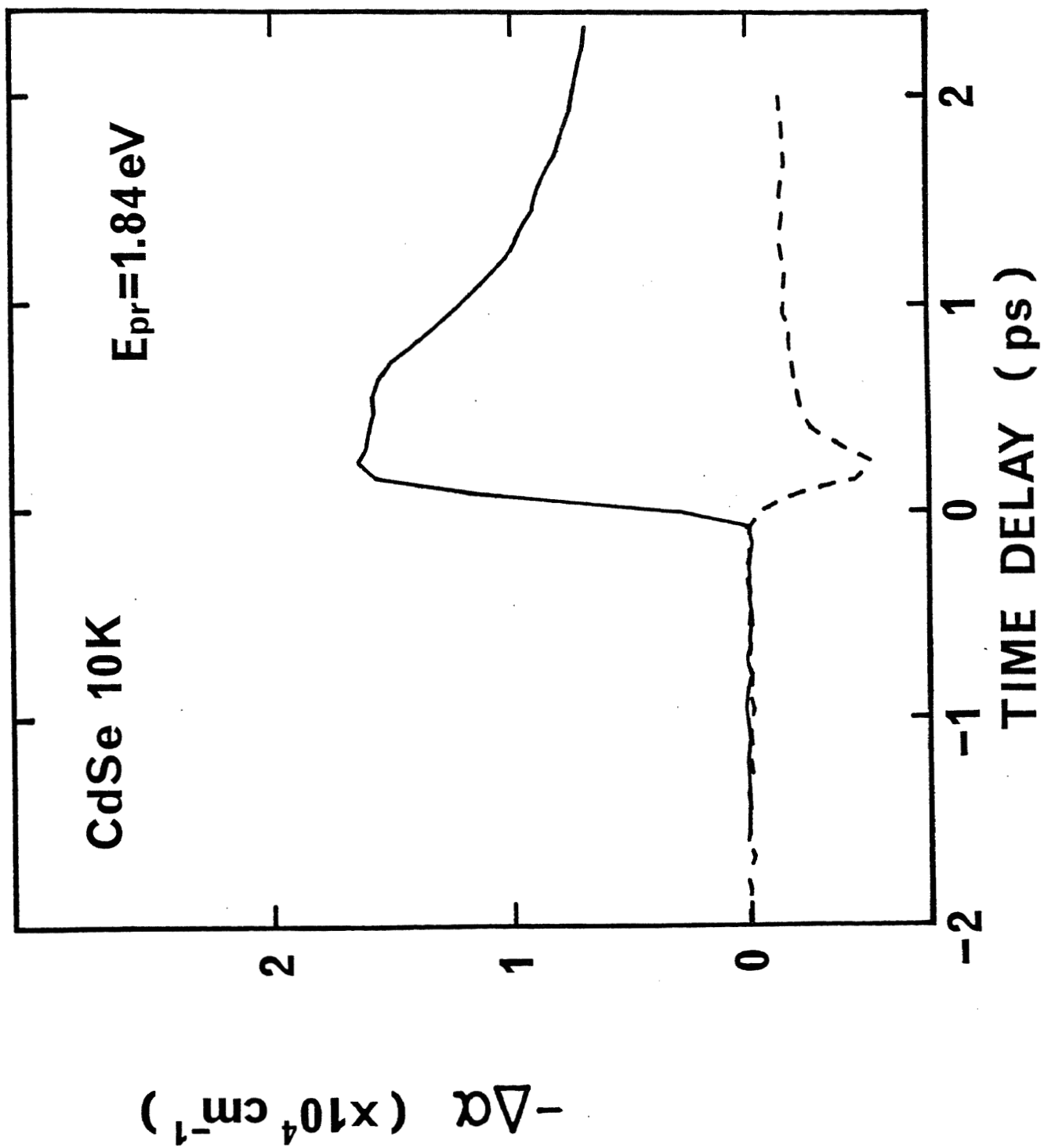


Fig. 28

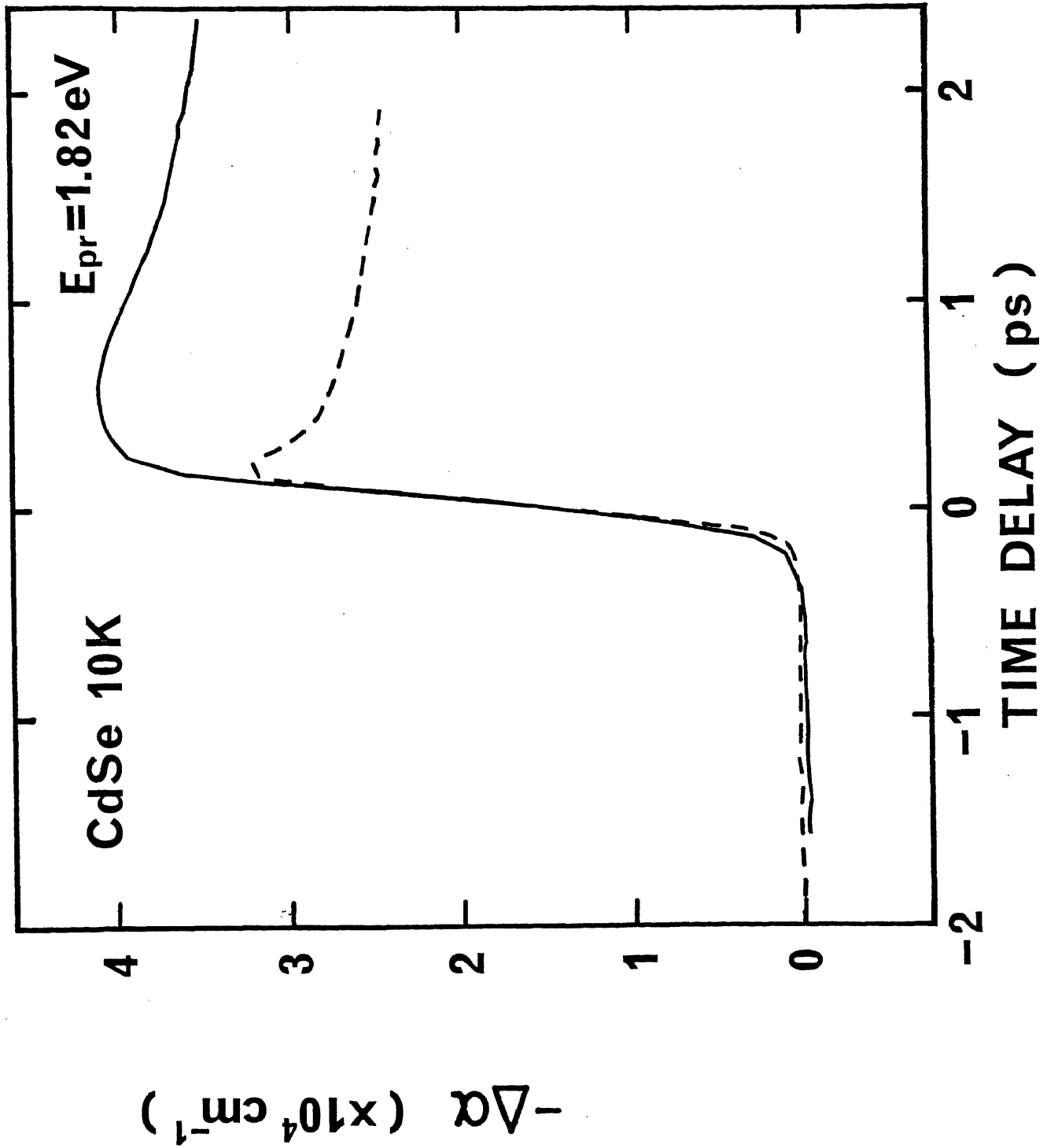


Fig. 29

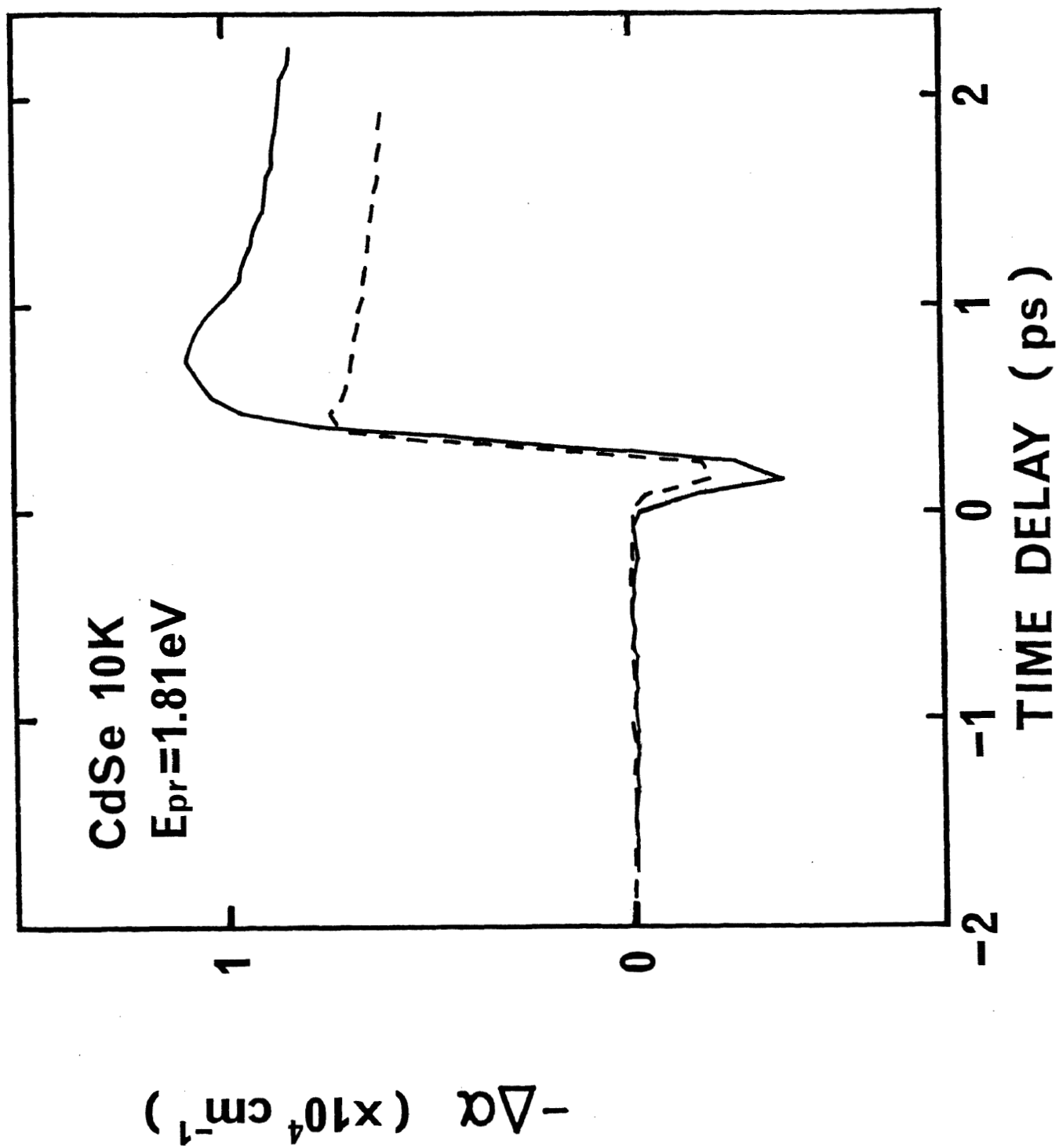


Fig. 30

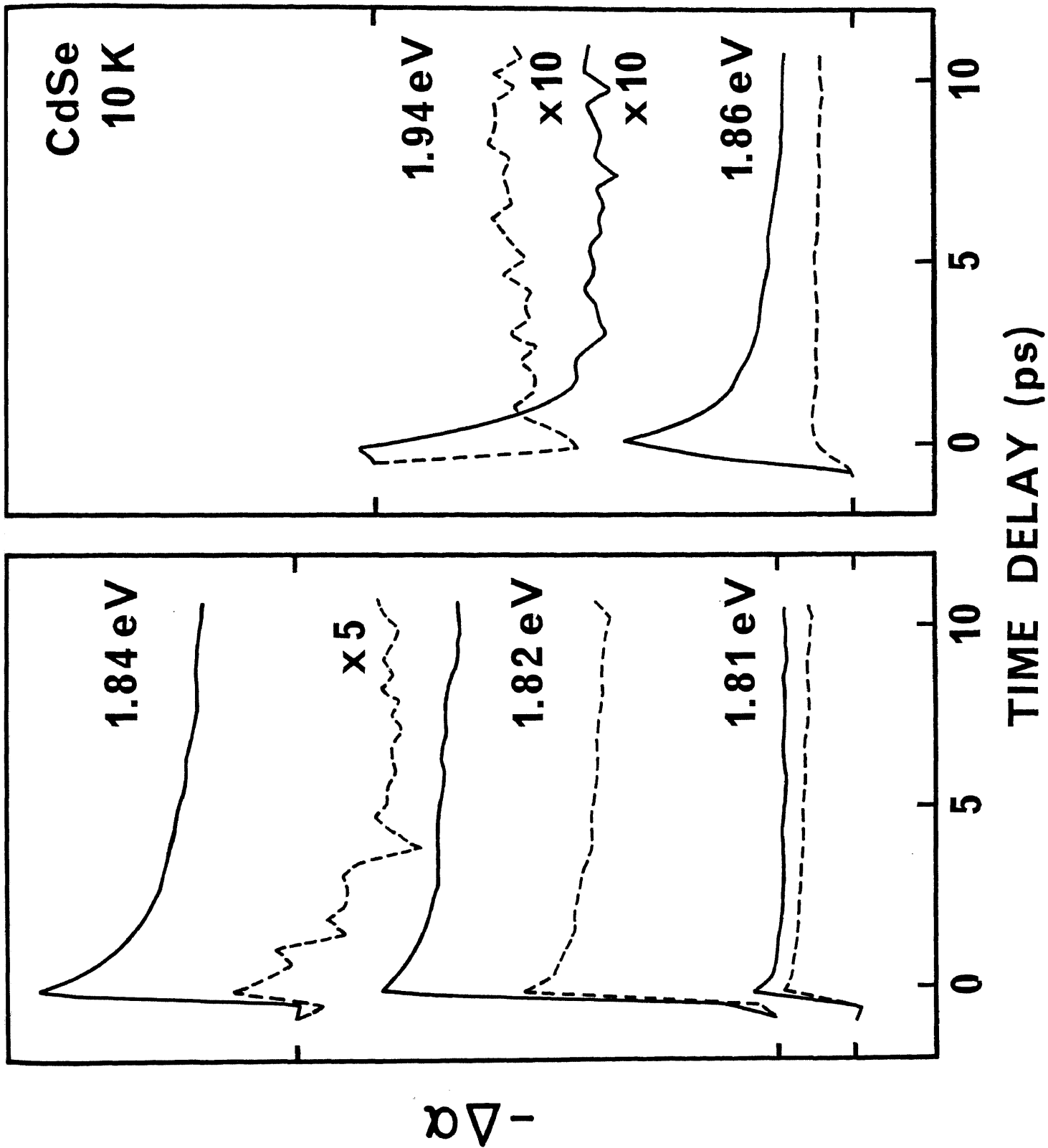


Fig. 31

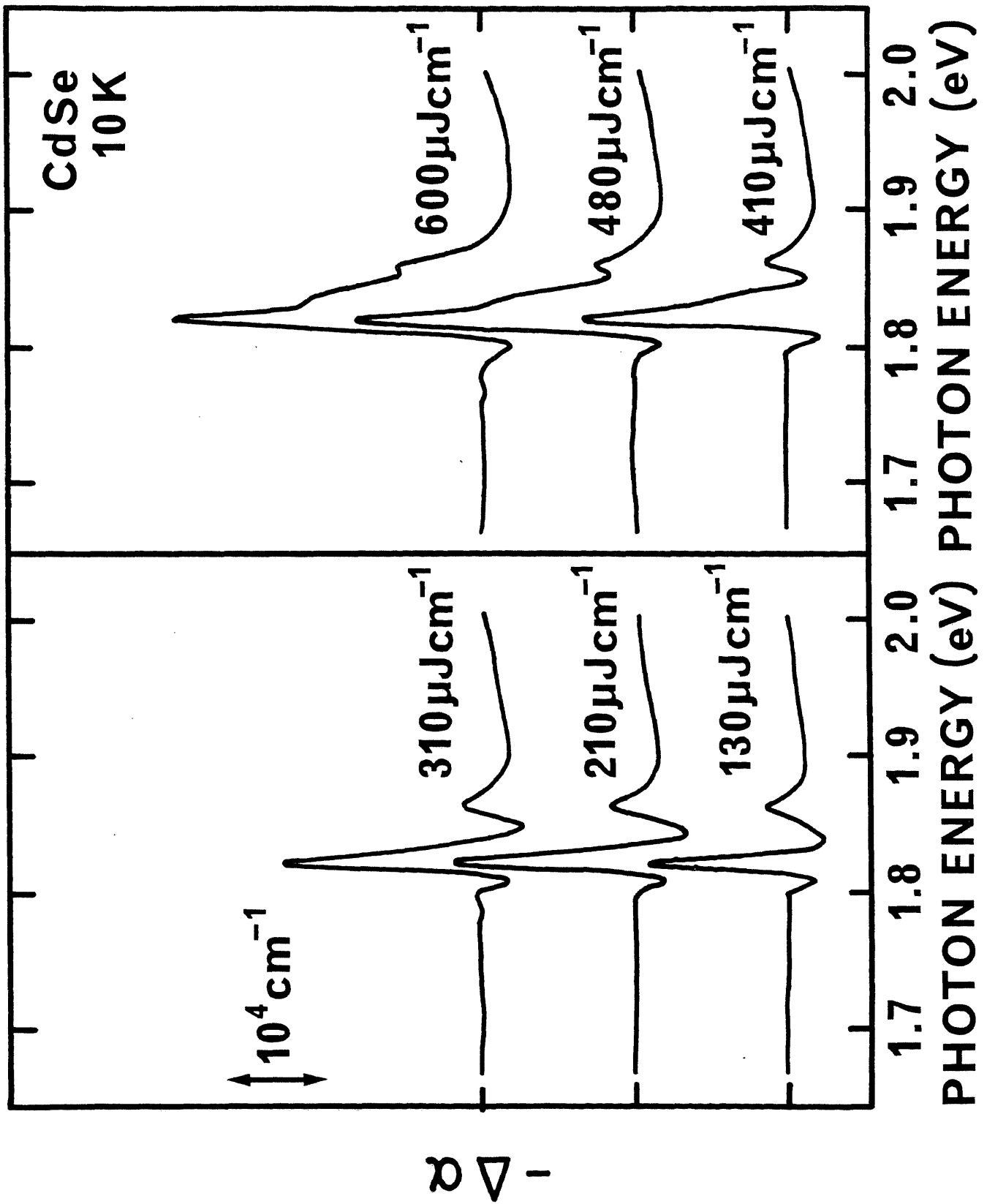


Fig. 32

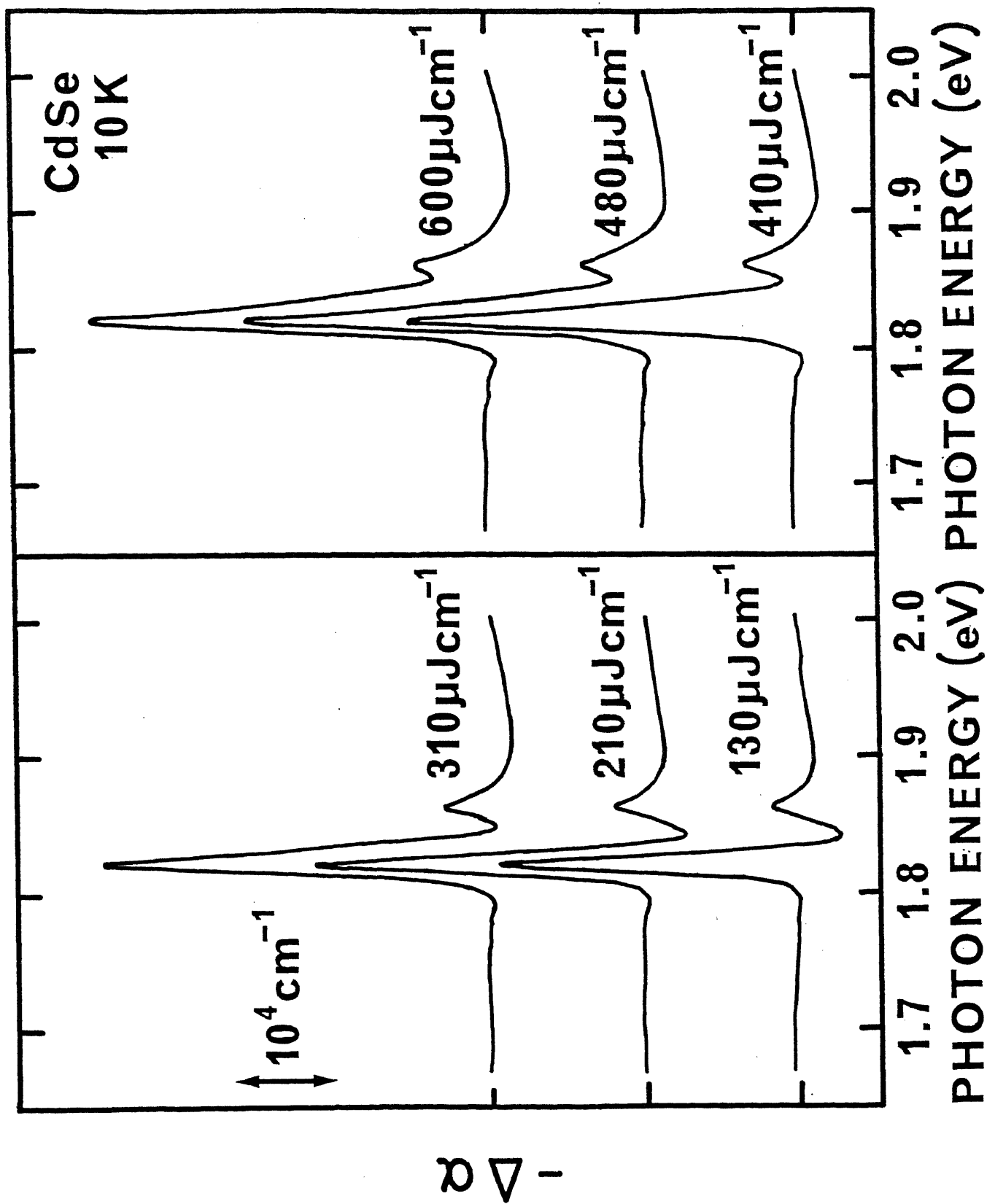


Fig. 33

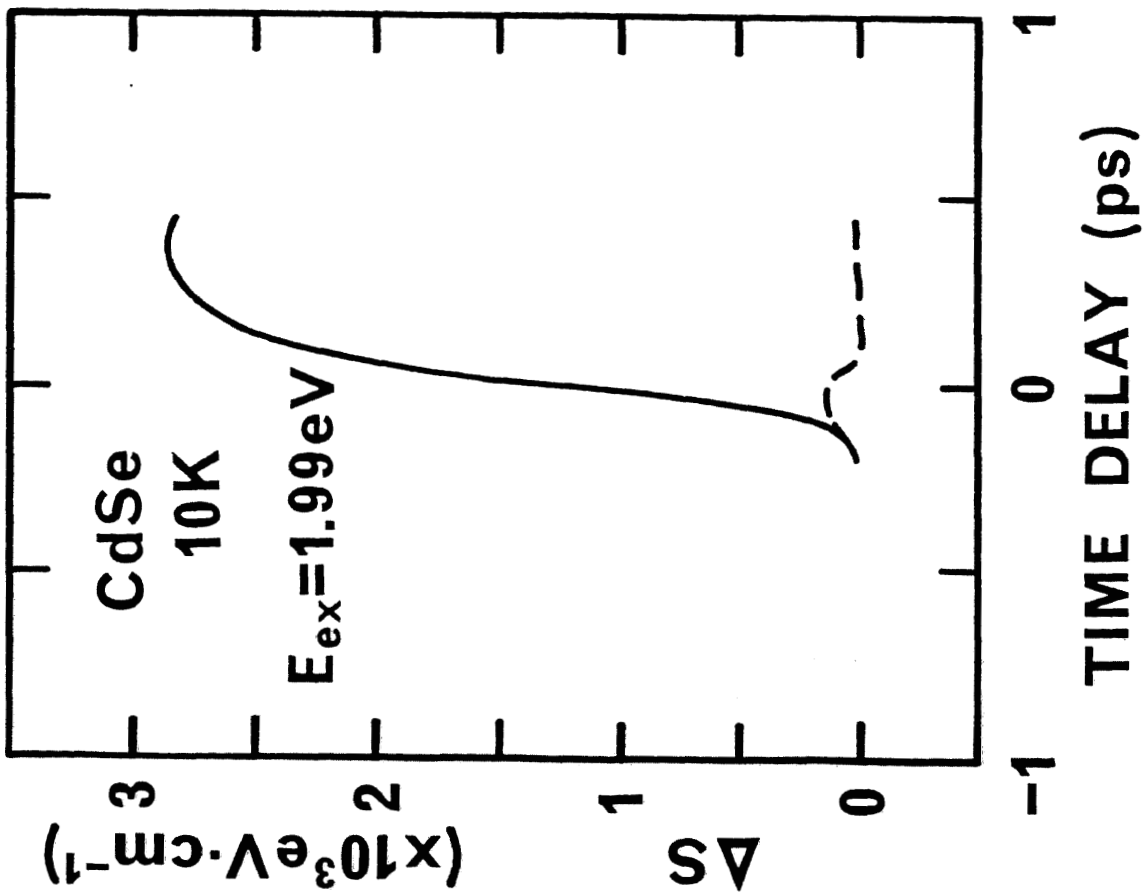
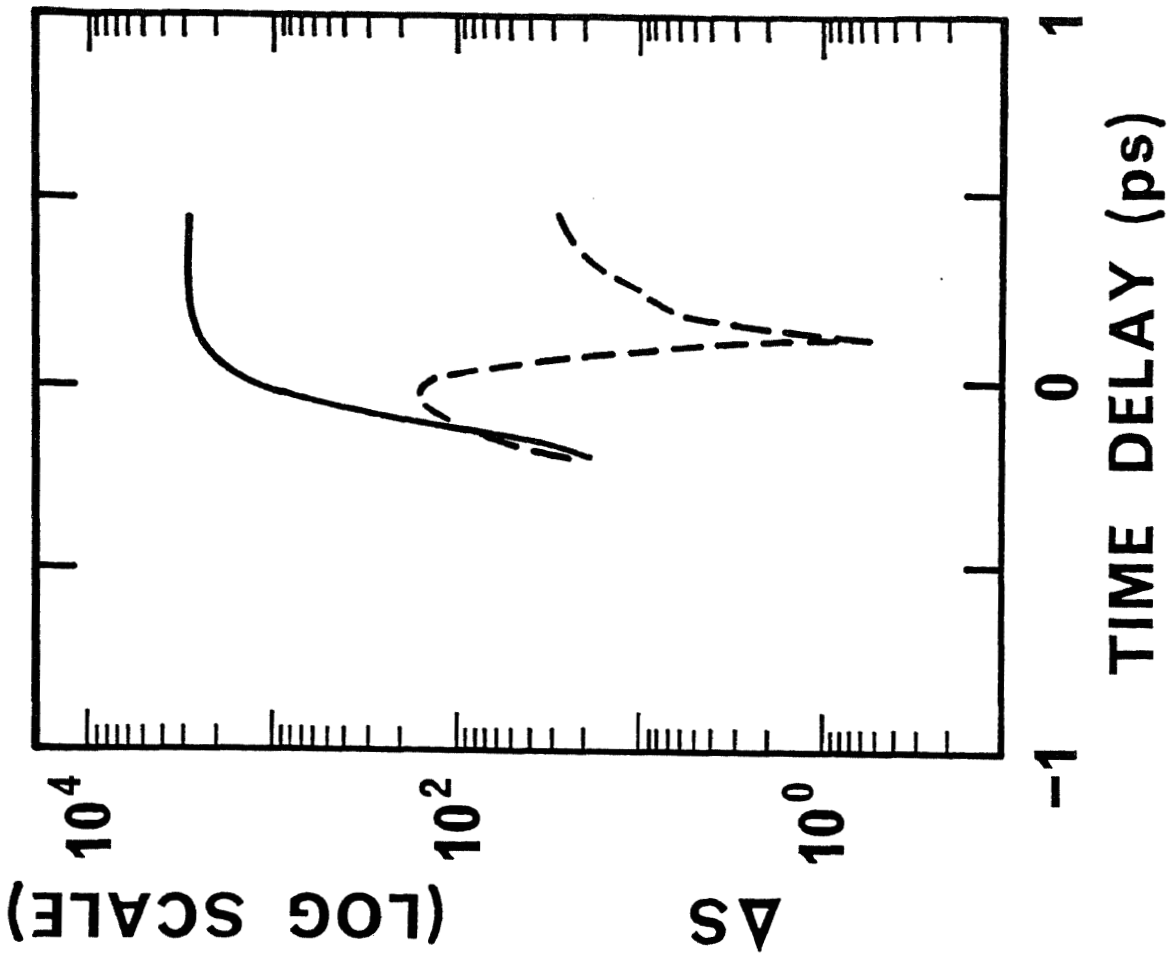


Fig. 34

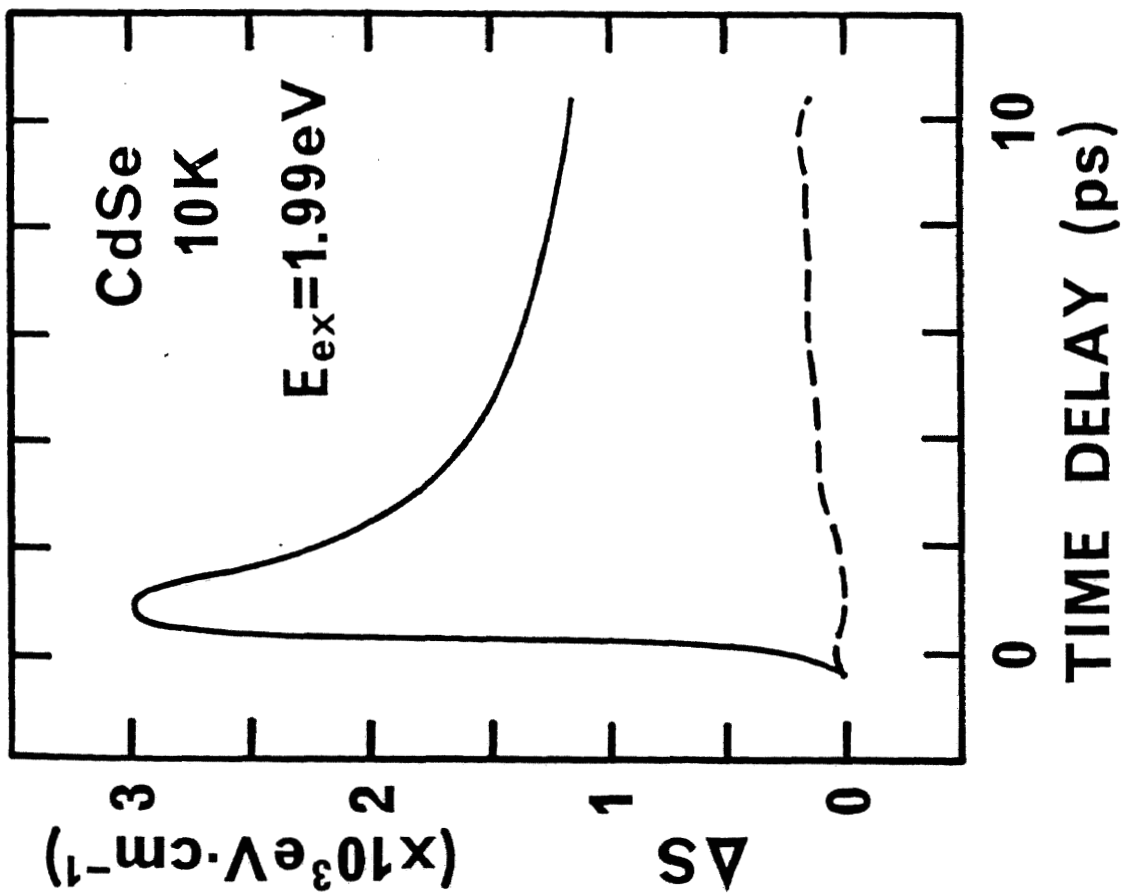
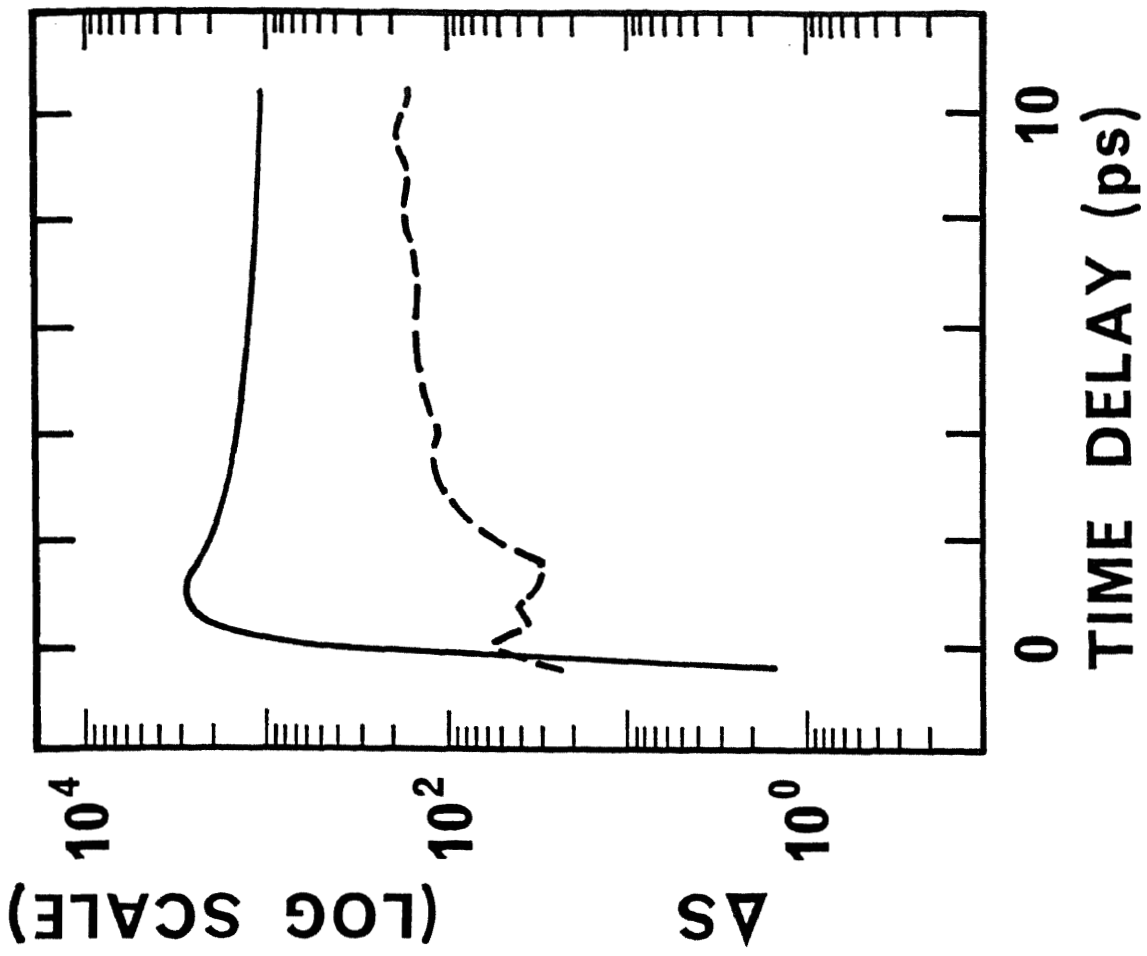


Fig. 35

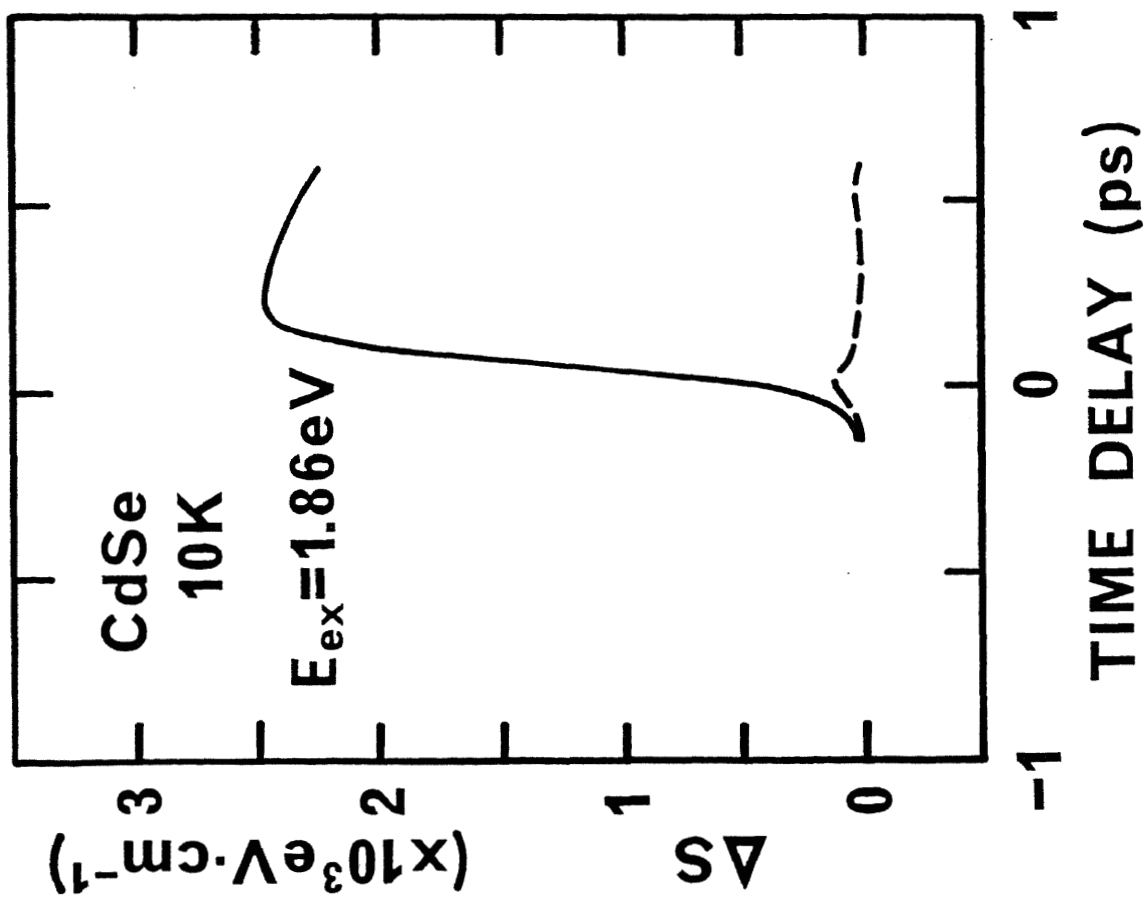
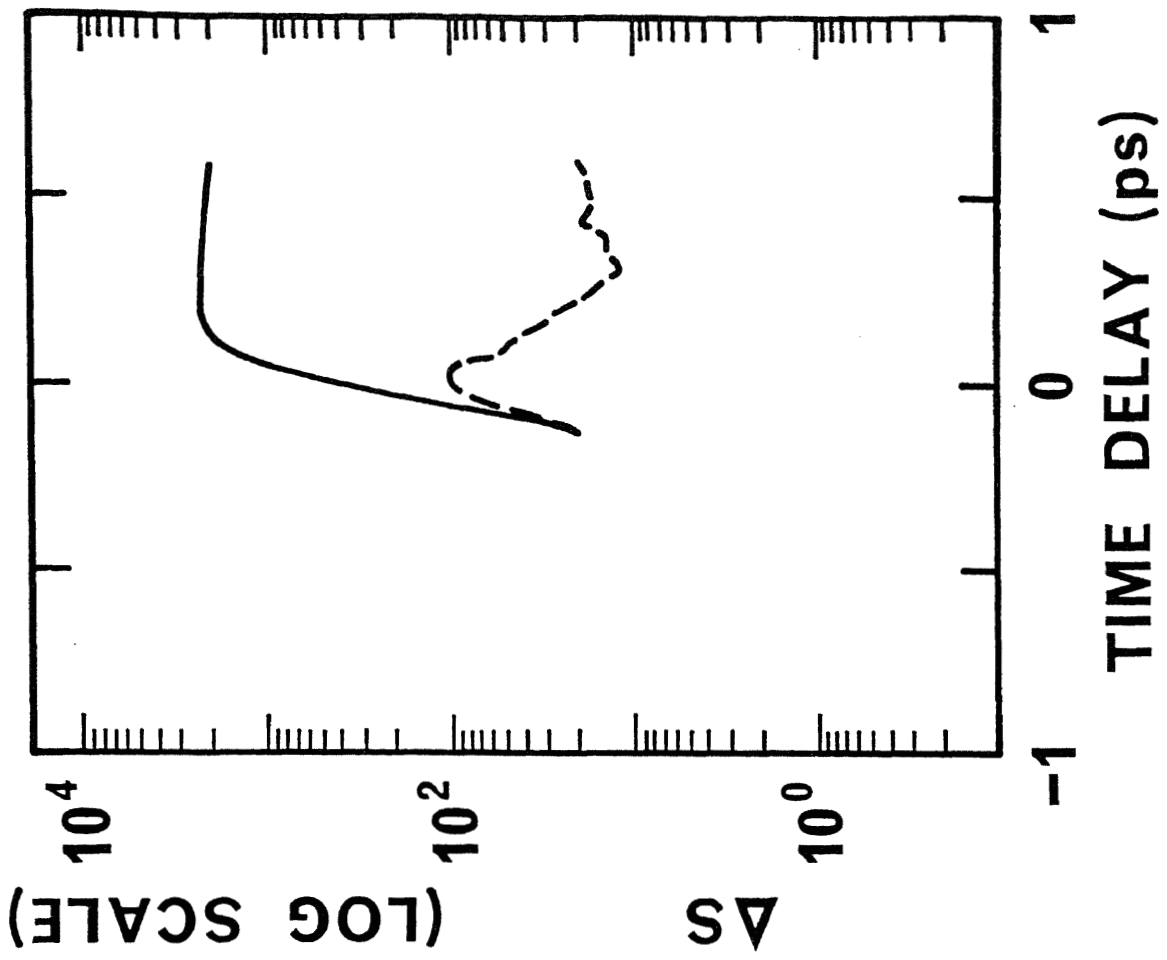


Fig. 36

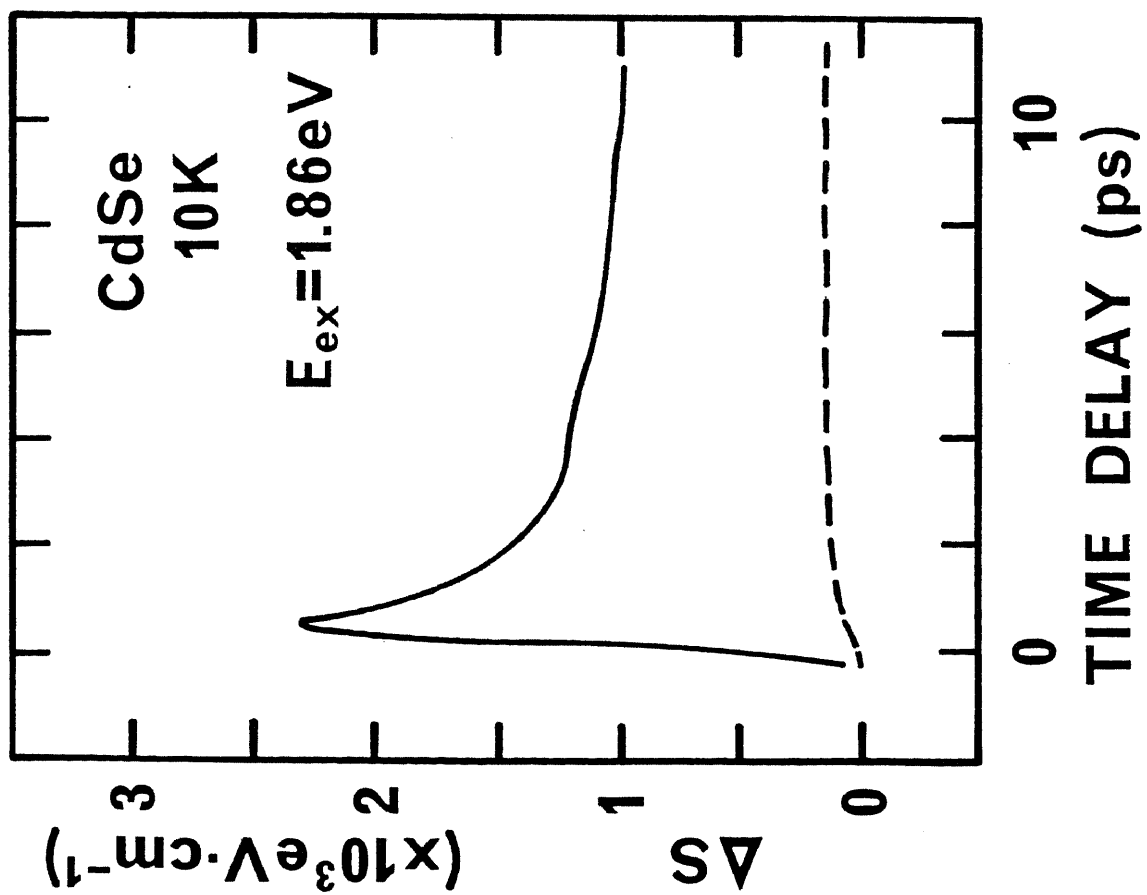
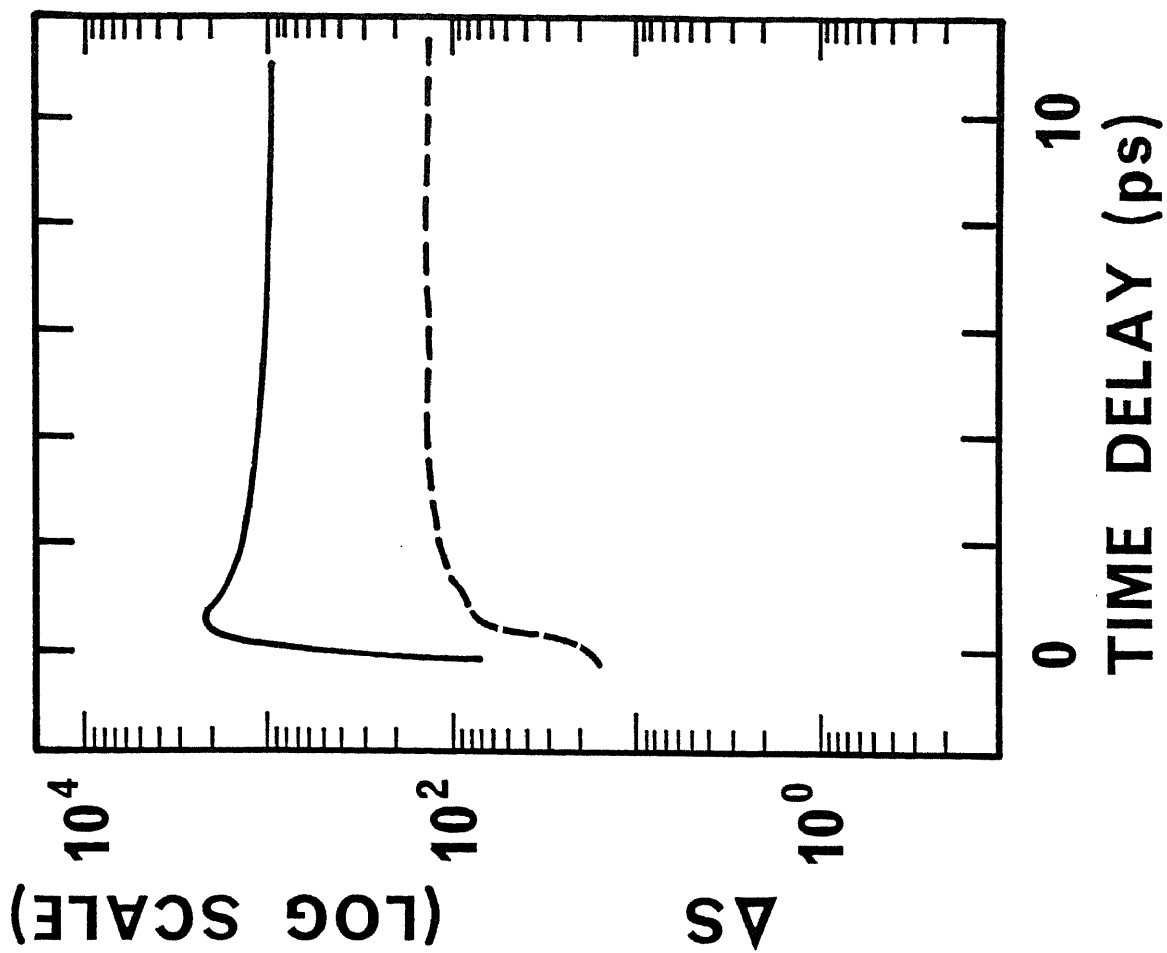


Fig. 37

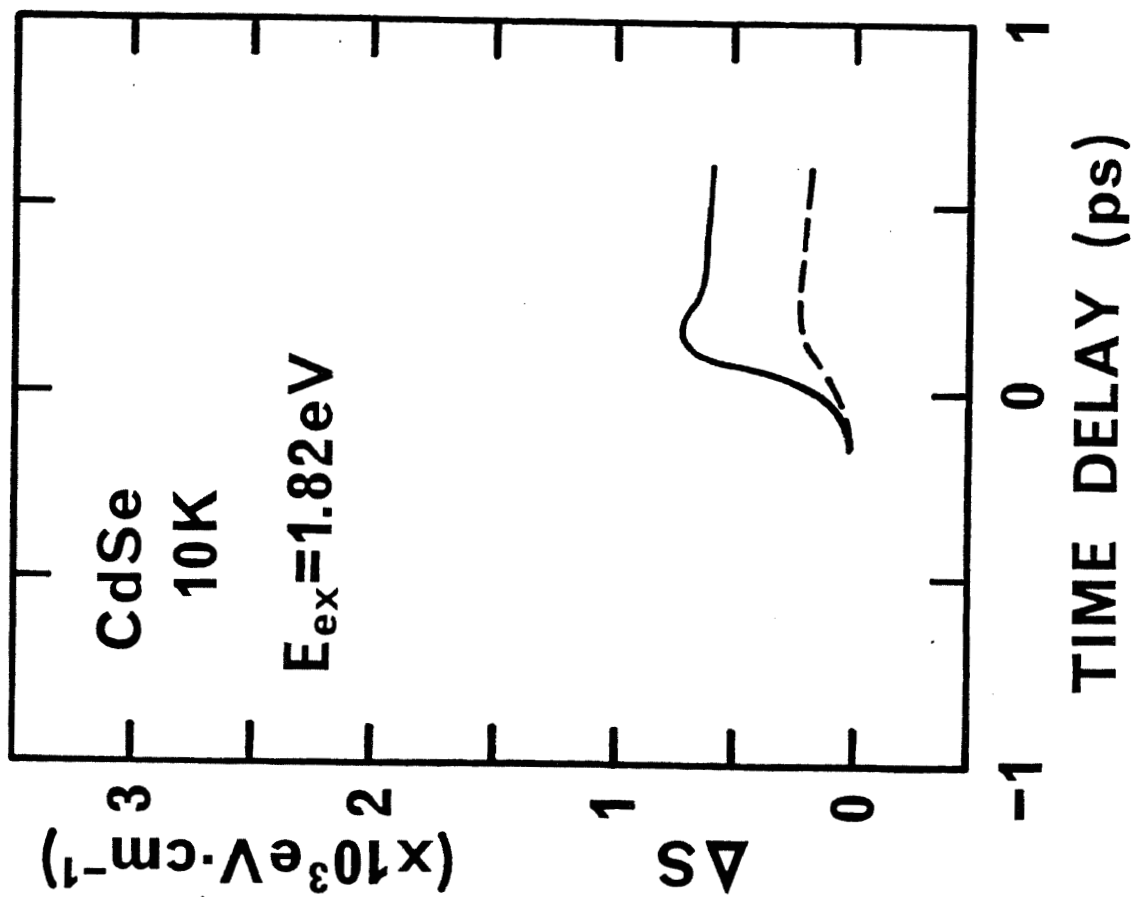
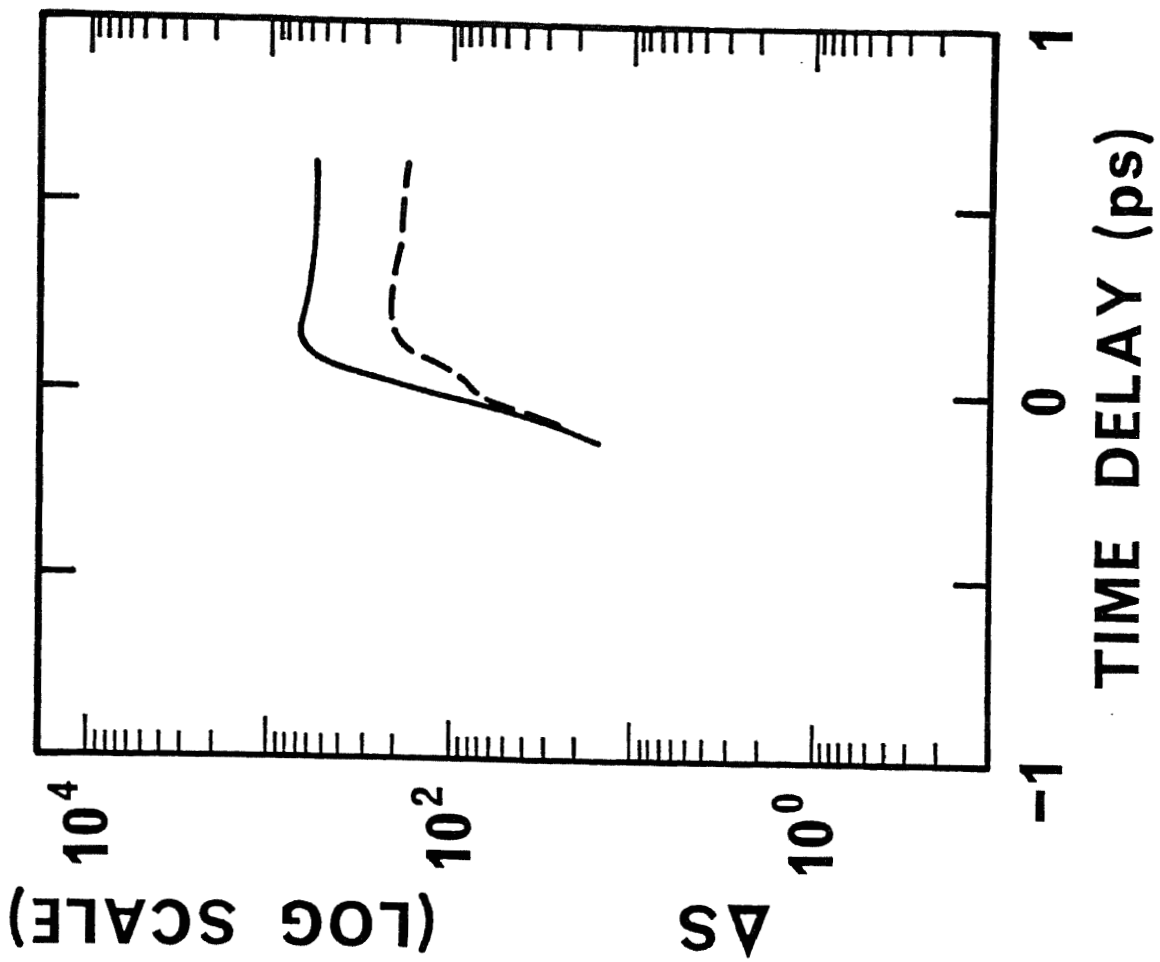


Fig. 38

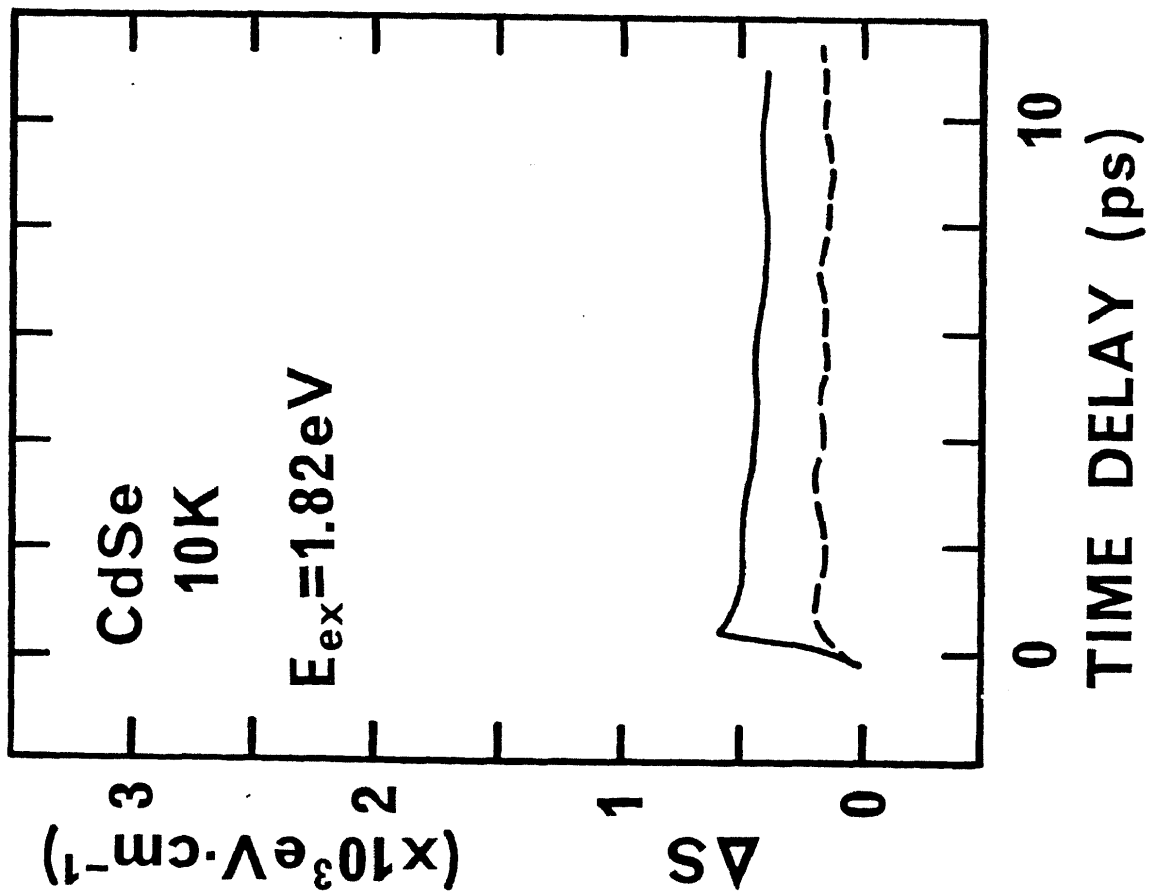
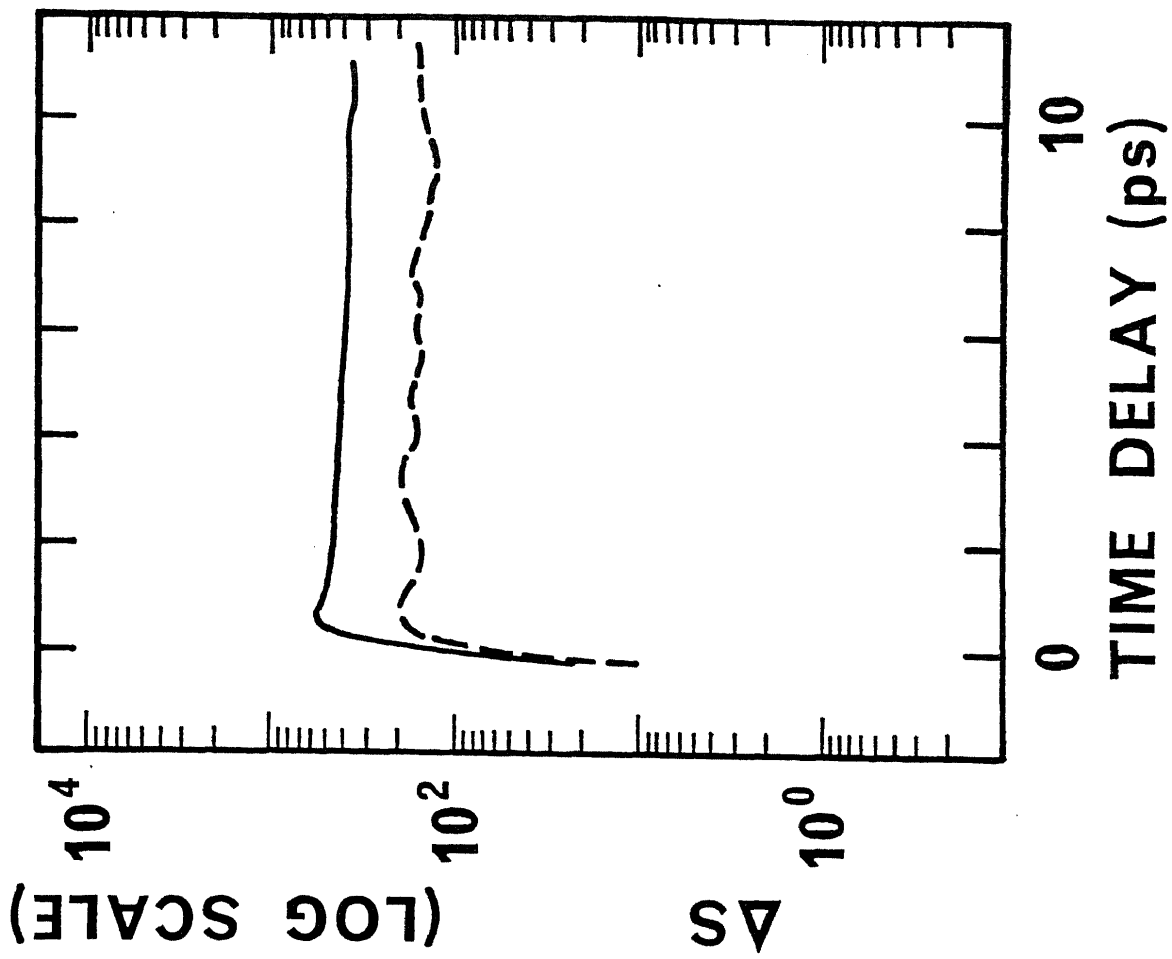


Fig. 39

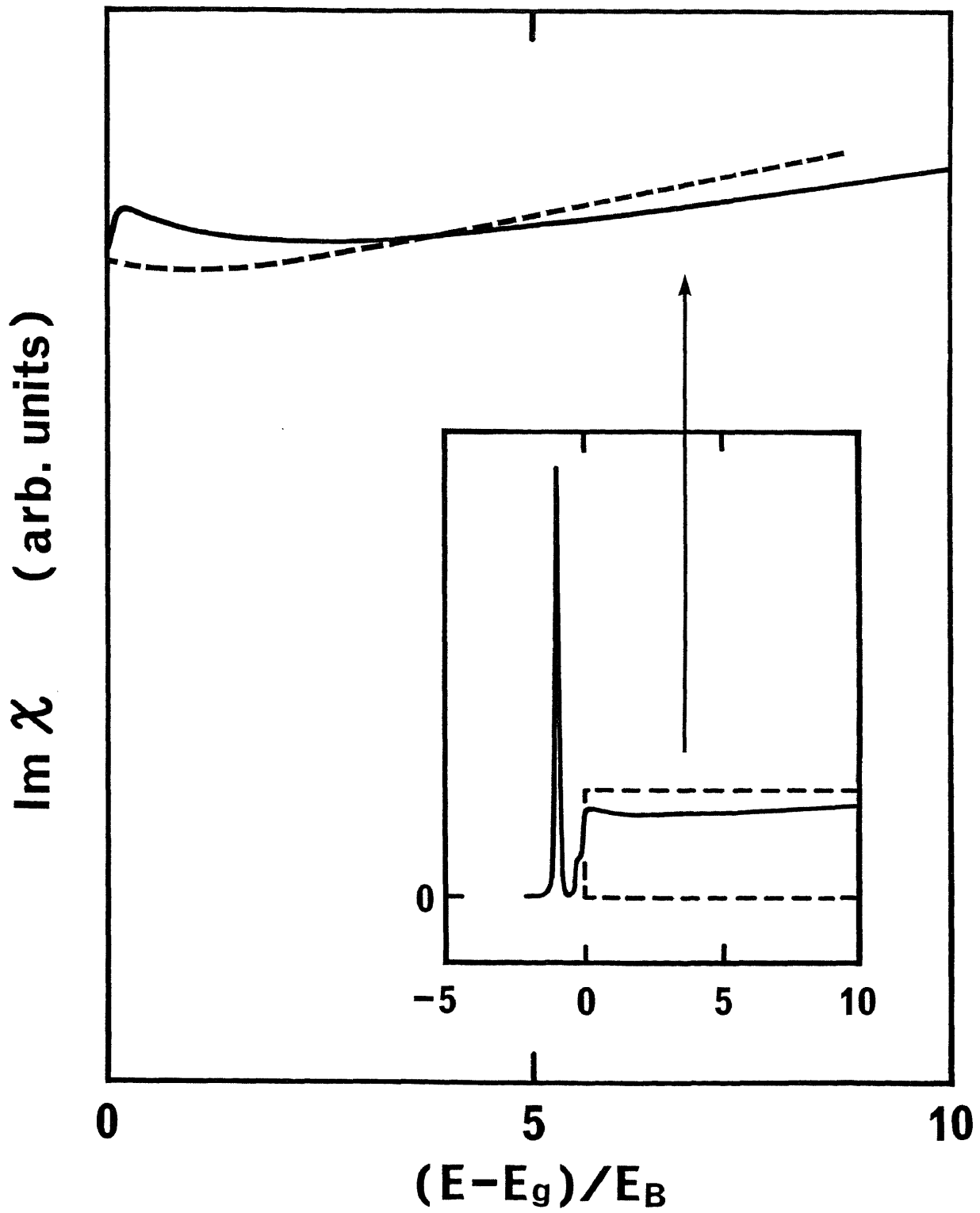


Fig. 40

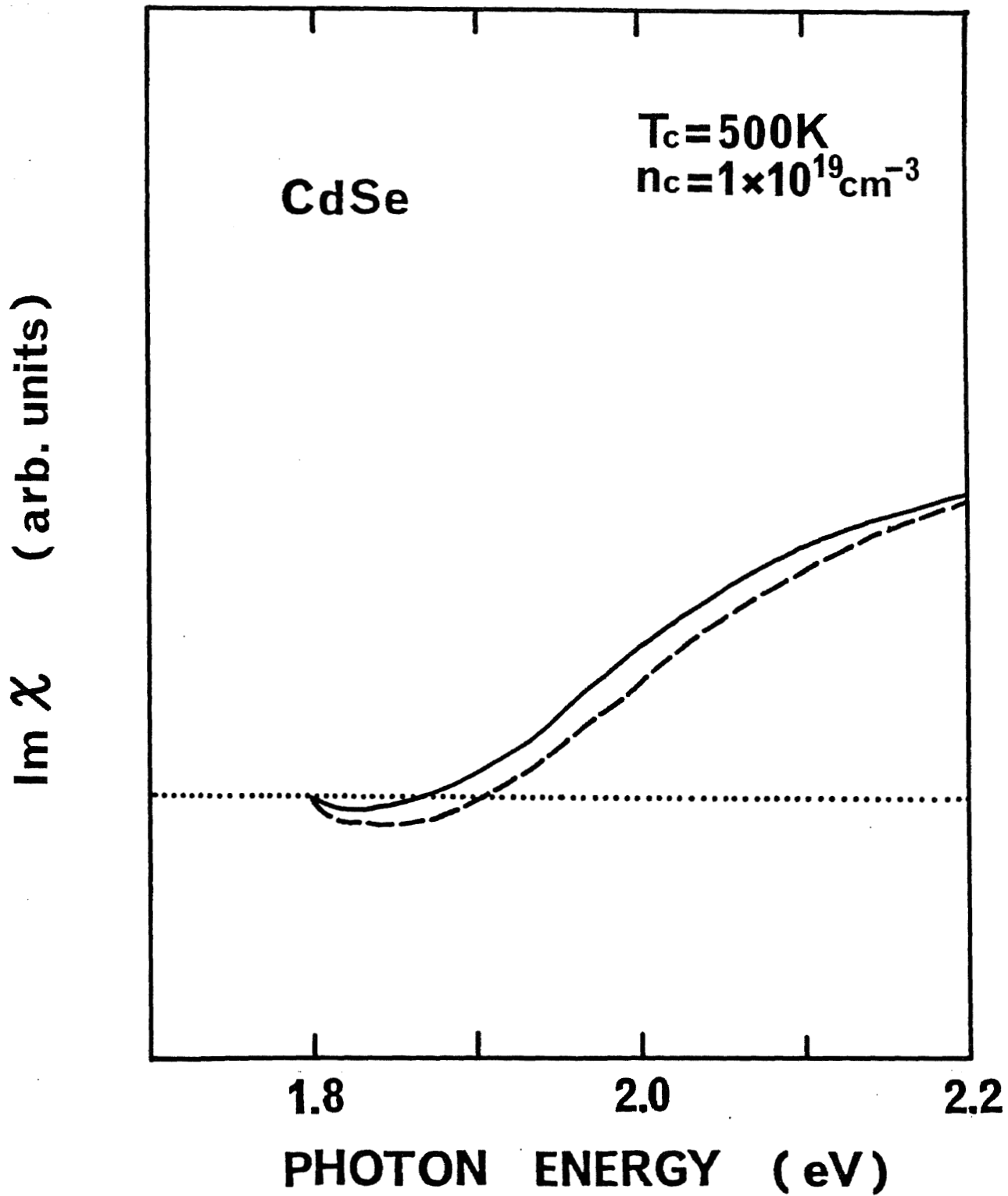


Fig. 41

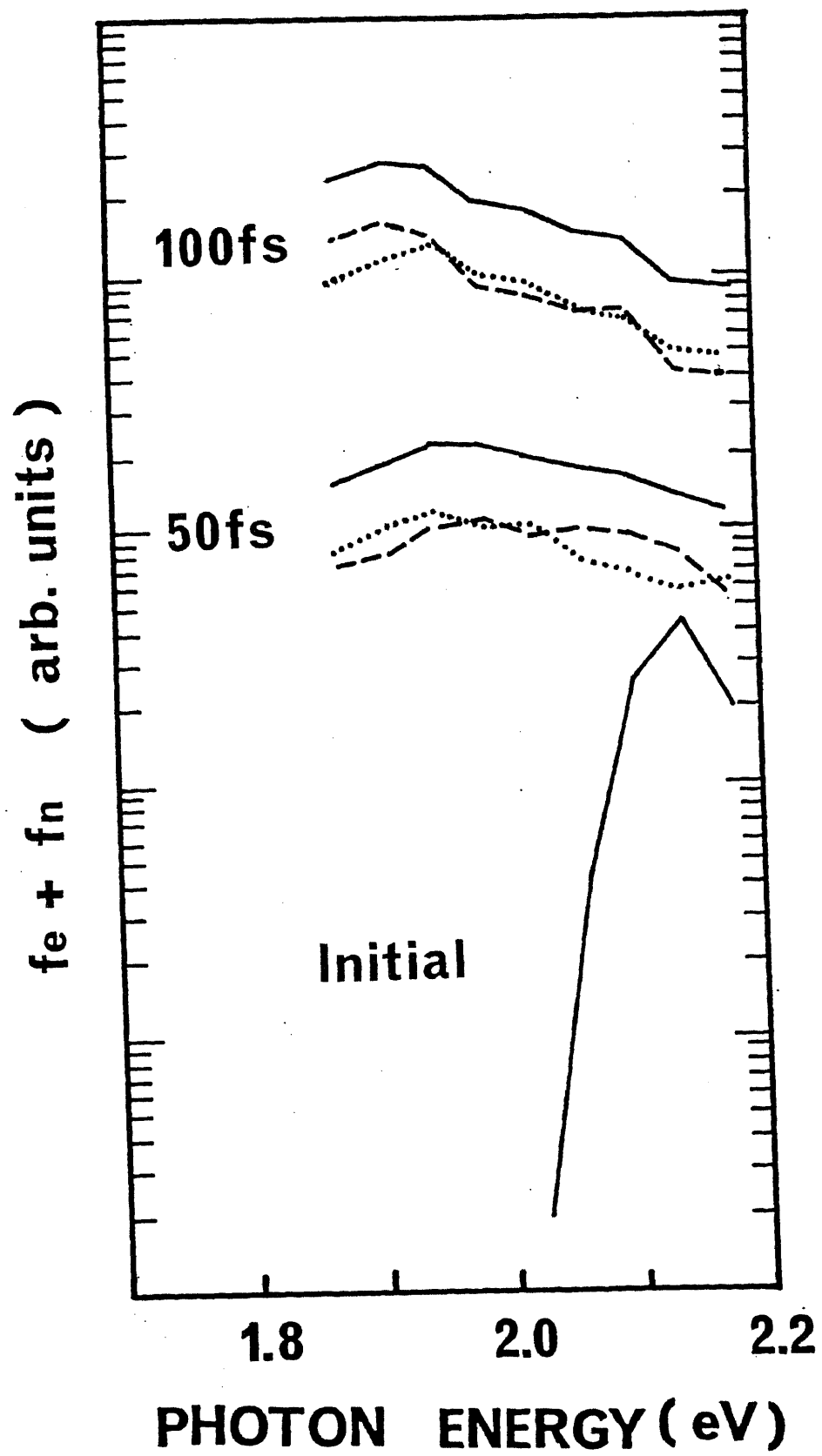


Fig. 42

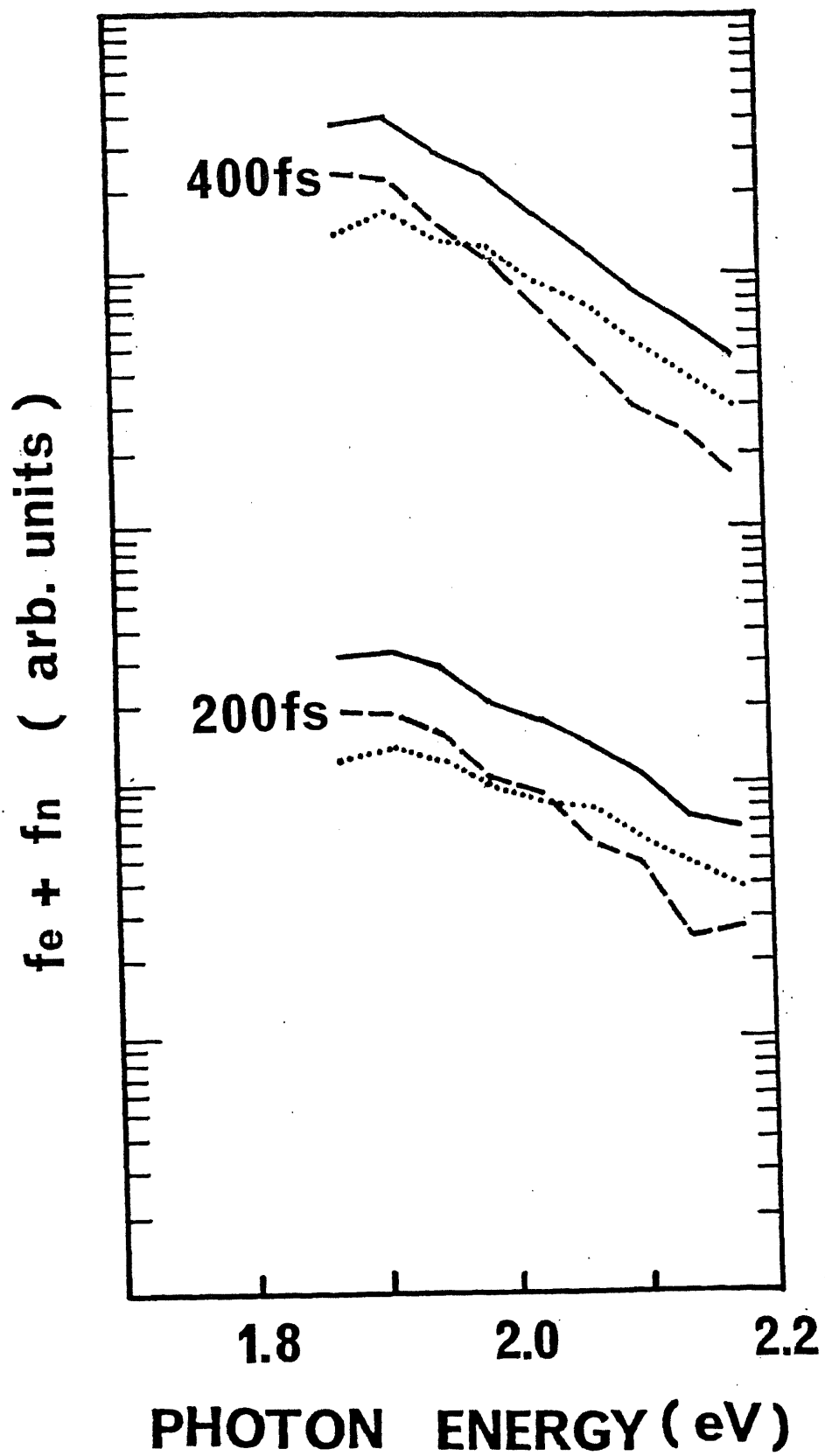


Fig. 43

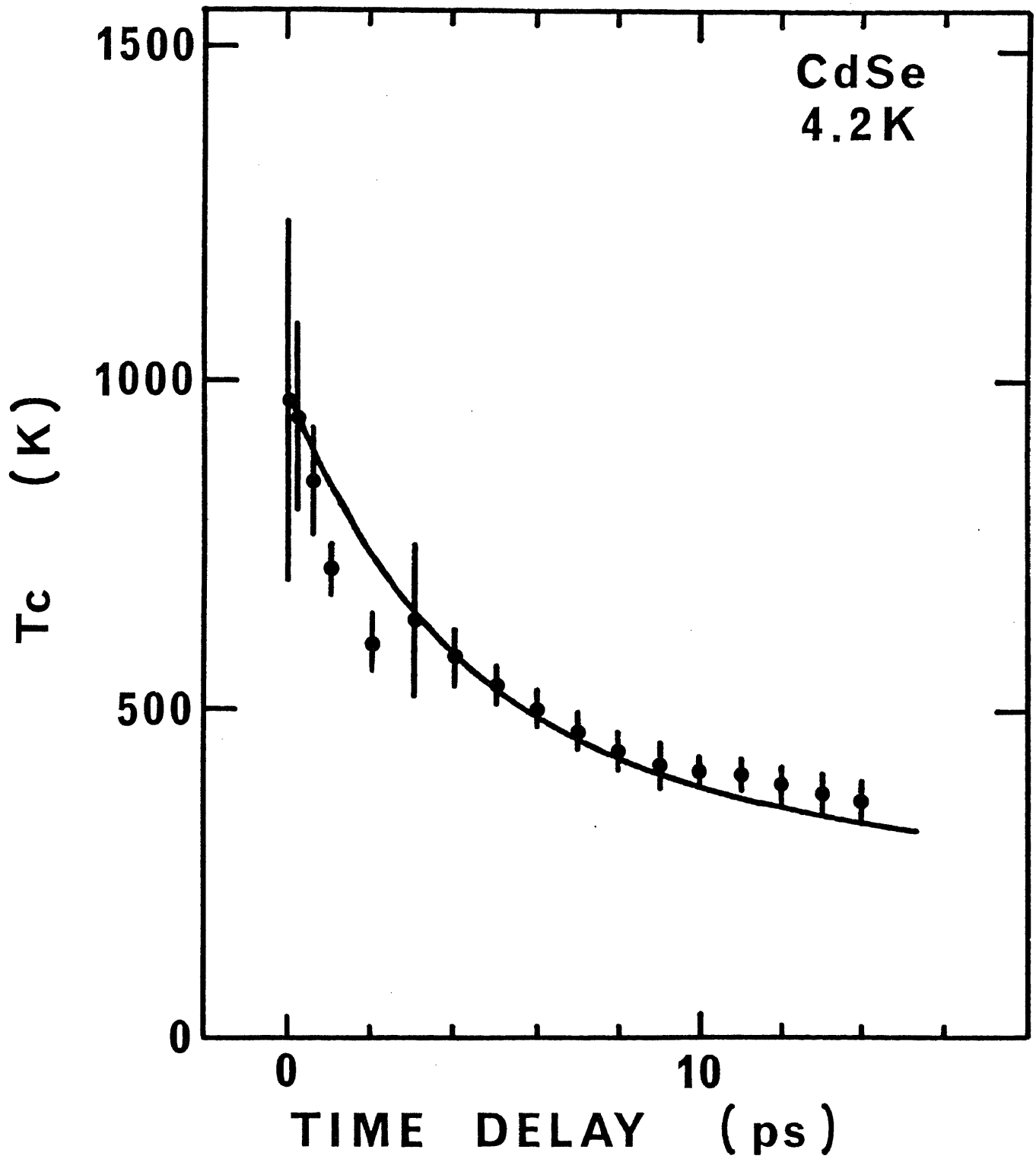


Fig. 44

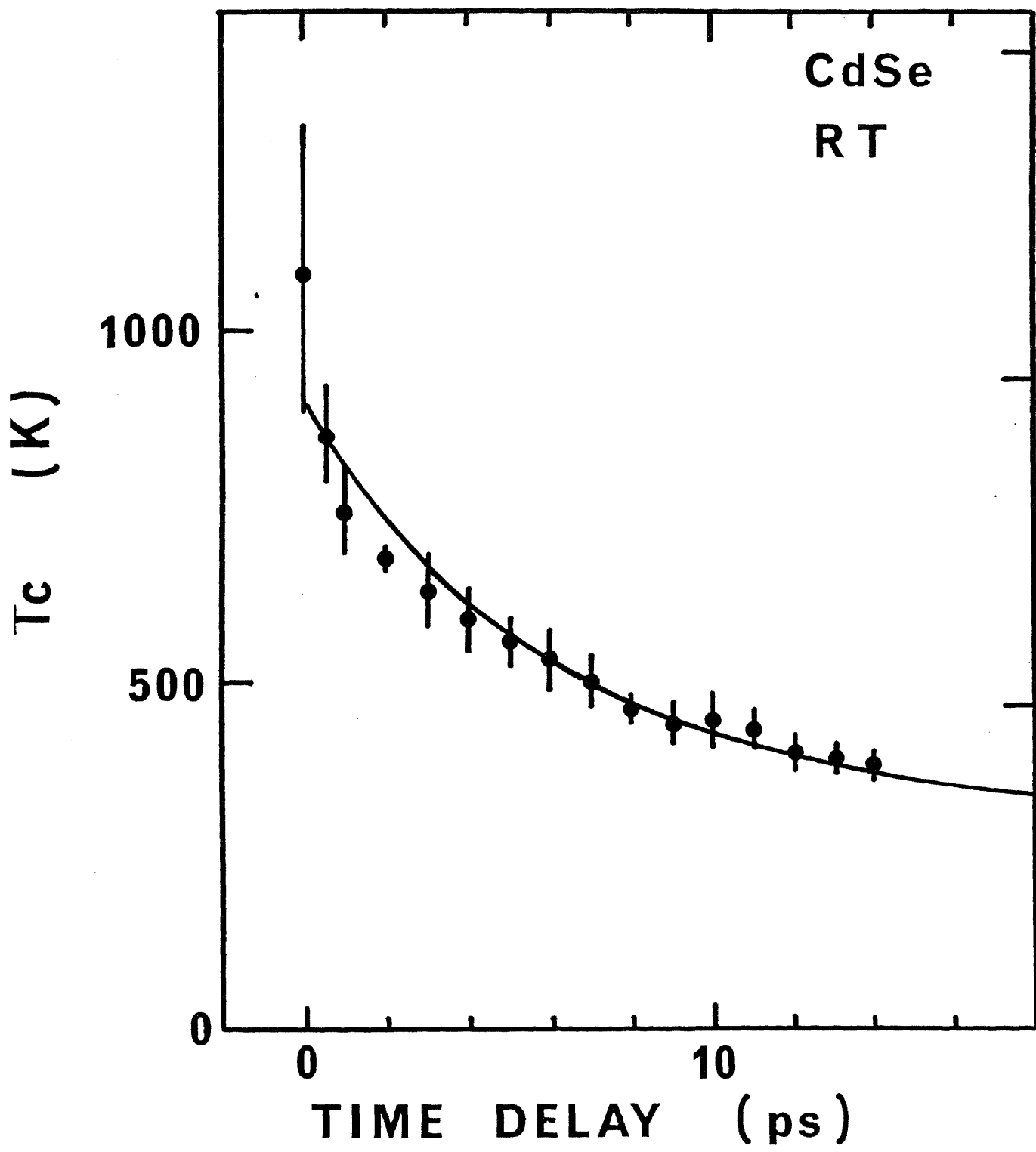


Fig. 45

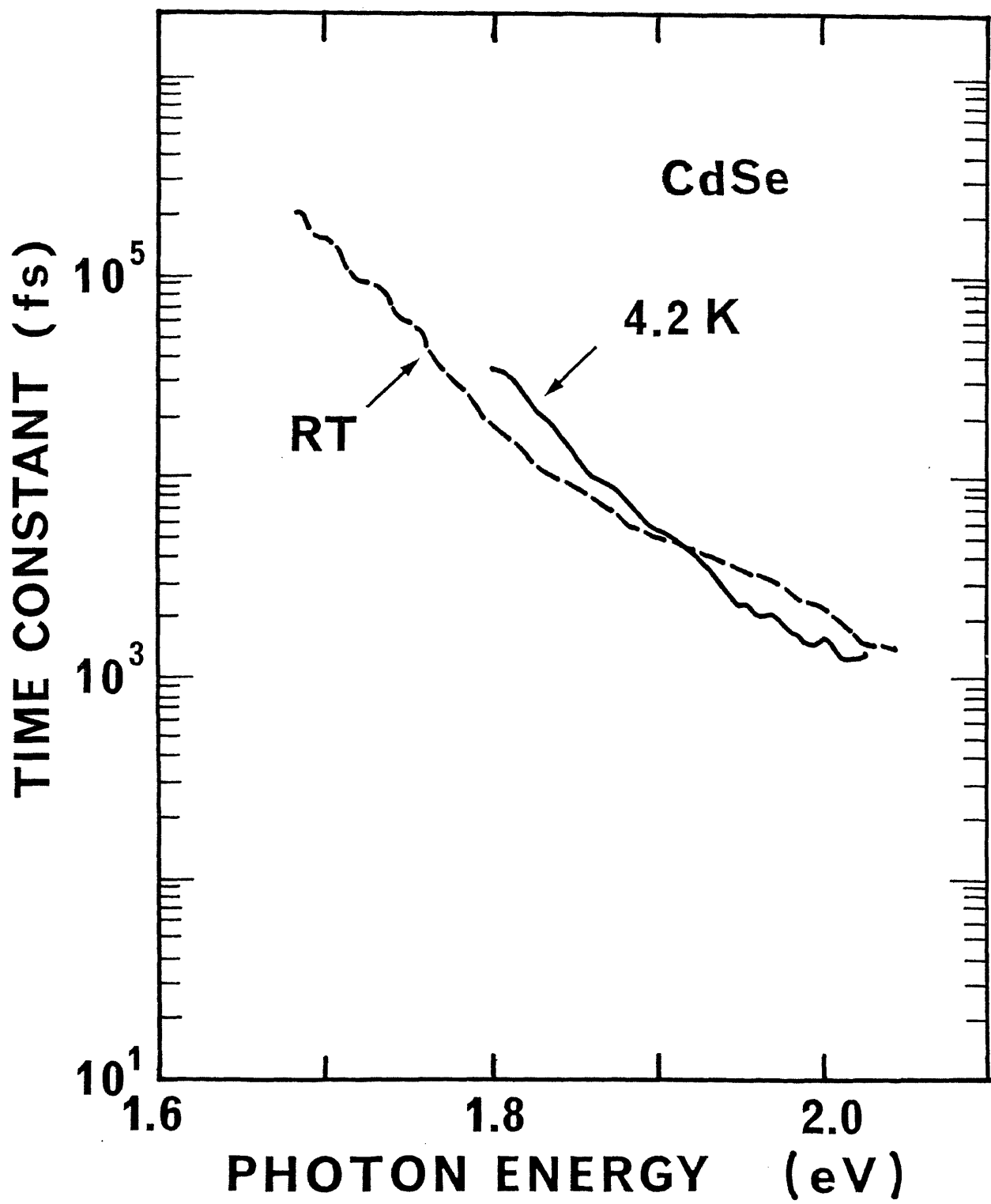


Fig. 46

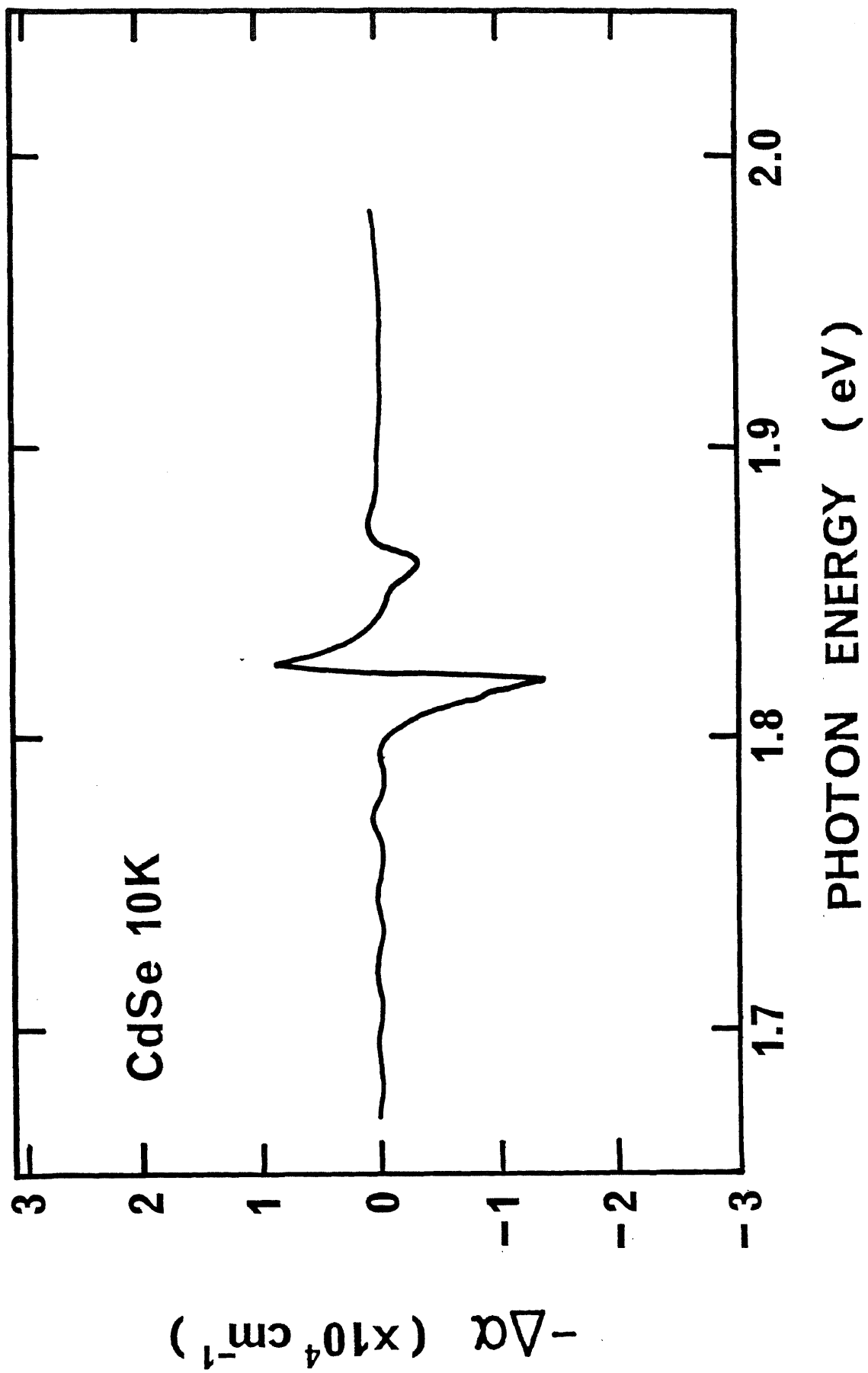


Fig. 47

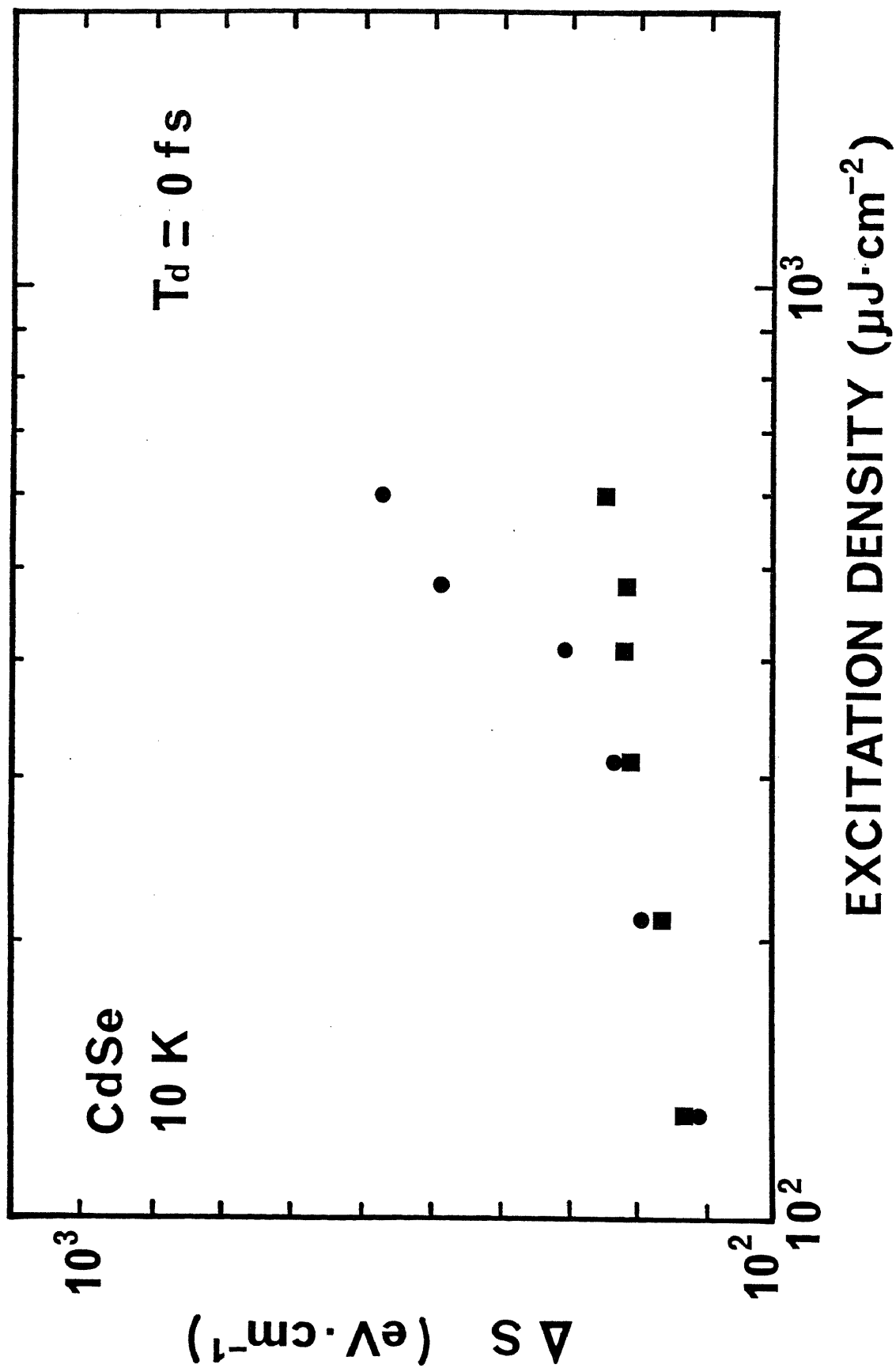


Fig. 48

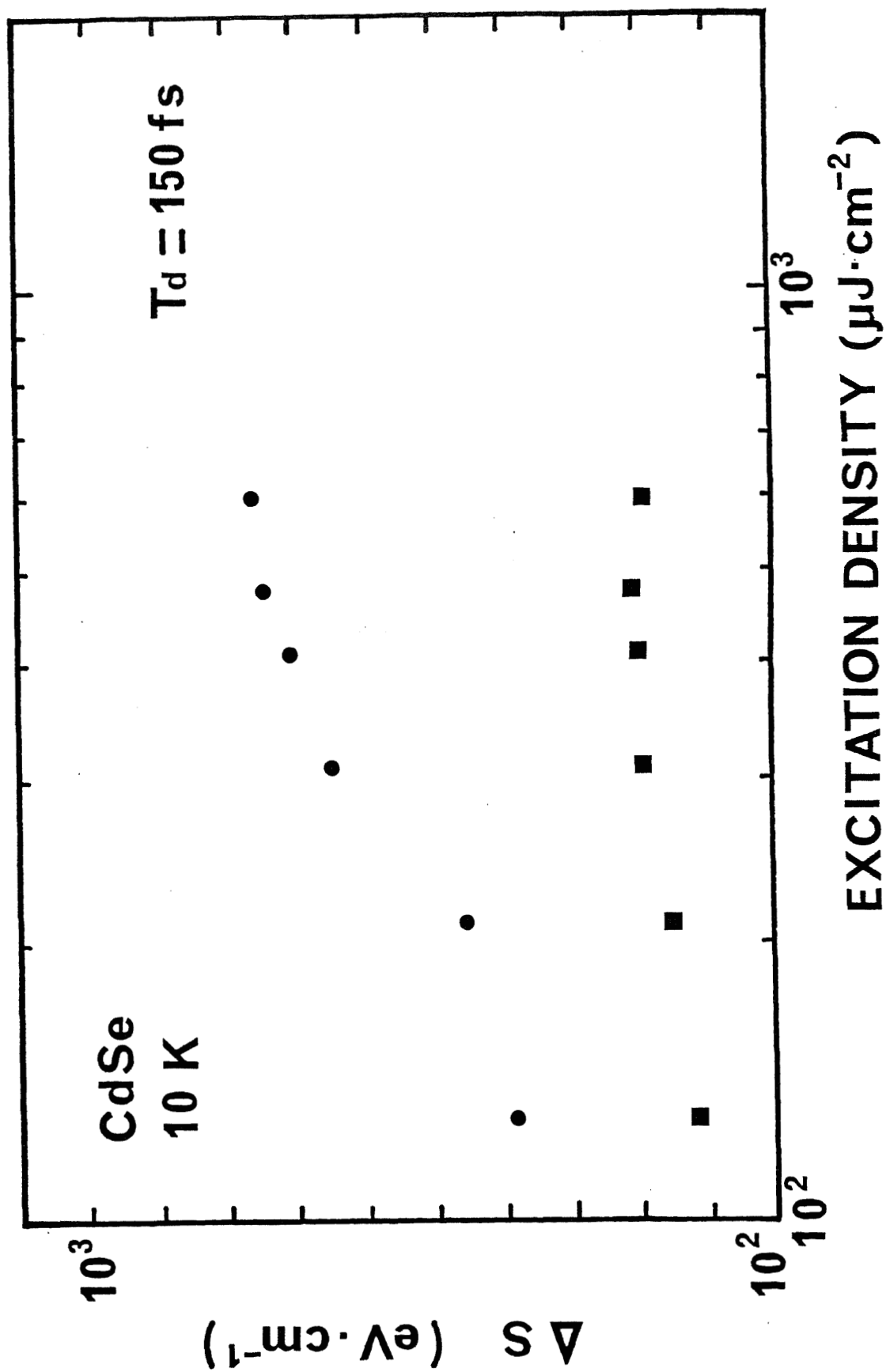


Fig. 49

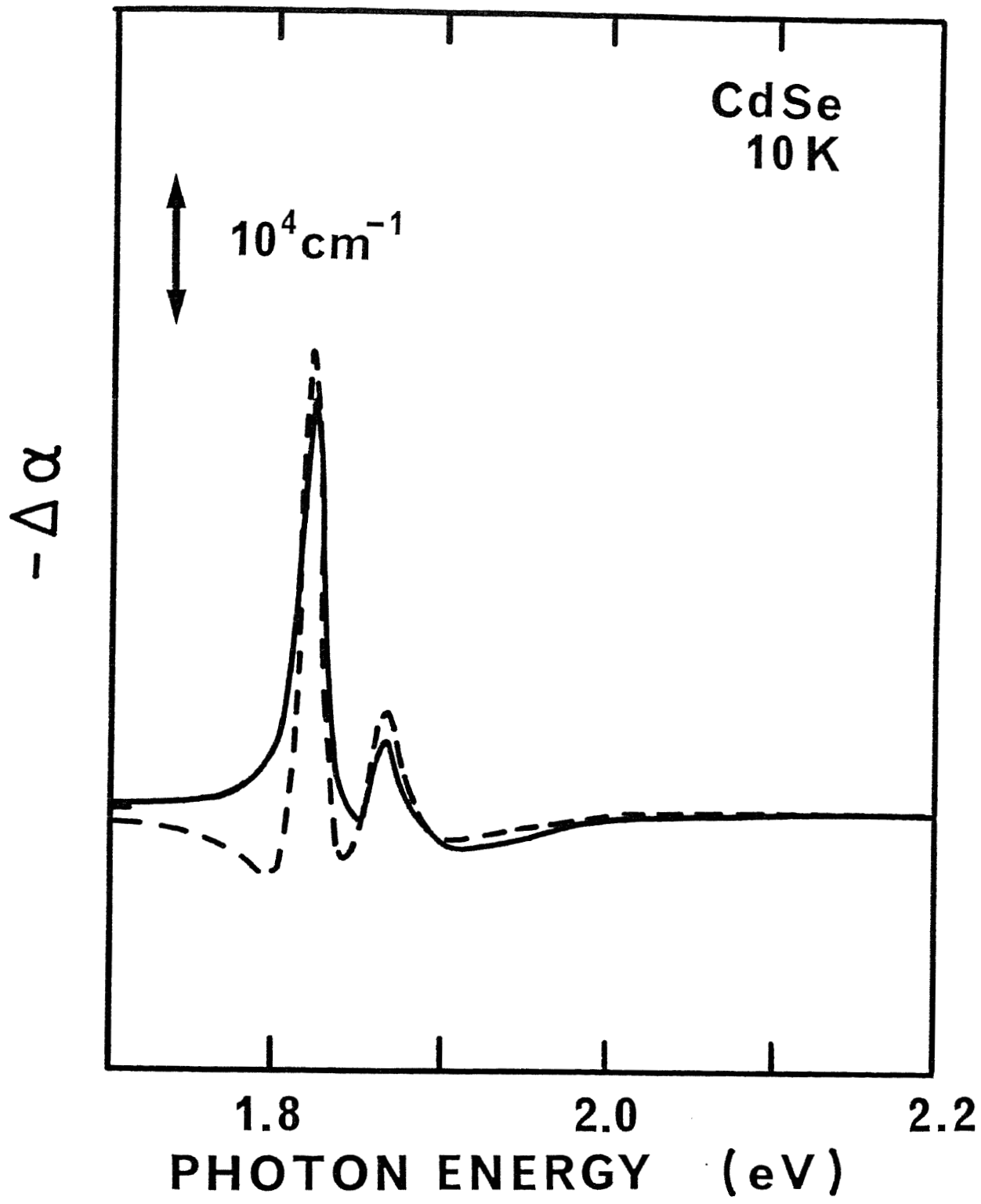


Fig. 50